THE JOURNAL OF
PHYSICAL CHEMISTRY C

Article

pubs.acs.org/JPCC

Cu-TDPAT, an *rht*-Type Dual-Functional Metal–Organic Framework Offering Significant Potential for Use in H_2 and Natural Gas Purification Processes Operating at High Pressures

Haohan Wu,[†] Kexin Yao,[§] Yihan Zhu,[§] Baiyan Li,[∥] Zhan Shi,[∥] Rajamani Krishna,[*,‡] and Jing Li[*,†]

[†]Department of Chemistry and Chemical Biology, Rutgers University, 610 Taylor Road, Piscataway, New Jersey 08854, United States

[‡]Van 't Hoff Institute for Molecular Sciences, University of Amsterdam, Science Park 904, 1098 XH Amsterdam, The Netherlands

[§]Advanced Membranes and Porous Materials Center, Chemical and Life Sciences and Engineering Division, King Abdullah University of Science and Technology, Thuwal 23955-6900, Saudi Arabia

[∥]State Key Laboratory of Inorganic Synthesis and Preparative Chemistry, College of Chemistry, Jilin University, Changchun 130012, People's Republic of China

Supporting Information

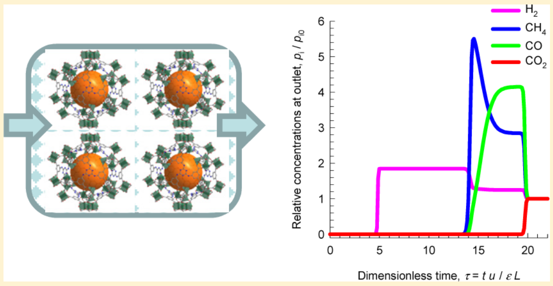

ABSTRACT: The separations of $CO_2/CO/CH_4/H_2$, CO_2/H_2, CH_4/H_2, and CO_2/CH_4 mixtures at pressures ranging to 7 MPa are important in a variety of contexts, including H_2 production, natural gas purification, and fuel-gas processing. The primary objective of this study is to demonstrate the selective adsorption potential of an *rht*-type metal–organic framework $[Cu_3(TDPAT)(H_2O)_3]\cdot 10H_2O\cdot 5DMA$ (Cu-TDPAT), possessing a high density of both open metal sites and Lewis basic sites. Experimental high pressure pure component isotherm data for CO_2, CO, CH_4, and H_2 are combined with the Ideal Adsorbed Solution Theory (IAST) for estimation of mixture adsorption equilibrium. The separation performance of Cu-TDPAT is compared with four other microporous materials, specifically chosen in order to span a wide range of physicochemical characteristics: MgMOF-74, MIL-101, LTA-5A, and NaX. For all mixtures investigated, the capacity of Cu-TDPAT to produce the desired product, H_2 or CH_4, satisfying stringent purity requirements, in a fixed bed operating at pressures exceeding about 4 MPa, is either comparable to, or exceeds, that of other materials.

1. INTRODUCTION

Metal–organic frameworks (MOFs) offer considerable potential for use in a variety of separations based on selective adsorption of one or more components from fluid mixtures.[1−4] MOFs are composed of multifunctional organic molecules linked by metal cations and offer a nearly limitless number of combinations to form new structures, resulting in an immense versatility in the possible geometries and surface properties. The specific advantages offered by MOFs over traditionally used adsorbent materials such as zeolites and activated carbon include (1) chemical tunability to any specific separation application, (2) precisely controlled pore sizes spanning a wider range, 3−20 Å, (3) wider range of pore volumes, 0.2−2 cm^3 g^{-1}, and (4) the possibility of incorporating functional groups decorating the pore walls. The chemical tunability of MOF adsorbents is advantageous for CO_2 capture,[2,4−6] separation of O_2/N_2 mixtures,[7] alkane/alkenes,[8−10] and selective adsorption of ethyne.[10−13] The ability to tune the channel dimensions is of particular importance in the separation of alkane isomers.[14] The incorporation of functional groups serves to enhance the selectivity of separations.[11,15]

The main focus of this article is on high-pressure separations of gaseous $CO_2/CO/CH_4/H_2$, CO_2/CH_4, CO_2/H_2, and CH_4/H_2 mixtures, operating at pressures ranging to 7 MPa in Pressure Swing Adsorption (PSA) units.

Hydrogen is commonly generated by steam-reforming of methane. This process generates CO and H_2 that is converted by the water-gas shift reaction to generate CO_2 and more H_2. For production of H_2, significant amounts of CO_2 need to be removed, along with relatively smaller amounts of CO and CH_4, at pressures that often exceed 3 MPa.[2,16−18] The PSA processes are commonly designed to produce H_2 at purity levels ranging from 98 to 99.99%.[18] The commonly used adsorbents are LTA-5A[19,20] (with Na^+ and Ca^{2+} extra-framework cations) and NaX[21] (also commonly denoted by its trade name 13X, with Na^+ extra-framework cations) zeolites.

The purification of pure H_2 from refinery off-gases is important in the petroleum industry.[22] The gas mixtures contain approximately 50% H_2 at 0.5−5 MPa.[23−25] Here, the impurities are C1−C5 hydrocarbons of which CH_4/H_2 separation is the most difficult separation to achieve.

Received: May 13, 2012
Revised: June 21, 2012
Published: July 16, 2012

dx.doi.org/10.1021/jp3046356 | *J. Phys. Chem. C* 2012, 116, 16609−16618

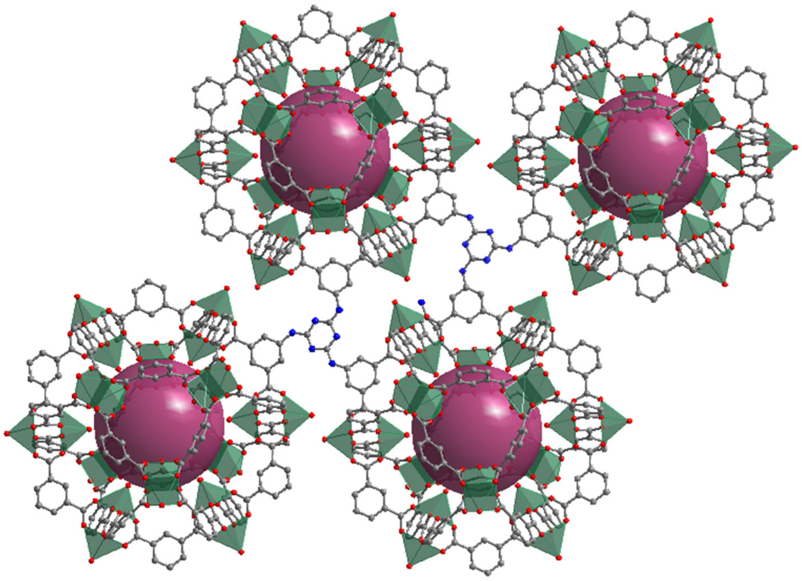

Figure 1. Crystal structure of Cu-TDPAT. Color scheme: copper, dark-green (shown as square pyramid); carbon, gray; oxygen, red; nitrogen, blue; void space, large violet sphere. H atoms are omitted for clarity. The structure shown here is the form including terminal water molecules, namely, $[Cu_3(TDPAT)(H_2O)_3]$. The framework remains intact upon removal of coordinated water molecules (see Figure S2 in the Supporting Information).

Separation of CO_2 from CH_4 is relevant to the purification of natural gas, which can have up to 92% CO_2 impurity at its source.[12] Removal of CO_2, which is most commonly accomplished using amines, is conducted between 2 and 7 MPa.[17] The separation requirements for production of liquefied natural gas (LNG) are rather stringent, often requiring the achievement of impurity levels of less than 500 ppm CO_2 in LNG.

The primary objective of this study is to demonstrate the selective adsorption potential of an *rht*-type metal–organic framework $[Cu_3(TDPAT)(H_2O)_3]\cdot 10H_2O\cdot 5DMA$ = Cu-TDPAT, H_6TDPAT = 2,4,6-tris(3,5-dicarboxylphenylamino)-1,3,5-triazine, for the aforementioned high-pressure purification processes. Cu-TDPAT[26] is the smallest member of (3,24)-connect nets of *rht* topology[27−31] made of a three-armed hexacarboxylate ligand and 24 $M_2(COO)_4$ paddle-wheel based supramolecular building blocks (SBBs),[32,33] as shown in Figure 1. Cu-TDPAT is featured with a high density of both open metal sites (1.76 nm^{-3}) and Lewis basic sites (3.52 nm^{-3}). This dual functionality is the main reason for its high adsorption capacity and strong binding affinity toward CO_2. In their earlier report, Li et al.[26] had examined the potential of Cu-TDPAT only for separation of CO_2/N_2 mixtures under near ambient pressures relevant to flue gas processing.

To underscore its potential, we compare the separation characteristics of Cu-TDPAT with four other adsorbents: MgMOF-74[34] (also denoted as CPO-27-Mg or $Mg_2(dobdc)$ ($dobdc^{4-}$ = 2,5-dioxido-1,4-benzenedicarboxylate), MIL-101,[35] LTA-5A, and NaX. While MgMOF-74 does not possess any Lewis basic sites, it has a very high density of open metal sites (4.3 nm^{-3}) and highly polarized Mg−O bonds, which are the major contributors to its exceptionally high binding affinity and uptake amount for CO_2. The recent work of Herm et al.[12,16] indicates that MgMOF-74 is attractive for H_2 and natural gas purification processes, outperforming NaX zeolite. MIL-101, whose selective adsorption potential for CO_2, CO, and CH_4 has been investigated by Chowdhury et al.,[36] has the most porous framework. However, it lacks Lewis basic sites and has a very small density of open metal sites (0.78 nm^{-3}). LTA-5A and NaX zeolites have the smallest pore volume, and the strong adsorption potential for CO_2 is attributable to Coulombic interactions with extra-framework cations.

2. ADSORPTION ISOTHERMS

Pure component isotherm measurements on a properly activated Cu-TDPAT sample were carried out for CO_2, CO, CH_4, and H_2 for pressures ranging to at least 5 MPa in order to be able to predict the high pressure separation performance with the required accuracy and reliability. Further details of synthesis and structure of Cu-TDPAT, along with the experimental details of the isotherm measurements and the isotherm fit parameters using the dual Langmuir−Freundlich model are provided in the Supporting Information accompanying this publication.

According to DFT calculations (see Supporting Information), the strongest adsorption sites of CO_2 are at unsaturated Cu metal centers that form the internal surface of the cages (Cu-1, namely, one of the two Cu atoms in each $Cu_2(COO)_4$ paddle-wheel unit that points toward the cage void); there are 24 such Cu sites per unit cell. The adsorption of 1 molecule of CO_2 per Cu-1 metal corresponds with a molar loading of 1.88 mol kg^{-1} (8.24 wt %) at which the pure component isotherm exhibits a pronounced inflection; see Figure 2a. For adsorption of the other species CO, CH_4, and H_2, no such pronounced inflection in the isotherm occurs, as is evidenced in the comparisons of the isotherm data at 298 K in Figure 2b.

The required pure component isotherm data for MgMOF-74, MIL-101, LTA-5A, and NaX, along with the structural details, are obtained from literature sources; see Supporting Information.

3. ISOSTERIC HEAT OF ADSORPTION

The isosteric heat of adsorption, Q_{st}, defined as

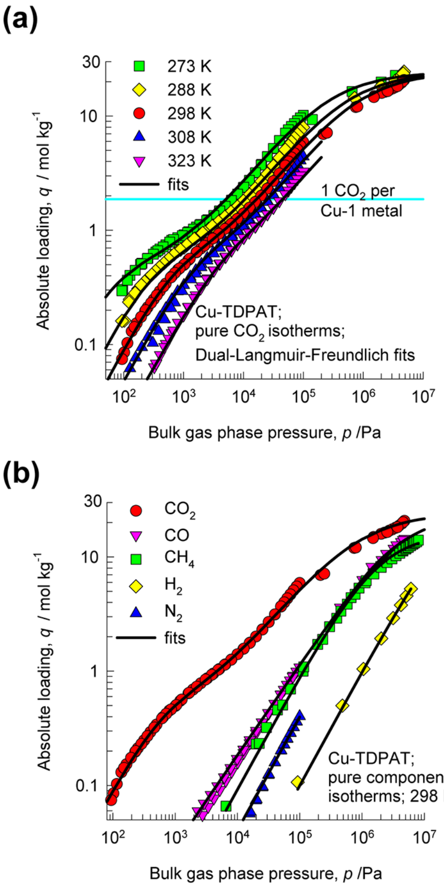

Figure 2. (a) Comparison of the experimentally determined absolute component loadings for CO_2 at 273 K, 288 K, 298 K, 308 K, and 323 K. (b) Comparison of the experimentally determined absolute component loadings for CO_2, CO, CH_4, H_2, and N_2 in Cu-TDPAT at 298 K. The continuous solid lines are the isotherm fits using fit parameters that are provided in the Supporting Information.

$$Q_{st} = RT^2\left(\frac{\partial \ln p}{\partial T}\right)_q \qquad (1)$$

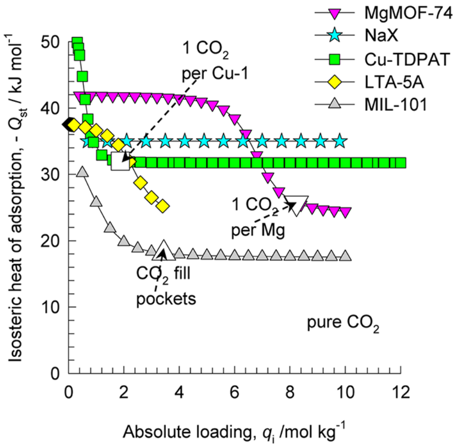

Figure 3. Comparison of isosteric heats of adsorption, Q_{st}, of CO_2 in Cu-TDPAT, MIL101, MgMOF-74, LTA-5A, and NaX. The calculations of Q_{st} are based on the use of the Clausius−Clapeyron equation, using *numerical* procedures for differentiation of the dual Langmuir−Freundlich model.

were determined using the pure component CO_2 isotherm fits. Strictly speaking, the derivative in eq 1 is to be determined with the *absolute* loading, *q*, held constant; see Myers and Monson.[37] This aspect appears to be insufficiently appreciated in some of the published literature analyzing high-pressure adsorption data,[36,38,39] while others have been careful in converting excess loadings to absolute loadings for the purposes of calculating Q_{st}.[7,15,16,40−43] In Figure 3, the loading dependence of Q_{st} for Cu-TDPAT are compared with the corresponding ones for adsorption of CO_2 in MIL-101, MgMOF-74, LTA-5A, and NaX. The strong inflection in the CO_2 isotherm for Cu-TDPAT, at a loading of 1 CO_2 per Cu-1 atom, leads to a corresponding sharp decline in Q_{st} values. The Q_{st} for MgMOF-74 shows an analogous sharp decline when the loading approaches 1 CO_2 per Mg atom.[40] It is important to note that the plateau of Q_{st} at loadings in excess of 8 mol kg^{-1} is higher for Cu-TDPAT than for MgMOF-74. We shall see later, that this has consequences for the separation performance at pressures in excess of 3 MPa for which the binding energy of CO_2 is higher in Cu-TDPAT than for MgMOF-74. For NaX zeolite, the value of Q_{st} has a constant value of 35 kJ mol^{-1}. MIL-101 has small pockets that preferentially locate CO_2; these pockets are filled at a loading corresponding to 3.44 mol kg^{-1}, rationalizing the data presented in Figure 3.

4. IAST CALCULATIONS OF ADSORPTION SELECTIVITIES AND UPTAKE CAPACITIES

The selectivity of preferential adsorption of component 1 over component 2 in a mixture containing 1 and 2 can be formally defined as

$$S_{ads} = \frac{q_1/q_2}{p_1/p_2} \qquad (2)$$

In eq 2, q_1 and q_2 are the *absolute* component loadings of the adsorbed phase in the mixture. In all the calculations to be presented below, the calculations of S_{ads} are based on the use of the Ideal Adsorbed Solution Theory (IAST) of Myers and Prausnitz.[44] The validity of IAST estimations of CO_2/CH_4, CO_2/H_2, CH_4 /H_2, and CO_2/N_2 mixture equilibria in a variety of MOFs (MgMOF-74, MOF-177, and BTP-COF) and zeolites (FAU, LTA, MFI, and CHA) has been established in earlier publications by comparison of IAST calculations with molecular simulations of binary adsorption equilibrium.[12,14,45,46] The demonstrated applicability of the IAST for MOF-177, FAU, and LTA also implies that the same would apply for MIL-101, NaX, and LTA-5A that have similar pore topologies and adsorption strengths. It should be noted that the applicability of the IAST is restricted to cases in which there is a homogeneous distribution of adsorbate species throughout the microporous framework. The IAST predictions will fail when strong segregation effects are present. Examples of segregated adsorption include preferential siting of CO_2 at the window regions,[47−49] preferential location at the intersections of network of channels,[50] or within pockets.[51] Other conditions under which IAST calculations are not of adequate accuracy are discussed by Cessford et al.[52]

The pore topology and sizes of the large cages of Cu-TDPAT are similar to those of CuBTC (HKUST-1). Configurational-Bias Monte Carlo (CBMC) simulations of the pure component adsorption isotherms of CO_2, CH_4, and H_2, along with CBMC simulations of 50/50 CO_2/CH_4 and 15/85 CO_2/H_2 mixtures, are available in the published literature for CuBTC.[5,14,49,53,54] A detailed analysis of this data, presented in Section 8 of the

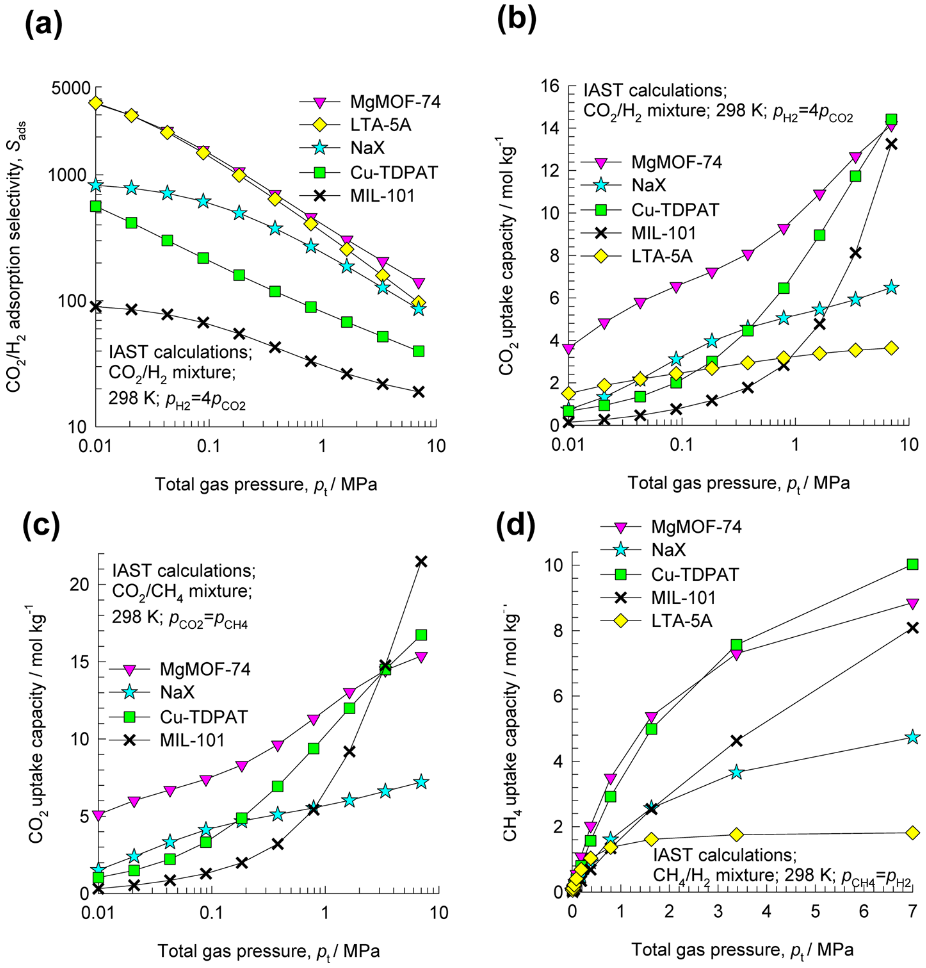

Figure 4. IAST calculations for (a) adsorption selectivity, (b) CO_2 uptake capacity of binary 20/80 CO_2/H_2 mixture at 298 K using five different adsorbents. (c) CO_2 uptake capacity of binary 50/50 CO_2/CH_4 mixture. (d) CH_4 uptake capacity of binary 50/50 CH_4/H_2 mixture.

Supporting Information, provide validation of the applicability of IAST to describe mixture adsorption in CuBTC. The same conclusion is expected to hold for Cu-TDPAT. Further validation, albeit indirect, of the IAST calculations will be provided below when comparing experimental breakthrough curves with simulations.

The IAST calculations need to be carried out using the pure component isotherm fits of *absolute* component loadings. This point needs to be emphasized here because the use of pure component isotherm fits in terms of excess loadings will lead to unreasonably high selectivities for high pressure separations, as has been demonstrated in recent work.[55] The accuracy of IAST calculations in estimation of mixture adsorption equilibrium has been established for a wide variety of guest−host combinations in zeolites and MOFs by comparison with molecular simulations.[5,14,45,46,56,57]

Figure 4a illustrates the calculations of S_{ads} for 20/80 CO_2/H_2 mixtures. The highest selectivities are obtained with MgMOF-74 and LTA-5A over the entire pressure range and this is followed by NaX and Cu-TDPAT. MIL-101 has the lowest selectivity. The uptake of CO_2 in the *adsorbed* mixture is an appropriate measure of the capacity. Figure 4b presents IAST calculations of the CO_2 uptake capacities.

An examination of the data reveals that the selectivity and capacity factors do not go hand-in-hand. For operating pressures exceeding 1 MPa, LTA-5A and NaX zeolites have lower uptake capacities; the reason for this can be traced to the pore volume of 0.25 and 0.28 cm^3/g, which are significantly lower than that of the three MOFs. As a consequence of low pore volumes, the capacities of LTA-5A and NaX for CO_2 uptake becomes limiting for high-pressure operations. Put another way, MOFs with open structures are especially attractive for high-pressure separations; indeed, the recent patent issued for use of MIL-53 as adsorbent in H_2 purification is on the basis of its claimed *capacity* advantages.[58] MgMOF-74 is rather unique in that it has both high selectivity and high capacity. That is the reason that MgMOF-74 is often the adsorbent of choice for a variety of separations.[12,14,16,40,59] The CO_2 uptake capacities for adsorption from CO_2/CH_4 mixtures show a similar trend; see Figure 4c.

For production of pure H_2 from CH_4/H_2 refinery gases, the uptake capacity of CH_4 is an important metric in comparing adsorbents, and the comparisons are provided in Figure 4d. It is noteworthy that Cu-TDPAT has a higher CH_4 uptake for pressures exceeding 2 MPa, exceeding even MgMOF-74. At a total pressure of 7 MPa, the uptake CH_4 capacity is 10 mol/kg, corresponding to 7.8 mol/L. This value is significantly higher than those for any of the 105 different MOFs examined by Wu et al.[25] in their large-scale computational screening study for CH_4/H_2 separation.

Further detailed results of IAST calculations of selectivity and capacity characteristics of all mixtures investigated here are provided as Supporting Information.

5. PACKED-BED BREAKTHROUGH SIMULATIONS AND EXPERIMENTS

It is well recognized that the separation characteristics of a PSA unit is dictated by a *combination* of adsorption selectivity and uptake capacity.[60−62] Generally speaking, higher capacities are desirable because the adsorber bed can be run for longer lengths of time before the need for regeneration arises. For a rational choice of adsorbents for mixture separation at high pressures, we need to have a proper method of evaluation that combines the selectivity and capacity metrics in a manner that is a true reflection of the separation performance of a PSA unit. For this purpose, we perform transient breakthrough calculations following the methodologies developed and described in earlier works.[59,62,63] A persuasive reason for performing such breakthrough calculations is that this procedure is the only one that ensures that the stringent purity constraints on the products, H_2 or CH_4, can be imposed in the comparisons.

Assuming plug flow of the gas mixture through the fixed bed maintained under isothermal conditions and negligible pressure drop, the partial pressures in the gas phase at any position and instant of time are obtained by solving the following set of partial differential equations for each of the species i in the gas mixture.

$$\frac{1}{RT}\frac{\partial p_i}{\partial t} = -\frac{1}{RT}\frac{\partial (v p_i)}{\partial z} - \frac{(1-\varepsilon)}{\varepsilon}\rho\frac{\partial q_i}{\partial t} \quad i = 1, 2, ...n \tag{3}$$

In eq 3, t is the time, z is the distance along the adsorber, ρ is the framework density, ε is the bed voidage, v is the interstitial gas velocity, equal to the superficial gas velocity, u, dived by ε, R is the gas constant, and T is the temperature. The molar loadings of the species i, q_i at any position z, and time t are determined from solution of the set of partial differential eqs 3. In these calculations, the loadings with a crystal at any given time t and position z are obtained from local thermodynamic equilibrium calculations using IAST.[63] Further details of the numerical procedures used to solve eq 3 to determine the transient breakthrough characteristics are available in the Supporting Information.

In order to establish the validity of the simulation methodology, breakthrough experiments were conducted for 50/50 CO_2/CH_4 and CO_2/H_2 mixtures in a setup similar to the one described by Britt et al;[34] details of the setup and procedure followed are supplied in the Supporting Information. Figure 5a,b provides a comparison of the breakthrough characteristics for 50/50 CO_2/CH_4 and CO_2/H_2 mixtures, respectively, for the activated and regenerated Cu-TDPAT samples. For both mixtures, there is close correspondence between breakthrough characteristics of the activated and regenerated samples. It was also established that the CO_2 uptake capacity remains practically unchanged even after repeated regenerations.

The continuous solid lines in Figure 5 represent solutions to eq 3 with data inputs corresponding to those in the experiments. The time at which CO_2 breaks through is very well predicted in the simulations. For natural gas and H_2 purification processes, the correct estimation of breakthrough times for CO_2 is of vital importance as they have a direct bearing on the CO_2 capture capacity, as will be elaborated later.

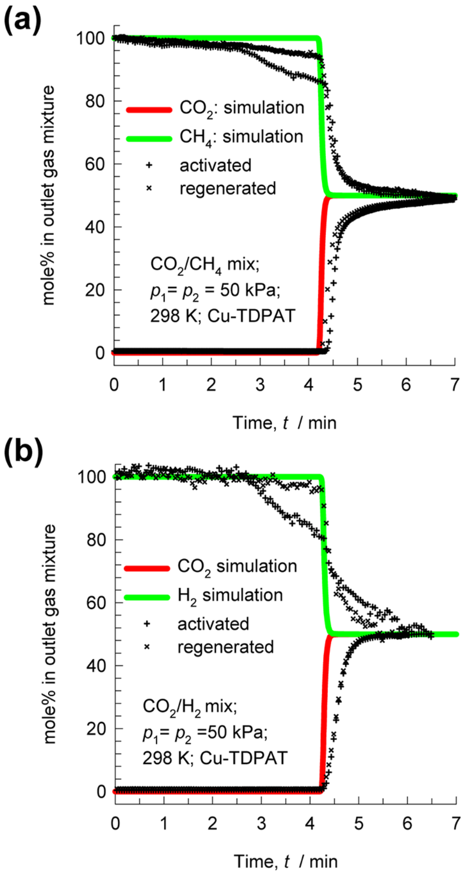

Figure 5. Experimentally determined breakthrough curves obtained for 50/50 (a) CO_2/CH_4 and (b) CO_2/H_2 mixtures using activated and regenerated samples. The smooth continuous lines are the simulation results.

We also performed breakthrough simulations in which intracrystalline diffusion effects, described with the aid of rigorous Maxwell−Stefan diffusion equations are incorporated following the methodology described in earlier works.[63,64] The diffusivities used for this purpose were those determined using MD simulations for the same set of guest molecules within CuBTC.[5,14,49,53,54,65] CuBTC has a similar pore topology, cage size, and adsorption strengths as for Cu-TDPAT, and so, the diffusivities are expected to be similar in magnitude. The entire set of partial differential equations describing diffusion, adsorption, and convective flow were solved using the methodology developed in earlier work.[63] A comparison of the two sets of simulation results (details are provided in Section 11 of the Supporting Information) demonstrates that, even for a 400 μm crystal size, intracrystalline diffusion does not significantly influence the breakthrough times. Furthermore, any uncertainties in the diffusivity values assumed for Cu-TDPAT will have no impact on the breakthrough simulations. The excellent agreement between the breakthrough times obtained in the simulations and experiments also lead to the conclusion that the IAST calculations of adsorption equilibrium are of sufficient accuracy for the analysis presented below. In PSA practice, the MOF crystals, smaller than about 400 μm, will be embedded within a macroporous matrix before being packed into a fixed bed; consequently, diffusional effects will have no impact on the performance of Cu-TDPAT, even for operations up to 7 MPa; simulation results supporting this conclusion are provided in Section 11 of the Supporting Information.

There are, however, deviations between the simulations and experiments *after* the CO_2 breaks through; the approach to the final steady-state is much sharper in the simulations than in the experiments. The reason for this is that the gas flow in the packed tubular bed is expected to be in laminar flow conditions, leading to a parabolic velocity profile. In the simulations, plug flow of the gas mixture is assumed with sharp velocity fronts traversing the bed. The deviations after the CO_2 breaks through have little consequence for the calculations of the amount of CO_2 captured because the adsorption cycle is terminated once the concentration level of CO_2 increases beyond the desired purity level.

Having established the accuracy of our breakthrough simulation methodology, we proceed to compare the separation performance of Cu-TDPAT with the other adsorbent materials. For this purpose, we compare the *equilibrium* behaviors, i.e., ignoring diffusional effects, of different materials in a fixed bed adsorber. Of the five different materials evaluated in this study, only LTA-5A is expected to suffer from severe diffusional limitations and its performance will be worse than that anticipated by an equilibrium model. The other four materials Cu-TDPAT, MgMOF-74, NaX, and MIL-101 have open structures, and the diffusivities are similar in magnitude.

6. COMPARISON OF BREAKTHROUGH CHARACTERISTICS OF DIFFERENT ADSORBENTS

In view of the wide variety of compositions and pressure ranges used in the H_2 production, natural gas purification, and fuel-gas processing, we performed breakthrough calculations for (a) 40/5/5/50 $CO_2/CO/CH_4/H_2$, (b) 40/10/50 $CO_2/CH_4/H_2$, (c) 20/80 CO_2/H_2, (d) 50/50 CO_2/CH_4, and (e) 50/50 CH_4/H_2 mixtures for pressures ranging from 0.1 to 7 MPa. The mixtures that we have considered do not include H_2O. Any moisture presumed is assumed to have been removed in initial pretreatment steps, involving condensation and dehumidification; this is common practice in natural gas processing and hydrogen production. The choice of these mixtures ensures that the conclusions to be drawn regarding the suitability of Cu-TDPAT are not restricted to a narrow range of compositions chosen. The complete set of simulation results for all mixtures is available in the Supporting Information. We begin by considering the results for a representative 40/5/5/50 $CO_2/CO/CH_4/H_2$ quaternary mixture, encountered typically in H_2 production.

Figure 6a shows typical gas phase concentrations at the exit of the adsorber packed with Cu-TDPAT for the separation of 40/5/5/50 $CO_2/CO/CH_4/H_2$ mixtures. The sequence of breakthroughs is in the order of increasing adsorption strengths: H_2, CH_4, CO, and CO_2. The breakthroughs of CH_4 and CO occur at almost the same time, and this is due to the fact that the adsorption strengths are nearly the same (cf. Figure 2b). The extent of impurities in H_2 produced are primarily dictated by the earlier breakthroughs of CH_4 and CO and only to a lesser extent by the breakthrough characteristics of CO_2 that is most strongly adsorbed. This also implies that the CH_4/H_2 and CO/H_2 adsorption selectivities are more significant determinants of the performance of the fixed bed adsorber than the CO_2/H_2 selectivity. Ranking adsorbents just on the basis of CO_2/H_2 selectivity is not justified even if CO_2 is the predominant impurity in the incoming gas stream; the less strongly adsorbed CH_4, and CO determined the PSA performance to a larger extent. From the exit gas concentrations, we can determine the ppm (CO_2 + CO + CH_4) in outlet gas as a function of the dimensionless time, τ, defined by dividing the actual time, t, by the characteristic time, (L/v). A comparison of the breakthrough characteristics of different adsorbents is presented in Figure 6b. Cu-TDPAT has the longest breakthrough time, followed by NaX. For industrial production of H_2, it is important to ensure that the sum of the impurities (CO_2 + CO + CH_4) in the outlet gas is below a specified level. We choose the impurity level to be 500 ppm (CO_2 + CO + CH_4) in outlet gas; this is a typical value in industry. When this impurity level is reached, the corresponding dimensionless breakthrough time, τ_{break}, can be determined.

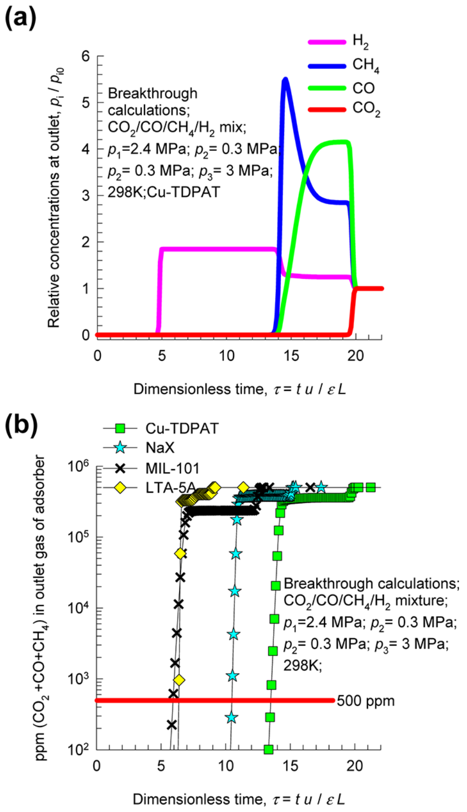

Figure 6. (a) Breakthrough characteristics a quaternary 40/5/5/50 $CO_2/CO/CH_4/H_2$ mixture in an adsorber packed with Cu-TDPAT and maintained at isothermal conditions at 298 K and total pressure of 6 MPa. Video animations of the breakthrough simulations are available as Supporting Information. (b) Ppm (CO_2 + CO+ CH_4) in outlet gas as a function of the dimensionless time for various adsorbent materials.

Figure 7a, shows the influence of the total operating pressure on dimensionless breakthrough times, τ_{break}. The value of τ_{break} decreases for all materials with increasing pressure; this is due to limitations in the capacities with increasing pressure; this decrease becomes apparent for NaX, LTA-5A, and Cu-TDPAT for pressures exceeding about 2 MPa. MIL-101, that has the highest pore volume, displays almost no change in τ_{break} with increasing pressure. In other words, the decrease in τ_{break} is a reflection of the approach to pore saturation.

Figure 7b presents data on the number of moles of H_2 produced, with 99.95%+ purity, per kg of adsorbent material during the time interval 0−τ_{break}; this quantity is obtained from a material balance across the fixed bed adsorber. The amount produced *per kg of material* is relevant for grass-roots design of

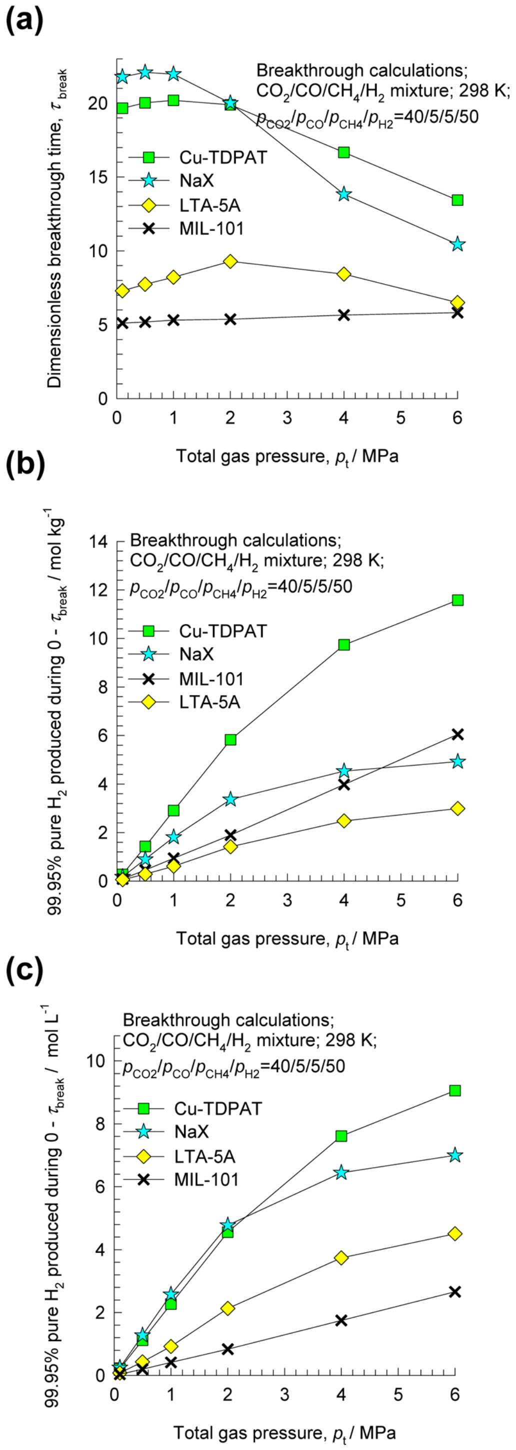

Figure 7. Influence of the total operating pressure on (a) dimensionless breakthrough times and the number of moles of 99.95%+ pure H_2 produced (b) per kg of adsorbent material and (c) per L of adsorbent material during the time interval 0−τ_{break}. The breakthrough times, τ_{break}, correspond to those when the outlet gas contains 500 ppm (CO_2 + CO + CH_4).

PSA units; this metric is directly a reflection of the adsorbent cost. We note that, on a gravimetric basis, at a total pressure of 6 MPa, the production capacity of Cu-TDPAT is more than three times that of the commonly used industrial adsorbents NaX and LTA-5A zeolites.[18,19] Particularly noteworthy is the performance of MIL-101 that has the poorest selectivity among the four materials examined (cf. Figure 4a). Per kg of adsorbent, MIL-101 is able to produce more H_2 than either NaX and LTA-5A when the total system pressures exceed 4.5 MPa. The success of MIL-101 can be traced to the high gravimetric uptake capacity (cf. Figure 4b).

Figure 7c presents data on the number of moles of 99.95%+ pure H_2 produced per L of adsorbent material during the time interval 0−τ_{break}. The volumetric production capacity is the relevant metric to use when deciding whether or not to replace the adsorbent currently used in an existing PSA unit. In this case, the adsorber dimensions are fixed, and therefore, the relevant comparison should be on a *volumetric* basis. Materials with more open structures such as MIL-101 have low framework densities and, consequently, significantly lower volumetric production capacities. For this reason, MIL-101 has the poorest volumetric production capacity over the entire pressure range. The comparison between Cu-TDPAT and NaX is interesting because NaX and Cu-TDPAT have roughly the same volumetric productivities for pressures below 2 MPa, but for p_t > 2 MPa, Cu-TDPAT outperforms NaX.

A combination of the results presented in Figure 7b,c would lead us to conclude that Cu-TDPAT is the *scenario robust* adsorbent of choice for use at H_2 production processes operating at pressures exceeding 4 MPa, performing well both for grass-roots design and also as replacement use in existing PSA units.

The relative costs of regeneration of the bed will be largely dictated by the desorption of the CO_2 captured during the interval 0−τ_{break}. From a material balance on the adsorber, these values are determined to be 2.4, 4.4, 7.9, and 10.5 mol/kg, respectively, for LTA-5A, NaX, MIL-101, and Cu-TDPAT for 6 MPa operation. From the data on the isosteric heats of adsorption at these loadings (cf. Figure 3), the regeneration energy requirements can be calculated per kg of 99.95%+ pure H_2 produced; these values are 15.7, 11.5, 11.7, and 14.5 kJ/kg. In comparison with LTA-5A and MIL-101, the higher regeneration energy requirement for Cu-TDPAT will be compensated by the significantly higher productivity. It is also remarkable to note that Cu-TDPAT has not only a higher productivity but also a *lower* regeneration energy requirement than NaX.

In two recent publications on the evaluation of MOFs for H_2 and natural gas purifications, Herm et al.[16] have presented IAST and breakthrough calculations for separation of CO_2/CH_4/H_2, CO_2/H_2, CO_2/CH_4, and CH_4/H_2 mixtures to demonstrate the superiority in the performance of MgMOF-74 when compared to NaX zeolite for operations up to 5 MPa. It is therefore important to compare the relative separation performances of Cu-TDPAT with MgMOF-74.

Figure 8a presents data on the separation of CO_2/CH_4/H_2 mixtures in a fixed bed adsorber packed with Cu-TDPAT, MgMOF-74, NaX, LTA-5A, and MIL-101. We note that, on a gravimetric basis, Cu-TDPAT becomes increasingly competitive with MgMOF-74 as the pressure increases, and for operations exceeding 3 MPa, Cu-TDPAT has a higher gravimetric H_2 production capacity than MgMOF-74; below 3 MPa, MgMOF-74 is the best adsorbent. Particularly noteworthy is the performance of MIL-101 that has the poorest selectivity among the five materials examined. Per kg of adsorbent, MIL-101 is able to produce more H_2 than either LTA-5A or NaX when the total system pressures exceed 4 MPa. The success of MIL-101 can be traced to the high gravimetric (CO_2 + CH_4) uptake capacity.

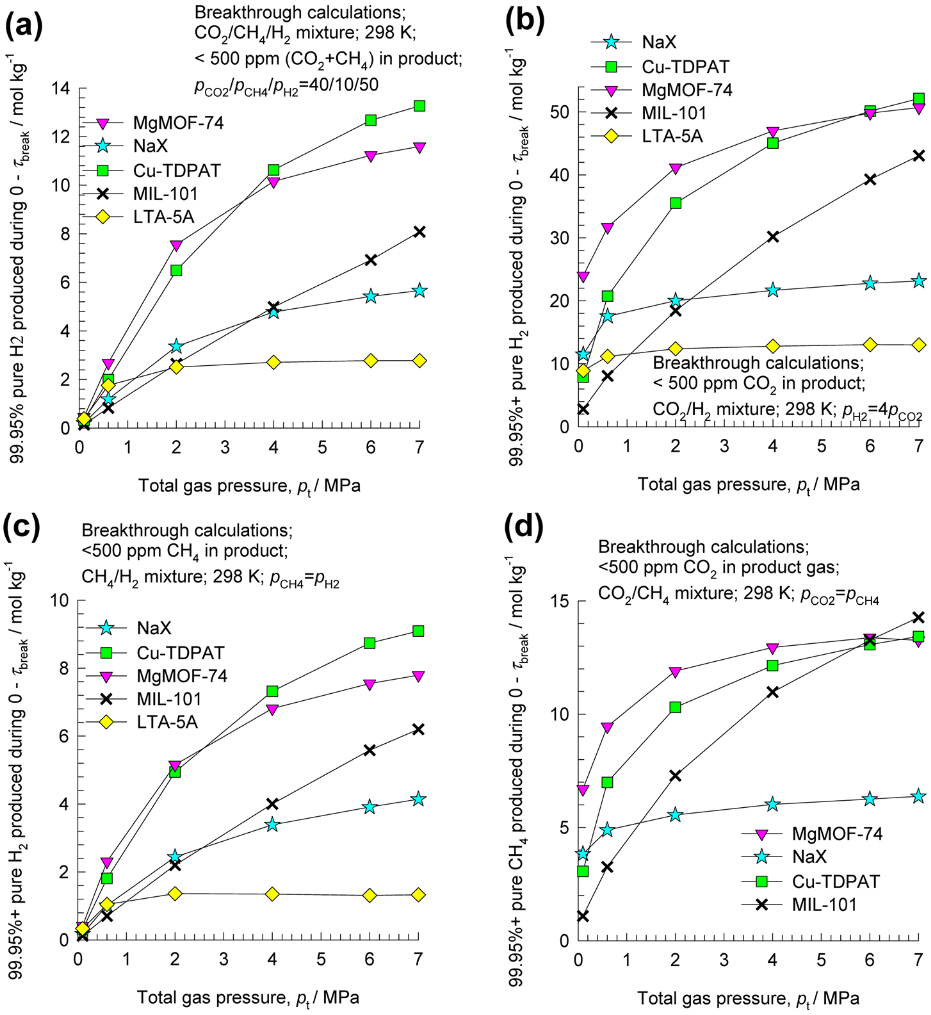

Figure 8. Influence of the total operating pressure on the number of moles of (a, b, d) 99.95%+ pure H_2 or (c) 99.95%+ pure CH_4 produced per kg of adsorbent material during the time interval 0−τ_{break} for separation of (a) 40/10/50 $CO_2/CH_4/H_2$, (b) 20/80 CO_2/H_2, (c) 50/50 CH_4/H_2, and (d) 50/50 CO_2/CH_4 mixtures. The breakthrough times, τ_{break}, correspond to those when the outlet gas contains less than 500 ppm of impurity.

Analogous results are obtained for production of 99.95%+ pure H_2 by separation of CO_2/H_2 mixtures; see Figure 8b; Cu-TDPAT outperforms NaX, LTA-5A, and MIL-101 for all pressures exceeding 0.5 MPa. However, the performance of Cu-TDPAT is superior to that of MgMOF-74 only for pressures exceeding 6 MPa.

For production of 99.95%+ pure H_2 by separation of CH_4/H_2 mixtures relevant in the context refinery gas purifications, Cu-TDPAT has the highest productivity among five different materials when pressures exceed 2 MPa; see Figure 8c.

In natural gas purification, the crucial separation is that of the CO_2/CH_4 binary mixture. The gravimetric productivities of CH_4, containing less than 500 ppm CO_2, are compared in Figure 8d. We note that, while NaX is superior to Cu-TDPAT for operations at atmospheric pressure, the efficacy of Cu-TDPAT becomes evident for higher pressures. A further point to note is that Cu-TDPAT becomes increasingly competitive with MgMOF-74 as the pressure increases, and for operations at 6 MPa, Cu-TDPAT has a CH_4 productivity comparable to that of MgMOF-74. Particularly noteworthy is the performance of MIL-101 that has the poorest selectivity among the four materials examined. Per kg of adsorbent, MIL-101 is able to produce the most amount of 99.95%+ pure CH_4 when the total system pressures exceed 6 MPa. The superiority of MIL-101 is not maintained when comparisons are made on the amount of CH_4, produced per L of adsorbent; indeed MIL-101 is the lowest productivity using this metric.

7. CONCLUSIONS

This work has demonstrated the potential of Cu-TDPAT for separation of $CO_2/CO/CH_4/H_2$, $CO_2/CH_4/H_2$, CO_2/H_2, CH_4/H_2, and CO_2/CH_4 mixtures at pressures ranging to 7 MPa in PSA units. The separation performance of Cu-TDPAT has been compared with MgMOF-74, MIL-101, LTA-5A, and NaX zeolites. For a realistic comparison, breakthrough calculations were performed for a fixed bed adsrober operating at 298 K; in these calculations, the adsorber was packed with the same *volume* of adsorbents. The following set of conclusions can be derived.

(1) The capture capacity of a relatively stronger adsorbing component such as CO_2 from mixtures with relatively weaker adsorbing components is dictated by a *combination* of (a) adsorption selectivity and (b) uptake capacity of the strongly adsorbing species. High adsorption selectivities alone do not guarantee a high capture capacity in PSA units; this point is particularly relevant for materials with relatively low uptake capacities such as

LTA-5A and NaX that have high adsorption selectivities but suffer capacity limitations for operations at pressures in excess of 1 MPa.

(2) The relative productivities of 99.95%+ pure H_2 or CH_4 can be judged either on a gravimetric (i.e., per kg of adsorbent) or volumetric (i.e., per L of adsorbent) basis. More open MOFs structures such as Cu-TDPAT and MIL-101, with large pore volumes, become increasingly attractive with increasing pressures.

(3) For all mixtures, the productivity with Cu-TDPAT exceeds that of the commonly used zeolites NaX and LTA-5A, for pressures exceeding about 1 MPa. The zeolites have relatively low pore volumes and experience capacity limitations at high pressures.

(4) For all CO_2-bearing mixtures examined, Cu-TDPAT is able to outperform MgMOF-74 on a gravimetric basis when the system pressure exceeds about 4 MPa. For H_2 purification from refinery gases, Cu-TDPAT outperforms MgMOF-74 above 2 MPa.

The major conclusion to emerge from this study is that Cu-TDPAT has significant potential for use as adsorbent in the grass-roots design of H_2 production, natural gas purification, and fuel-gas processing operations operating at high pressures.

■ ASSOCIATED CONTENT

Ⓢ Supporting Information

(a) Structural and synthesis details for Cu-TDPAT. (b) Details of experimental isotherm data measurements for Cu-TDPAT. (c) Isotherm fit parameters for all pure component isotherms of the four materials considered in this work, along with validation of the IAST. (d) Details of the numerical procedure used in breakthrough calculations. (e) Details of the experimental procedure for breakthrough measurements and comparison with breakthrough simulations including diffusion. (f) IAST calculation results of selectivity and capacity for all mixtures. (g) Breakthrough calculation results for all mixtures considered in this work. (h) Video animations showing 4-component breakthrough simulations. This material is available free of charge via the Internet at http://pubs.acs.org.

■ AUTHOR INFORMATION

Corresponding Author

*E-mail: r.krishna@uva.nl (R.K.); jingli@rutgers.edu (J.L.).

Notes

The authors declare no competing financial interest.

■ ACKNOWLEDGMENTS

J.L. and H.H.W. would like to acknowledge the partial support from DOE (DE-FG02-08ER46491).

■ REFERENCES

(1) Liu, J.; Thallapally, P. K.; McGrail, B. P.; Brown, D. R.; Liu, J. *Chem. Soc. Rev.* **2012**, *41*, 2308−2322.

(2) Sumida, K.; Rogow, D. L.; Mason, J. A.; McDonald, T. M.; Bloch, E. D.; Herm, Z. R.; Bae, T.-H.; Long, J. R. *Chem. Rev.* **2012**, *112*, 724−781.

(3) Wu, H.; Gong, Q.; Olson, D. H.; Li, J. *Chem. Rev.* **2012**, *112*, 836−868.

(4) Li, J.-R.; Sculley, J.; Zhou, H.-C. *Chem. Rev.* **2012**, *112*, 869−932.

(5) Krishna, R.; van Baten, J. M. *J. Membr. Sci.* **2010**, *360*, 323−333.

(6) An, J.; Rosi, N. L. *J. Am. Chem. Soc.* **2010**, *132*, 5578−5579.

(7) Bloch, E. D.; et al. *J. Am. Chem. Soc.* **2011**, *133*, 14814−14822.

(8) Bae, Y.-S.; Lee, C. Y.; Kim, K. C.; Farha, O. K.; Nickias, P.; Hupp, J. T.; Nguyen, S. T.; Snurr, R. Q. *Angew. Chem., Int. Ed.* **2012**, *51*, 1857−1860.

(9) Bao, Z.; Alnemrat, S.; Vasiliev, I.; Ren, Q.; Yu, L.; Lu, X.; Deng, S. *Langmuir* **2011**, *27*, 13554−13562.

(10) Bloch, E. D.; Queen, W. L.; Krishna, R.; Zadrozny, J. M.; Brown, C. M.; Long, J. R. *Science* **2012**, *335*, 1606−1610.

(11) An, J.; Geib, S. J.; Rosi, N. L. *J. Am. Chem. Soc.* **2010**, *132*, 38−39.

(12) Herm, Z. R.; Swisher, J. A.; Smit, B.; Krishna, R.; Long, J. R. *J. Am. Chem. Soc.* **2011**, *133*, 5664−5667.

(13) Das, M. C.; et al. *J. Am. Chem. Soc.* **2012**, *134*, 8708−8710.

(14) Krishna, R.; van Baten, J. M. *Phys. Chem. Chem. Phys.* **2011**, *13*, 10593−10616.

(15) McDonald, T. M.; D'Alessandro, D. M.; Krishna, R.; Long, J. R. *Chem. Sci.* **2011**, *2*, 2022−2028.

(16) Herm, Z. R.; Krishna, R.; Long, J. R. *Microporous Mesoporous Mater.* **2012**, *151*, 481−487.

(17) Rochelle, G. T. *Science* **2009**, *325*, 1652−1654.

(18) Sircar, S.; Golden, T. C. *Sep. Sci. Technol.* **2000**, *35*, 667−687.

(19) Pakseresht, S.; Kazemeini, M.; Akbarnejad, M. M. *Sep. Purif. Technol.* **2002**, *28*, 53−60.

(20) Sircar, S. *Ind. Eng. Chem. Res.* **2006**, *45*, 5435−5448.

(21) Belmabkhout, Y.; Pirngruber, G.; Jolimaitre, E.; Methivier, A. *Adsorption* **2007**, *13*, 341−349.

(22) Li, J. R.; Kuppler, R. J.; Zhou, H. C. *Chem. Soc. Rev.* **2009**, *38*, 1477−1504.

(23) Rao, M. B.; Sircar, S. *J. Membr. Sci.* **1993**, *85*, 253−264.

(24) Malek, A.; Farooq, S. *AIChE J.* **1998**, *44*, 1985−1992.

(25) Wu, D.; Wang, C.; Liu, B.; Liu, D.; Yang, Q.; Zhong, C. *AIChE J.* **2012**, *58*, 2078−2084.

(26) Li, B.; et al. *Angew. Chem., Int. Ed.* **2012**, *51*, 1412−2415.

(27) Zhao, D.; Yuan, D.; Sun, D.; Zhou, H.-C. *J. Am. Chem. Soc.* **2009**, *131*, 91866−99188.

(28) Farha, O. K.; Yazaydın, A. Ö.; Eryazici, I.; Malliakas, C. D.; Hauser, B. G.; M.G., K.; Nguyen, S. T.; Snurr, R. Q.; Hupp, J. T. *Nat. Chem.* **2010**, *2*, 944−948.

(29) Yan, Y.; et al. *J. Am. Chem. Soc.* **2010**, *132*, 4092−4094.

(30) Yuan, D.; Zhao, D.; Sun, D.; Zhou, H. C. *Angew. Chem., Int. Ed.* **2010**, *49*, 5357−5361.

(31) Zheng, B.; Bai, J.; Duan, J.; Wojtas, L.; Zaworotko, M. J. *J. Am. Chem. Soc.* **2011**, *133*, 748−751.

(32) Cairns, A. J.; Perman, J. A.; Wojtas, L.; Kravstov, V. C.; Alkordi, M. H.; Eddaoudi, M.; Zaworotko, M. J. *J. Am. Chem. Soc.* **2008**, *130*, 1560−1561.

(33) Nouar, F.; Eubank, J. F.; Bousquet, T.; Wojtas, L.; Zaworotko, M. J.; Eddaoudi, M. *J. Am. Chem. Soc.* **2008**, *130*, 1833−1835.

(34) Britt, D.; Furukawa, H.; Wang, B.; Glover, T. G.; Yaghi, O. M. *Proc. Natl. Acad. Sci. U.S.A.* **2009**, *106*, 20637−20640.

(35) Férey, G.; Mellot-Draznieks, C.; Serre, C.; Millange, F.; Dutour, J.; Surblé, S.; Margiolaki, I. *Science* **2005**, *309*, 2040−2042.

(36) Chowdhury, P.; Mekala, S.; Dreisbach, F.; Gumma, S. *Microporous Mesoporous Mater.* **2012**, *152*, 246−252.

(37) Myers, A. L.; Monson, P. A. *Langmuir* **2002**, *18*, 10261−10273.

(38) Simmons, J. M.; Wu, H.; Zhou, W.; Yildirim, T. *Energy & Environ. Sci.* **2011**, *4*, 2177−2185.

(39) Mishra, P.; Mekala, S.; Dreisbach, F.; Mandal, B.; Gumma, S. *Sep. Purif. Technol.* **2012**, *94*, 124−130.

(40) Mason, J. A.; Sumida, K.; Herm, Z. R.; Krishna, R.; Long, J. R. *Energy Environ. Sci.* **2011**, 3, 3030−3040.

(41) He, Y.; Zhang, Z.; Xiang, S.; Fronczek, F. R.; Krishna, R.; Chen, B. *Chem.—Eur. J.* **2012**, *18*, 613−619.

(42) He, Y.; Zhang, Z.; Xiang, S.; Wu, H.; Fronczek, F. R.; Zhou, W.; Krishna, R.; O'Keeffe, M.; Chen, B. *Chem.—Eur. J.* **2012**, *18*, 1901−1904.

(43) Moellmer, J.; Moeller, A.; Dreisbach, F.; Glaeser, R.; Staudt, R. *Microporous Mesoporous Mater.* **2011**, *138*, 140−148.

(44) Myers, A. L.; Prausnitz, J. M. *AIChE J.* **1965**, *11*, 121−130.

(45) Krishna, R.; van Baten, J. M. *J. Membr. Sci.* **2011**, *377*, 249−260.

(46) Krishna, R.; van Baten, J. M. *J. Membr. Sci.* **2011**, *383*, 289−300.

(47) Krishna, R.; van Baten, J. M. *Chem. Phys. Lett.* **2007**, *446*, 344−349.

(48) Krishna, R.; van Baten, J. M. *Sep. Purif. Technol.* **2008**, *61*, 414−423.

(49) Krishna, R.; van Baten, J. M. *Chem. Eng. Sci.* **2008**, *63*, 3120−3140.

(50) Krishna, R.; van Baten, J. M. *Chem. Eng. J.* **2008**, *140*, 614−620.

(51) Ryan, P.; Farha, O. K.; Broadbelt, L. J.; Snurr, R. Q. *AIChE J.* **2011**, *57*, 1759−1766.

(52) Cessford, N. F.; Seaton, N. A.; Düren, T. *Ind. Eng. Chem. Res.* **2012**, *51*, 4911−4921.

(53) Chmelik, C.; Kärger, J.; Wiebcke, M.; Caro, J.; van Baten, J. M.; Krishna, R. *Microporous Mesoporous Mater.* **2009**, *117*, 22−32.

(54) Krishna, R.; van Baten, J. M. *Chem. Eng. Sci.* **2009**, *64*, 3159−3178.

(55) Krishna, R. *Microporous Mesoporous Mater.* **2012**, *156*, 217−223.

(56) Krishna, R.; van Baten, J. M. *Chem. Eng. J.* **2007**, *133*, 121−131.

(57) Krishna, R.; van Baten, J. M. *Chem. Eng. Sci.* **2012**, *69*, 684−688.

(58) Pirngruber, G.; Jolimaître, E.; Wolff, L.; Le Coq, D. L. *Purification Method by Hydrogen Adsorbtion with Cogeneration of CO_2 Stream Pressure*. U.S. Patent 8,192,527, 2010.

(59) Krishna, R.; van Baten, J. M. *Sep. Purif. Technol.* **2012**, *87*, 120−126.

(60) Ho, M. T.; Allinson, G. W.; Wiley, D. E. *Ind. Eng. Chem. Res.* **2008**, *47*, 4883−4890.

(61) Kumar, R. *Ind. Eng. Chem. Res.* **1994**, *33*, 1600−1605.

(62) Krishna, R.; Long, J. R. *J. Phys. Chem. C* **2011**, *115*, 12941−12950.

(63) Krishna, R.; Baur, R. *Sep. Purif. Technol.* **2003**, *33*, 213−254.

(64) Krishna, R. *J. Phys. Chem. C* **2009**, *113*, 19756−19781.

(65) Krishna, R.; van Baten, J. M. *J. Phys. Chem. C* **2010**, *114*, 11557−11563.

Supplementary Information (ESI) to accompany:

Cu-TDPAT, a *rht*-type Dual-Functional Metal–Organic Framework Offering Significant Potential for Use in H_2 and Natural Gas Purification Processes Operating at High Pressures

Haohan Wu[a], Kexin Yao[c], Yihan Zhu[c], Baiyan Li[d], Zhan Shi[d], Rajamani Krishna[b]*, and Jing Li[a]*

[a]Department of Chemistry and Chemical Biology, Rutgers University, 610 Taylor Road, Piscataway,
NJ 08854, USA

[b]Van 't Hoff Institute for Molecular Sciences, University of Amsterdam, Science Park 904,
1098 XH Amsterdam, The Netherlands

[c]Advanced Membranes and Porous Materials Center, Chemical and Life Sciences and Engineering
Division, King Abdullah University of Science and Technology, Thuwal 23955-6900, Saudi Arabia

[d]State Key Laboratory of Inorganic Synthesis and Preparative Chemistry, College of Chemistry, Jilin
University,
Changchun 130012, People's Republic of China

*CORRESPONDING AUTHORS: email: r.krishna@uva.nl; jingli@rutgers.edu

Table of Contents

1. Synthesis, structure and porosity of Cu-TDPAT

$[Cu_3(TDPAT)(H_2O)_3]\cdot 10H_2O\cdot 5DMA$ (Cu-TDPAT)[1] is the smallest member of (3, 24)-connect nets of *rht* topology[2-6] made of a three-armed hexacarboxylate ligand and 24 $M_2(COO)_4$ paddle-wheel based supramolecular building blocks (SBBs)[7, 8] Solvothermal reaction of 2,4,6-tris(3,5-dicarboxylphenylamino)-1,3,5-triazine (H_6TDPAT) with excess amount of $Cu(NO_3)_2\cdot 3H_2O$ in a mixture of DMSO and DMA at 85 °C for 3 days produced blue, hexagonal-shaped crystals of Cu-TDPAT in high yield (83.3%, based on ligand).[1] The structure of Cu-TDPAT is highly porous and contains three different types of cages, cuboctahedron (cub-O_h), truncated tetrahedron (T-T_d), and truncated octahedron (T-O_h), as shown in Figure 1. The structure shown here is the form including terminal water molecules, namely $[Cu_3(TDPAT)(H_2O)_3]$. The framework remains intact upon removal of coordinated water molecules as is evident in Figure 2 which shows the XRD patterns of as-synthesized and outgassed samples. We note that the (see Figure S2 in the Supporting Information).The pore volume, BET and Langmuir surface areas are estimated to be 0.93 $cm^3\ g^{-1}$, 1938 $m^2\ g^{-1}$ and 2608, respectively, calculated from N_2 adsorption isotherms (77 K). Cu-TDPAT is featured with a high density of both open metal sites (1.76 nm^{-3}) and Lewis basic sites (3.52 nm^{-3}). This dual functionality is the main reason for its high adsorption capacity and strong binding affinity toward CO_2.

2. MOF and zeolite structures chosen for comparison with Cu-TDPAT

While the main objective of the present study is to demonstrate the efficacy of Cu-TDPAT for separation of $CO_2/CO/CH_4/H_2$, CO_2/CH_4, CO_2/H_2, and CH_4/H_2 mixtures, we also compare its separation characteristics with four other microporous structures: MgMOF-74, MIL-101, LTA-5A, and NaX zeolite; for further details on these structures detailed information on pore sizes, surface areas, pore size distributions, along with pore landscapes are available in the published literature.[9-12] Figure 3 depicts the structural frameworks of MIL-101, MgMOF-74, LTA-5A, and NaX. The physical characteristics all four structures evaluated in this study are summarized in Table 1. Figure 4 presents a 3D bar plot comparing the surface areas, pore volumes and framework densities of the five structures. A particularly noteworthy point is that the zeolites LTA-5A (with Na^+ and Ca^{++} extra-framework cations), and NaX zeolite (also commonly denoted by its trade name 13X, with Na^+ extra-framework cations) have the smallest pore volume, lowest surface area and the highest framework density. At the other end of the spectrum, MIL-10 has the highest pore volume, highest surface area but the lowest framework density. We shall see later that these physical characteristics have important consequences for the breakthrough characteristics in a Pressure Swing Adsorption (PSA) unit.

While MgMOF-74 does not possess any Lewis basic sites, it has a very high density of open metal sites ($4.3/nm^3$) and highly polarized Mg-O bonds, which are the major contributors to its exceptionally high binding affinity and uptake amount for CO_2. MIL-101, on the other hand, has the most porous framework among the three MOFs, however its lowest adsorbed amount and binding energy are attributed to lack of Lewis basic sites and a very small density of open metal sites ($0.78\ nm^{-3}$).

In all cases the comparisons are made for an operating temperature of 298 K. Also, the comparisons will be made on the performance of the selected materials in a fixed bed adsorber operating isothermally at 298 K.

3. DFT calculations

The adsorption energies of CO_2 in Cu-TDPAT were calculated by density functional theory (DFT). The structure model was constructed from the single crystal data of Cu-TDPAT. CO_2 molecule was manually placed at different positions near the Cu-TDPAT framework. Optimized ground-state geometries were obtained using generalized gradient approximation (GGA) in the parameterization of Perdew, Burke and Ernzerhof[13] with a double numerical plus polarization (DNP) basis set. During the calculations, the framework atoms of Cu-TDPAT were fixed to be immobile. All of the calculations were performed using DMol3 implemented in the *Materials Studio* package (Materials Studio 4.0, Accelrys Software Inc., 2005). Integration accuracy, SCF tolerance, orbital cutoff and geometry optimization quality were all set to “FINE”. The DFT calculations confirm that both open-metal sites and Lewis basis sites in Cu-TDPAT have higher adsorption energies than the benzene site..

4. Experimental isotherm measurements in Cu-TDPAT

Low pressure and high pressure CO gas sorption experiments were performed on volumetric gas sorption analyzers using Autosorb-1 MP (Quantachrome Instruments) and HPVA-100 (Micromeritics), respectively.

Ultra-high-purity grade gases (CO_2, CO, CH_4, N_2, H_2) were used for isotherm determinations. Some salient details are provided below.

CO_2 isotherms

CO_2 of research grade (99.998%, GTS-Welco) was used. Prior to the gas adsorption experiments, an as-synthesized sample of Cu-TDPAT was treated by replacing non-volatile DMA and DMSO with methanol. Solvent-exchanged sample (~656 mg) was loaded and outgassed at 120 °C for 12 h under a high dynamic vacuum.

The isotherms were measured up to 4.8 MPa at both 298K and 288K. At 273K, data were collected up to 3.5 MPa before CO_2 starts to condense in the sample cell.

A part of the data for CO_2 isotherms correspond to those reported in earlier work of Li et al.[1] These data were extended to other temperatures, and higher pressures in some cases.

CO isotherms

Ultra high purity CO (99.995%) was used in all the isotherm determinations. Exhaust CO was vented into hood. Two CO monitors were installed for CO detection. The sample of Cu-TDPAT was activated at 398 K under high vacuum overnight. Outgassed samples in the amount of ~90 mg and 218 mg were used for low pressure and high pressure gas sorption measurements, respectively, and the weight of each sample was recorded before and after outgassing to confirm the removal of guest molecules and to ensure the framework integrity.

CH_4 isotherms

The data for CH_4, including both low- and high- pressure regions are those measured and reported in earlier work of Li et al.[1]

H_2 isotherms

The data for H_2, including both low- and high- pressure regions are those measured and reported in earlier work of Li et al.[1]

N_2 isotherms

The data for N_2, spanning only the low pressure region below 0.1 MPa, those measured and reported in earlier work of Li et al.[1]

5. Fitting of pure component isotherms

For evaluating the performance of the five chosen adsorbent in separation of CO_2/CH_4, CO_2/H_2, and CH_4/H_2 gas mixtures we need to estimate the mixture adsorption equilibrium. For this estimation we rely on the Ideal Adsorbed Solution Theory (IAST) of Myers and Prausnitz.[14] The accuracy of the IAST estimations have been established for a wide variety of guest-host combinations.[9, 15-19] In using the IAST we need fits of the pure component isotherms for CO_2, CH_4, and H_2 for pressures ranging to at least 5 MPa in order to be able to predict the high pressure separation performance with the required accuracy and reliability.

Cu-TDPAT

The experimentally determined *excess* isotherm loadings were converted to *absolute* loadings using

$$q^{abs} = q^{excess} + \frac{pV_{pore}}{ZRT} \tag{1}$$

where Z is the compressibility factor. The Peng-Robinson equation of state was used to estimate Z. The accessible pore volume within the crystals, V_{pore}, was taken to be equal to experimentally determined value of 0.93 cm^3/g.

The pure component isotherm data for CO_2, covering both the low and high pressure ranges measured for five different temperatures 273 K, 288 K, 298 K, 308 K, and 323 K were fitted with the dual-site Langmuir-Freundlich model

$$q = q_{A,sat}\frac{b_A p^{\nu_A}}{1+b_A p^{\nu_A}} + q_{B,sat}\frac{b_B p^{\nu_B}}{1+b_B p^{\nu_B}} \tag{2}$$

with T-dependent parameters b_A, and b_B

$$b_A = b_{A0} \exp\left(\frac{E_A}{RT}\right); \quad b_B = b_{B0} \exp\left(\frac{E_B}{RT}\right) \tag{3}$$

The exponents ν_A, and ν_B have non-unity values to cater for the steepness of the isotherms. The isotherm parameters are provided in Table 2. According to DFT calculations, the strongest adsorption sites of CO_2 are at unsaturated Cu metal centers that form the internal surface of the cages (Cu-1, namely one of the two Cu atoms in each $Cu_2(COO)_4$ paddle-wheel unit that points toward the cage void); there are 24 such Cu sites per unit cell. The adsorption of 1 molecule of CO_2 per Cu-1 metal corresponds with a molar loading of 1.88 mol kg^{-1} (= 8.24 wt%) at which isotherm inflection occurs.

Table 3 presents the isotherm parameters for CO adsorption in Cu-TDPAT. Figure 5 provides a comparison of the experimentally determined absolute component loadings for CO at 273 K, 288 K, and 298 K with the isotherm fits using parameters specified in Table 3.

The pure component isotherms of CH_4, N_2 and H_2 in Cu-TDPAT do not demonstrate any inflection characteristics and the single-site Langmuir model

$$q = \frac{q_{sat} bp}{1 + bp} \tag{4}$$

provides a compares an adequately good representation of the absolute component loadings.

MgMOF-74

For evaluating the performance of MgMOF-74 the pure component isotherm data for CO_2 and CH_4, were obtained from the works of Mason et al.[20], Herm et al.[21, 22], and Dietzel et al.[23]. The measured experimental data on excess loadings were converted to absolute loadings for fitting purposes. The temperature-dependent fit parameters are specified in Tables 5, and 6. The pure component H_2 uptake data at 298 K are reported by Yaghi [24] in a document that is available on the web. The fit parameters are provided in Table 7.

NaX zeolite

For evaluating the performance of NaX zeolite we used the pure component isotherm data for CO_2, CH_4, and H_2 reported by Belmabkhout et al.[23] and Cavenati et al.[25] for a variety of temperatures. The excess loading reported in these papers are converted to absolute loadings using a pore volume of 0.28 cm^3/g, along with the Peng-Robinson equation of state for estimation of the fluid phase densities within the pores. The temperature-dependent fit parameters are specified in Tables 8, and 9.

MIL-101

The measured experimental data on excess loadings published by Chowdhury et al.[26] on pure component isotherms for CO_2, and CH_4 at 295 K, 318 K, and 353 K in MIL-101 were first converted to absolute loadings using the Peng-Robinson equation of state for estimation of the fluid phase molar densities within the pores. The temperature-dependent fit parameters are specified in Tables 10, and 11. The pure component isotherm data for pure component H_2 at 298 K are reported by Latroche et al.[27]. These data were fitted with the Langmuir constants specified in Table 12.

LTA-5A zeolite

Table 13 presents the 2-site Langmuir-Freundlich parameters for pure CO_2, CO, CH_4 and H_2 isotherms in LTA-5A zeolite. These fits are derived from fitting the data presented in Table 1 of Pakseresht et al.[28], along with Figure 6 of Sircar and Golden.[29]

Figure **6** presents a comparison of uptake of CO_2 (expressed in absolute loadings) in Cu-TDPAT, MIL101, MgMOF-74, LTA-5A and NaX. The presented uptake data are based on the isotherm fits.

6. Isosteric heat of adsorption

The isosteric heat of adsorption, Q_{st}, defined as

$$Q_{st} = RT^2 \left(\frac{\partial \ln p}{\partial T} \right)_q \tag{5}$$

were determined using the pure component isotherm fits for CO_2 and CO. Strictly speaking, the derivative in equation (5) is to be determined with the *absolute* loading, *q*, held constant; see Myers and Monson.[30] This aspect appears to be insufficiently appreciated in some of the published literature analyzing high pressure adsorption data,[26, 31, 32] while others have been careful in converting excess loadings to absolute loadings for the purposes of calculating Q_{st}.[20, 21, 33-37]

Figure 7 compares the isosteric heats of adsorption, Q_{st}, of CO_2 and CO in Cu-TDPAT. The calculations of, Q_{st}, are based on the use of the Clausius-Clapeyron equation, using *numerical* procedures for differentiation of the dual-Langmuir-Freundlich model.

7. Calculations of adsorption selectivity

The selectivity of preferential adsorption of component 1 over component 2 in a mixture containing 1 and 2, perhaps in the presence of other components too, can be formally defined as

$$S_{ads} = \frac{q_1/q_2}{p_1/p_2} \tag{6}$$

In equation (6), q_1 and q_2 are the *absolute* component loadings of the adsorbed phase in the mixture. In all the calculations to be presented below, the calculations of S_{ads} are based on the use of the Ideal Adsorbed Solution Theory (IAST) of Myers and Prausnitz.[14] These calculations are carried out using the pure component isotherm fits of absolute component loadings. This point needs to be emphasized here, because the use of pure component isotherm fits in terms of excess loadings will lead to unreasonably high selectivities for high pressure separations, as has been demonstrated in recent work.[12]

8. Validation of IAST with the aid of CBMC mixture simulations

The validity of IAST estimations of CO_2/CH_4, CO_2/H_2, CH_4/H_2, and CO_2/N_2 mixture equilibria in a variety of MOFs (MgMOF-74, MOF-177, BTP-COF) and zeolites (FAU, LTA, MFI, CHA) has been established in earlier publications by comparison of IAST calculations with molecular simulations of binary adsorption equilibrium.[9, 17, 18, 22] The demonstrated applicability of the IAST for MOF-177, FAU and LTA also implies that the same would apply for MIL-101, NaX and LTA-5A that have similar pore topologies and adsorption strengths. It should be noted that the applicability of the IAST is restricted to cases in which there is a homogenous distribution of adsorbate species throughout the microporous framework. The IAST predictions will fail when strong segregation effects are present. Examples of segregated adsorption include preferential siting of CO_2 at the window regions,[38-40] preferential location at the intersections of network of channels,[41] or within pockets.[42] Other conditions under which IAST calculations are not of adequate accuracy are discussed by Cessford et al.[43]

The pore topology and sizes of the large cages of Cu-TDPAT are similar to those of CuBTC (= HKUST-1) for which extensive investigations, both experimental and with the aid of molecular simulations, have already been conducted in the published literature. Configurational-bias Monte Carlo (CBMC) simulations of the pure component adsorption isotherms of CO_2, CH_4 and H_2, along with CBMC simulations of 50/50 CO_2/CH_4 and 15/85 CO_2/H_2 mixtures are available in the work of Krishna, van Baten and co-workers.[9, 40, 44-46] We used this set of data to seek additional validation of the IAST for estimation of 50/50 CO_2/CH_4 and 15/85 CO_2/H_2 mixture adsorption equilibrium.

Figure 8a presents the CBMC simulations of the pure component adsorption isotherms of CO_2, CH_4 and H_2 in CuBTC (= HKUST-1) at 300 K. The continuous solid lines in Figure 8a are the dual-Langmuir-Freundlich fits of the pure component isotherms. Figure 8b compares the CBMC simulations of 50/50 CO_2/CH_4 mixture adsorption with IAST calculations (indicated by continuous solid lines). Figure 8c compares the CBMC simulations of 15/85 CO_2/H_2 mixture adsorption in CuBTC with IAST calculations. For both mixtures there is excellent agreement between CBMC mixture simulations and IAST (indicated by continuous solid lines). This provides validation of the use of IAST. The continuous solid lines are the IAST estimations of the component loadings.

9. Packed bed adsorber breakthrough calculations

It is now well recognized that the separation characteristics of a PSA unit is dictated by a combination of adsorption selectivity and capacity.[47-49] For a rational choice of adsorbents for mixture separation at high pressures we need to have a proper method of evaluation that combines the selectivity and capacity metrics in a manner that is a true reflection of the separation performance of a PSA unit. For this purpose we perform transient breakthrough calculations following the methodologies developed and described in earlier works.[10, 47, 50, 51] Figure 9 shows a schematic of a packed bed adsorber. Assuming plug flow of the gas mixture through the fixed bed maintained under isothermal conditions and negligible pressure drop, the partial pressures in the gas phase at any position and instant of time are obtained by solving the following set of partial differential equations for each of the species *i* in the gas mixture.

$$\frac{1}{RT}\frac{\partial p_i(t,z)}{\partial t} = -\frac{1}{RT}\frac{\partial \left(v(t,z)p_i(t,z)\right)}{\partial z} - \frac{(1-\varepsilon)}{\varepsilon}\rho\frac{\partial q_i(t,z)}{\partial t}; \quad i = 1,2,...n \tag{7}$$

In equation (7), t is the time, z is the distance along the adsorber, ρ is the framework density, ε is the bed voidage, and v is the interstitial gas velocity, equal to the superficial gas velocity, u, dived by ε. The adsorber bed is initially free of adsorbates, i.e. we have the initial condition

$$t = 0; \quad q_i(0,z) = 0 \tag{8}$$

At time, $t = 0$, the inlet to the adsorber, $z = 0$, is subjected to a step input of the ternary gas mixture and this step input is maintained till the end of the adsorption cycle when steady-state conditions are reached.

$$t \geq 0; \quad p_i(0,t) = p_{i0}; \quad v(0,t) = u_0/\varepsilon \tag{9}$$

where u_0 is the superficial gas velocity at the inlet to the adsorber.

Invoking the constraint of negligible pressure drop, the overall material balance is obtained by summing equation (7) over the three component species

$$\frac{1}{RT}p_t\frac{\partial \left(v(t,z)\right)}{\partial z} = -\frac{(1-\varepsilon)}{\varepsilon}\rho\frac{\partial q_t(t,z)}{\partial t} \tag{10}$$

Equation (10) allows the calculation of the interstitial gas velocity v along the length of the adsorber. For high pressure separations considered in this work, the variation of the gas velocity along the length of the adsorber, and with time, needs to be properly accounted for.

The molar loadings of the species i, $q_i(z,t)$ at any position z, and time t are determined from IAST calculations. Equation (7) is first subjected to finite volume discretization. Typically, the adsorber length L is divided into 100 slices. The number of slices is determined by checking that the obtained breakthrough results do not change on increasing it. Combination of the discretized PDEs along with the algebraic IAST equilibrium model, results in a set of differential-algebraic equations (DAEs), which are solved using BESIRK.[52] BESIRK is a sparse matrix solver, based on the semi-implicit Runge-Kutta method originally developed by Michelsen[53], and extended with the Bulirsch-Stoer extrapolation method.[54] Use of BESIRK improves the numerical solution efficiency in solving the set of DAEs. The evaluation of the sparse Jacobian required in the numerical algorithm is largely based on analytic expressions.[50] Further details of the adsorber model, along with the numerical procedures used in this work, are provided in our earlier works.[17, 50, 51] Typical computation times for a binary gas mixture breakthrough are less than 100 s, allowing such transient adsorber calculations to be routinely used for screening purposes.

Figure 10 presents the calculations of the superficial gas velocity, $u(t,z) = v(t,z)\varepsilon$, at the outlet of the adsorber packed with Cu-TDPAT. The feed mixture to the adsorber is a binary CO_2/CH_4 gas mixture maintained at isothermal conditions at 298 K. In these calculations the partial pressures of CO_2 and CH_4 are taken to be equal to each other, i.e. $p_1 = p_2 = 3.5$ MPa. The y-axis is superficial gas velocity of the outlet gas mixture. The x-axis is the dimensionless breakthrough time, τ. The data show that the gas velocity changes with time, and is properly accounted for in the breakthrough calculations to be presented for all mixtures considered in this work.

10. Breakthrough experiments, and validation of breakthrough calculations

In order to establish the validity the use of the simulation methodology, breakthrough experiments were conducted for 50/50 CO_2/CH_4, CO_2/H_2 and CO_2/N_2 mixtures in the set-up depicted in Figure 11. This set-up was built following the lines in the paper of Britt et al.[55] In each experiment, a measured amount of Cu-TDPAT crystals were thoroughly ground and then packed into a stainless column (2.1 mm I.D. × 150 mm) with silica wool filling the void space. The maximum size of the ground crystals is estimated to be about 100 μm.The sample was in-situ activated under vacuum (approximately10 Pa) at

120 ºC for 10 hours to remove the adsorbed solvent and make the active sites accessible. After that, the sample was purged with CH_4 (or H_2 or N_2) flow (2.0 mL/min) for 1 hour while the temperature of the column was decreased to 25 ºC. CO_2 flow was then introduced at 2.0 mL/min without changing the CH_4 (or H_2 or N_2) flow, resulting in 50/50 CO_2/CH_4, and CO_2/H_2 and CO_2/N_2 mixtures by volume. The effluent from the column was monitored by mass spectrometry (MS). The CO_2 saturated Cu-TDPAT was purged with CH_4 (or H_2 or N_2) flow (10 mL/min) for 3 hour at 80 ºC for successive breakthrough experiments to examine its regenerability. Figures 12a, 12b and 12c provide a comparison of the breakthrough characteristics for 50/50 CO_2/CH_4, CO_2/H_2 and CO_2/N_2 mixtures, respectively, for the activated and regenerated samples. In all cases, there is close correspondence between breakthrough characteristics of the activated and regenerated samples. It was also established that the CO_2 uptake capacity remains practically unchanged even after repeated regenerations.

The continuous solid lines in Figure 12 represent solutions equation (7) with data inputs corresponding to those in the experiments. The time at which CO_2 breaks through is very well predicted in the simulations. For natural gas and H_2 purification processes, the focus of our work, the correct estimation of breakthrough times for CO_2 is of vital importance as they have a direct bearing on the CO_2 capture capacity, as will be elaborated later.

The paper by Bloch et al.[56] provides experimental validation of the breakthrough simulation methodology for ethene/ethane separations using FeMOF-74 adsorbent.

11. Influence of intra-crystalline diffusion on breakthrough characteristics of Cu-TDPAT

We also attempted to investigate whether the influence of intra-crystalline diffusion within the Cu-TDPAT crystallites influences the breakthrough characteristics. For this purpose, we repeated the breakthrough simulations including the influence of intracrystalline diffusion within crystallites of 1 mm size, which is about ten times the maximum size used in the experiments. These calculations will give an indication of the maximum influence of intra-crystalline diffusion effects. The diffusivity values used for this purpose were based on MD simulations of CO_2, CH_4, and H_2 diffusion within CuBTC, which has comparable pore topology, cage size and adsorption strengths as Cu-TDPAT. Figure 13 presents a summary of the Maxwell-Stefan diffusivities for CO_2, CH_4, and H_2. The continuous solid lines in Figure 13 are the Reed and Ehrlich model [57, 58] which leads to the following expression for the M-S diffusivity

$$Đ_i = Đ_i(0)\frac{(1+\varepsilon_i)^{z-1}}{(1+\varepsilon_i/\phi_i)^z} \tag{11}$$

expressed as a function of the fractional occupancy, θ_i defined by

$$\theta_i \equiv q_i / q_{i,sat} \tag{12}$$

where z is the coordination number, representing the maximum number of nearest neighbors within a cage. From an engineering point of view the precise choice of the value of z is not crucial, as the *combination* of z and ϕ_i prescribes the loading dependence. For the CuBTC structure we take $z = 5$. The other parameters are defined as follows (see Krishna et al.[57, 59] for more detailed discussions and derivations)

$$\varepsilon_i = \frac{(\beta_i - 1 + 2\theta_i)\phi_i}{2\,(1-\theta_i)}; \quad \beta_i = \sqrt{1 - 4\,\theta_i(1-\theta_i)(1-1/\phi_i)} \tag{13}$$

The Reed and Ehrlich model parameters for CuBTC are reported in Table 14.

The breakthrough simulations for 50/50 CO_2/CH_4, CO_2/H_2 , and CO_2/N_2 mixtures were repeated with the inclusion of the rigorous Maxwell-Stefan formulation for intra-crystalline diffusion.[60] The two sets of simulation results are compared in Figure 14. The simulation results including intra-crystalline diffusion within 400 μm crystals (indicated by crosses) yield virtually identical breakthrough times as those obtained with the assumption of thermodynamic equilibrium (indicated by continuous solid lines). The inclusion of diffusion effects leads to slightly more diffuse breakthrough characteristics *after* breakthrough.

There are, however, deviations between both sets of simulations and experiments, *after* the CO_2 breaks through; the approach to the final steady-state much sharper in the simulations than in the experiments. The reason is that the packed tubular bed is expected to be in laminar flow conditions, leading to a parabolic velocity profile. In the simulations, plug flow of the gas mixture is assumed with sharp velocity fronts traversing the bed. The deviations after the CO_2 breaks through have little consequence for the calculations of the amounts CO_2 captured because the adsorption cycle is terminated once the concentration level of CO_2 increases beyond the desired purity level. In other words the gaseous effluent after CO_2 breaks through is not included in the product stream say for H_2.

In order to further investigate the influence of diffusion on the breakthrough characteristics, we carried out breakthrough calculations for 50/50 CO_2/CH_4 mixtures at 7 MPa inlet pressure with crystals of sizes 400 μm, 600 μm, and 800 μm. The breakthrough curves, expressed in terms of ppm CO_2 in the outlet gas are shown in Figure 15. We note that with increasing particle size, the breakthrough curves are more diffuse in nature. For a required purity say of 500 ppm CO_2 in the exit gas, the breakthrough times for particle sizes of 400 μm or smaller are found to be practically identical with those calculated based on the basis of thermodynamic equilibrium. Typically, crystal sizes, smaller than 400 μm, will be embedded into a matrix material before being packed into a fixed bed. We do not anticipate diffusion effects will have any significant impact on the predicted performance of Cu-TDPAT for high pressure purifications.

We proceed further by comparing the equilibrium behaviors of different adsorbent material. The ranking of materials will not be influenced by diffusion effects.

12. The variety of mixture separations analyzed in this work

In view of the wide variety of compositions, and pressure ranges used in the H_2 production, natural gas purification, and fuel-gas processing we performed breakthrough calculations for (a) 40/5/5/50 $CO_2/CO/CH_4/H_2$, (b) 40/10/50 $CO_2/CH_4/H_2$, (c) 20/80 CO_2/H_2, (d) 50/50 CO_2/CH_4, and (e) 50/50 CH_4/H_2 mixtures for pressures ranging from 0.1 MPa to 7 MPa. The complete set of simulation results for all mixtures is presented and discussed below, for each mixture, in detail. For the 40/5/5/50 $CO_2/CO/CH_4/H_2$ quaternary mixture, the discussions presented in this Supporting Information repeat some, but not all, of the discussions in the main text of the manuscript. The discussions per mixture are on a "stand alone" basis, in order to assist readers who are interested to examine the details for only some specific mixture.

Each of the five mixture separations are discussed below in sequence.

13. Quaternary 40/5/5/50 CO_2/CO/CH_4/H_2 mixture separations

For industrial production of H_2, impurities such as need to be reduced to extremely low levels, typically lower than 500 ppm. Of these impurities, the adsorption strengths of CH_4 is the lowest and consequently the first component to breakthrough in a fixed bed adsorber will be CH_4. The concentration of the impurities can vary significantly depending on the specific processing application. For purposes of quantitative evaluation of different adsorbents we consider the separation of a CO_2/CO/CH_4/H_2 with the relative molar compositions 40/5/5/50, containing 40% CO_2, placing severe separation demands on the adsorbent. No CO isotherm data is available in the published literature for MgMOF-74, and so this MOF cannot be included in the evaluation.

Figure 16a presents the IAST calculations of the CO_2/H_2 adsorption selectivity *in the quarternary mixture,* and defined by equation (6). The highest selectivities are obtained with LTA-5A and NaX zeolites. This is followed by the two MOFs Cu-TDPAT, and MIL-101. The performance of a PSA unit is dictated not only by the adsorption selectivity but by the capacity to adsorb CO_2, CO, and CH_4. Generally speaking, higher capacities are desirable because the adsorber bed can be run for longer lengths of time before the need for regeneration arises. The sum of the component loadings of CO_2, CO, and CH_4 in the mixture, is an appropriate measure of the capacity. The component loading can be expressed either per kg or per L of adsorbent material. Figures 16b,and 16c present data on the IAST calculations of the (CO_2 +CO + CH_4) uptake capacities using these two metrics. Both metrics are relevant, as we will discuss later. An examination of the data presented in Figure 16 shows that the selectivity and capacity factors do not go hand-in-hand, especially when the operating pressures exceeding say 1 MPa. For p_t > 1MPa, LTA-5A and NaX zeolites have significantly lower capacities, both per kg and per L basis, than Cu-TDPAT whereas the selectivities of both zeolites are significantly higher than that of Cu-TDPAT for the entire range of pressures. LTA-5A and NaX have pore volumes of 0.25 cm^3/g and 0.28 cm^3/g, respectively, significantly lower than that of Cu-TDPAT (0.93 cm^3/g) and MIL-101 (1.38 cm^3/g). As a consequence, the capacity of NaX for (CO_2 + CO+ CH_4) uptake becomes limiting for operations significantly higher than 1 MPa.. Put another way, MOFs with "open' structures are especially attractive for high pressure separations.

For a proper combination of the selectivity and capacity metrics, breakthrough calculations were performed for a fixed bed depicted in Figure 17a. The following parameter values were used: $L = 0.1$ m; $\varepsilon = 0.4$; $v = 0.1$ m/s (at inlet). When comparing different materials, the fractional voidage is held constant at $\varepsilon = 0.4$. This implies the volume of adsorbents used in the fixed bed are the same for Cu-TDPAT, MIL-101, LTA-5A, and NaX. The total mass of the adsorbents used is governed by the framework density.

Figure 17b shows typical concentration profiles at the exit of the adsorber packed with Cu-TDPAT and maintained at isothermal conditions at 298 K. In these calculations the total system pressure is 6 MPa. The sequence of breakthroughs is in the order of increasing adsorption strengths: H_2, CH_4, CO, and CO_2. From the exit gas concentrations we can determine the ppm (CO_2 + CO+CH_4) in outlet gas as a function of the dimensionless time dimensionless time, τ, defined by dividing the actual time, t, by the characteristic time, $\frac{L}{v}$. A comparison of the breakthrough characteristics of different adsorbents is presented in Figure 17c. Cu-TDPAT has the longest breakthrough time, followed by NaX. When the composition in the exit gas reaches a certain desired purity level, the adsorption cycle needs to be terminated and the contents of the bed regenerated. We arbitrarily choose the purity level to be 500 ppm (CO_2 + CO + CH_4) in outlet gas. When this purity level is reached, the corresponding dimensionless breakthrough time, τ_{break}, can be determined.

To demonstrate how the choice of the best material alters with operating pressures, we carried out a series of breakthrough calculations for LTA-5A, NaX, MIL-101 and Cu-TDPAT for pressures ranging from 0.1 MPa to 6 MPa. Figure 18a, shows the influence of the total operating pressure on dimensionless breakthrough times, τ_{break}. The value of τ_{break} decreases for all materials with increasing pressure; this is due to limitations in the capacities with increasing pressure; this decrease becomes apparent for NaX, LTA-5A, and Cu-TDPAT for pressures exceeding about 2 MPa. MIL-101 that has the highest pore volume, displays almost no change in τ_{break} with increasing pressure. In other words, the decrease in τ_{break} is a reflection of the approach to pore saturation.

Figure 18b presents data on the number of moles of H_2 produced per kg of adsorbent material during the time interval 0 – τ_{break}; this quantity is obtained from a material balance across the fixed bed adsorber. The H_2 product is 99.95%+ pure, and contains the specified maximum impurities of 500 ppm (CO_2 +CO + CH_4). The amount produced *per kg of material* is relevant for grass-roots design of PSA units; this metric is directly a reflection of the adsorbent cost. We note that on a gravimetric basis, at a total pressure of 6 MPa, Cu-TDPAT has a production capacity that is more than three times that of the commonly used industrial adsorbents NaX and LTA-5A zeolites. Particularly noteworthy is the performance of MIL-101, that has the poorest selectivity amongst the four materials examined (cf. Figure 16a). Per kg basis of adsorbent, MIL-101 is able to produce more H_2 than both NaX and LTA-5A when the total system pressures exceed 4.5 MPa. The success of MIL-101 can be traced to the high gravimetric (CO_2 +CO+ CH_4) uptake capacity (cf. Figure 16b).

Figure 18c presents data on the number of moles of 99.95%+ pure H_2 produced per L of adsorbent material during the time interval 0 – τ_{break}. The volumetric production capacity is the relevant metric to use when deciding whether or not to replace the adsorbent currently used in an existing PSA unit. In this case, the adsorber dimensions are fixed, and therefore the relevant comparison should be on a *volumetric* basis. Materials with more open structures such as MIL-101 have low framework densities and, consequently, significantly lower volumetric production capacities. For this reason, MIL-101 has the poorest volumetric production capacity over the entire pressure range. The comparison between Cu-TDPAT and NaX is interesting because NaX and Cu-TDPAT have roughly the same volumetric capacities for pressures below 2 MPa, but for p_t > 2 MPa, Cu-TDPAT outperforms NaX.

A combination of the results presented in Figures 18b, and 18c would lead us to conclude that Cu-TDPAT is the *scenario robust* adsorbent of choice for use at pressures exceeding 2 MPa, performing well both for grass-roots design and also as replacement use in existing PSA units.

Let us consider the hierarchy of H_2 production capacities at a chosen total pressure of 6 MPa. Figure 19 presents plots of the number of moles of 99.95%+ pure H_2 produced (a) per kg of adsorbent material, (b) per L of adsorbent material during the time interval $0 - \tau_{\mathrm{break}}$ against the breakthrough time τ_{break}. We note that there is a near-linear correlation between the dimensionless breakthrough time, τ_{break}, and the amount of 99.95%+ pure H_2 produced per L of adsorbent. This is a rational result because the breakthrough calculations were performed with the same *volume* of adsorbent materials. The higher the value of τ_{break}, the higher the amount of H_2 produced that can be produced. Put another way, the dimensionless breakthrough time, τ_{break}, is the proper metric that reflects a combination of selectivity and capacity metrics. The best adsorbent material is Cu-TDPAT. We note that the commonly used NaX and LTA-5A zeolites are significantly poorer in their H_2 production performances because of capacity limitations at high pressures.

It is also instructive to investigate the factors that lead to desirably high H_2 production, either on a gravimetric, or volumetric basis. Figure 20 presents 3D bar plots in which the two production metrics are plotted as a function of the adsorption selectivity (x-axis), and (CO_2 + CO + CH_4) uptake capacity (y-axis), both of which calculated on the basis of IAST for the quaternary mixture. The adsorption selectivities of NaX and LTA-5A are significantly higher than that of Cu-TDPAT, but the H_2 productions in an adsorber with NaX or LTA-5A are significantly lower, using either gravimetric or volumetric production metrics. In PSA operations at high pressures, capacity considerations are paramount and can over-ride selectivity deficiencies. This is best illustrated by MIL-101 which has the poorest selectivity, yet can compete with NaX zeolite.

The overall conclusions can be summarized as follows. NaX and LTA-5A zeolites suffer increasing capacity limitations as the pressure is increased beyond 2 MPa, and more open MOF structures such as MIL-101, and Cu-TDPAT become particularly attractive. The plots in Figure 20 underscore the fallacy of ranking adsorbent purely on the basis of selectivity; capacity factors are of vital importance in PSA operations.

14. Ternary 40/10/50 CO_2/CH_4/H_2 mixture separations

For industrial production of H_2, impurities such as CO_2, CO, and CH_4 need to be reduced to extremely low levels, typically lower than 500 ppm. Of these impurities, the adsorption strengths of CH_4 is the lowest and consequently the first component to breakthrough in a fixed bed adsorber will be CH_4 as exemplified in the breakthrough curves for Cu-TDPAT in Figure 17b. We also note that the due to closeness of the pure component isotherms of CO, and CH_4 in Cu-TDPAT the breakthroughs of CO and CH_4 occur at almost the same time. We therefore investigated the separation of a ternary 40/10/50 CO_2/CH_4/H_2 mixture, in which the CO content used in the foregoing section is replaced by CH_4. A persuasive reason to investigate this mixture, is that the performance of MgMOF-74 can also be included in the comparison; this MOF was not included in the foregoing quaternary mixture separation investigations because of lack of data on the pure component CO isotherms.

Figures 21a presents the IAST calculations of the CO_2/H_2 adsorption selectivity *in the ternary mixture,* defined by equation (6). The highest selectivities are obtained with MgMOF-74 over the entire pressure range and this is followed by LTA-5A, NaX, and Cu-TDPAT. The performance of a PSA unit is dictated not only by the adsorption selectivity but by the capacity to adsorbe CO_2, and CH_4. Generally speaking, higher capacities are desirable because the adsorber bed can be run for longer lengths of time before the need for regeneration arises. The sum of the component loadings of CO_2 and CH_4 in the mixture, is an appropriate measure of the capacity. The component loading can be expressed either per kg or per L of adsorbent material. Figures 21b, and 21c present data on the IAST calculations of the (CO_2 + CH_4) uptake capacities using these two metrics. Both metrics are relevant, as will be discussed below. An examination of the data presented in Figure 21 shows that the selectivity and capacity factors do not go hand-in-hand, especially when the operating pressures exceeding say 1 MPa. For $p_t >$ 1MPa, LTA-5A and NaX have significantly lower capacities, both per kg and per L basis, than MgMOF-74, and Cu-TDPAT whereas the selectivitivities of both LTA-5A and NaX are higher than that of Cu-TDPAT for the entire range of pressures. LTA-5A and NaX have pore volumes of 0.25 cm^3/g and 0.28 cm^3/g, respectively, significantly lower than that of MgMOF-74 (0.57 cm^3/g) Cu-TDPAT (0.93 cm^3/g) and MIL-101 (1.38 cm^3/g). This is the reason that the capacity of LTA-5A and NaX for (CO_2 + CH_4) uptake becomes limiting for high pressure operations. Put another way, MOFs with "open' structures are especially attractive for high pressure separations. MgMOF-74 is rather unique in that it has both high selectivity and high capacity. That is the reason that MgMOF-74 is often the adsorbent of choice for a variety of separations.[9, 10, 20-22]

For a proper combination of the selectivity and capacity metrics, breakthrough calculations were performed for a fixed bed depicted in Figure 22a. The following parameter values were used: $L = 0.1$ m; $\varepsilon = 0.4$; $v = 0.1$ m/s (at inlet). When comparing different materials, the fractional voidage is held constant at $\varepsilon = 0.4$. This implies the volume of adsorbents used in the fixed bed are the same for Cu-TDPAT, MIL-101, MgMOF-4, LTA-5A, and NaX. The total mass of the adsorbents used is governed by the framework density.

Figure 22b shows typical concentration profiles at the exit of the adsorber packed with Cu-TDPAT and maintained at isothermal conditions at 298 K. In these calculations the total system pressure is 4 MPa. From the exit gas concentrations we can determine the ppm (CO_2 + CH_4) in outlet gas as a function of the dimensionless time dimensionless time, τ, defined by dividing the actual time, t, by the characteristic time, $\frac{L}{v}$; a comparison of the breakthrough characteristics of different adsorbents is presented in Figure 22c. MgMOF-74 has the longest breakthrough time, followed closely by Cu-TDPAT. When the composition in the exit gas reaches a certain desired purity level, the adsorption cycle needs to be terminated and the contents of the bed regenerated. We arbitrarily choose the purity level to be 500 ppm (CO_2 + CH_4) in outlet gas. When this purity level is reached, the corresponding dimensionless breakthrough time, τ_{break}, can be determined.

To demonstrate how the choice of the best material alters with operating pressures, we carried out a series of breakthrough calculations for MgMOF-74, NaX, LTA-5A, MIL-101 and Cu-TDPAT for pressures ranging from 0.1 MPa to 7 MPa. Figure 23a, shows the influence of the total operating pressure on dimensionless breakthrough times, τ_{break}. The value of τ_{break} decreases for all materials with increasing pressure; this is due to limitations in the capacities with increasing pressure. MIL-101 that has the highest pore volume, displays almost no change in τ_{break} with increasing pressure. In other words, the decrease in τ_{break} is a reflection of the approach to pore saturation. For Cu-TDPAT the decrease in τ_{break} with increasing pressure is less steep than for MgMOF-74; this is because Cu-TDPAT has a more open structure and therefore capacity limitations are of lesser significance than for NaX, and MgMOF-74.

Figure 23b presents data on the number of moles of 99.95%+ pure H_2 produced per kg of adsorbent material during the time interval 0 – τ_{break}; this quantity is obtained from a material balance across the fixed bed adsorber. The amount produced *per kg of material* is relevant for grass-roots design of PSA units; this metric is directly a reflection of the adsorbent cost. We note that on a gravimetric basis, Cu-TDPAT becomes increasingly competitive with MgMOF-74 as the pressure increases, and for operations exceeding 3 MPa, Cu-TDPAT has a higher gravimetric H_2 production capacity than MgMOF-74. Particularly noteworthy is the performance of MIL-101, that has the poorest selectivity amongst the five materials examined (cf. Figure 21a). On the basis of per kg of adsorbent, MIL-101 is able to produce more H_2 than either LTA-5A or NaX when the total system pressures exceed 4 MPa. The success of MIL-101 can be traced to the high gravimetric (CO_2 + CH_4) uptake capacity (cf. Figure 21b).

Figure 23c presents data on the number of moles of 99.95%+ pure H_2 produced per L of adsorbent material during the time interval 0 – τ_{break}. The volumetric H_2 production capacity is the relevant metric to use when deciding whether or not to replace the adsorbent currently used in an existing PSA unit. In this case, the adsorber dimensions are fixed, and therefore the relevant comparison should be on a *volumetric* basis. Materials with more open structures such as MIL-101 have low framework densities and, consequently, significantly lower volumetric prouduction capacities. For this reason, MIL-101 has the poorest volumetric production capacity over the entire pressure range. The comparison between Cu-

TDPAT and LTA-5A and NaX is interesting because these three materials have roughly the same volumetric capacities for pressures below 2 MPa, but for $p_t > 2$ MPa, Cu-TDPAT outperforms both NaX and LTA-5A. At the highest pressures Cu-TDPAT approaches the volumetric productivity of MgMOF-74.

A combination of the results presented in Figures 23b, and 23c would lead us to conclude that Cu-TDPAT is the *scenario robust* adsorbent of choice for use at pressures exceeding 4 MPa, performing well both for grass-roots design and also as replacement use in existing PSA units.

Let us consider the hierarchy of H_2 production capacities at a chosen total pressure of 7 MPa. Figure 24 presents plots of the number of moles of 99.95%+ pure H_2 produced (a) per kg of adsorbent material, (b) per L of adsorbent material during the time interval $0 - \tau_{break}$ against the breakthrough time τ_{break}. We note that there is a perfect linear correlation between the dimensionless breakthrough time, τ_{break}, and the amount of 99.95%+ pure H_2 produced per L of adsorbent. This is a rational result because the breakthrough calculations were performed with the same volume of adsorbent materials. The higher the value of τ_{break}, the higher the amount of pure H_2 produced that can be produced. Put another way, the dimensionless breakthrough time, τ_{break}, is the proper metric that reflects a combination of selectivity and capacity metrics. The best adsorbent material for operation at 7 MPa is MgMOF-74, and this is followed by Cu-TDPAT. We note that NaX zeolite is significantly poorer in its pure H_2 production performance because of capacity limitations at high pressures.

It is also instructive to investigate the factors that lead to desirably high H_2 production, either on a gravimetric, or volumetric basis. Figure 25 presents 3D bar plots in which the two production metrics are plotted as a function of the adsorption selectivity (x-axis), and (CO_2 + CH_4) uptake capacity (y-axis), both of which calculated on the basis of IAST for the ternary mixture. To illustrate this, consider let us compare Cu-TDPAT, LTA-5A and NaX. The adsorption selectivities of NaX, and LTA-5A are significantly higher than that of Cu-TDPAT, but the H_2 productions in an adsorber with NaX or LTA-5A are significantly lower, using either gravimetric or volumetric production metrics. In PSA operations at high pressures, capacity considerations are paramount and can over-ride selectivity deficiencies. This is best illustrated by MIL-101 which has the poorest selectivity, yet can compete with NaX zeolite on gravimetric production. MgMOF-74 is an exceptional MOF, and has a good combination of selectivity and capacity. It loses the competition with Cu-TDPAT only when (1) pressures exceed 3MPa, and (2) the comparison is made on a gravimetric basis. The plots in Figure 25 underscore the fallacy of ranking adsorbent purely on the basis of selectivity; capacity factors are of vital importance in PSA operations.

The overall conclusions can be summarized as follows. LTA-5A and NaX zeolites suffer increasing capacity limitation as the pressure is increased beyond 2 MPa, and more open MOF structures such as MgMOF-74, MIL-101 and Cu-TDPAT become particularly attractive. A further point to note is that even though Cu-TDPAT is less selective than MgMOF-74 (cf. Figure 21a), it becomes competitive with MgMOF-74 at pressures above 4 MPa (Figure 23).

15. Binary 20/80 CO_2/H_2 mixture separations

For production of high purity H_2, it is important to remove impurities such as CO_2, CO and CH_4. Such processes invariably use pressure swing adsorption and are operated at high pressures. The predominant impurity is CO_2. Therefore we shall compare the performance of MgMOF-74, MIL-101, Cu-TDPAT, LTA-5A and NaX for separation of CO_2/H_2 mixtures containing 20% CO_2 for pressures ranging from 0.1 MPa to 7 MPa. The analysis of the separation performance is precisely analogous to that employed in the foregoing analysis of $CO_2/CO/CH_4/H_2$ mixtures. We aim for production of H_2 with a purity level of 99.95% or more, corresponding to a maximum CO_2 content of 500 ppm. The obtained results are summarized in the same manner as in the previous section in Figures 26, 27, 29, 28, and 30. Indeed, the conclusions to be drawn are also analogous and can be summarized as follows. LTA-5A and NaX zeolite suffer increasing capacity limitation as the pressure is increased, and more open MOF structures such as MgMOF-74, MIL-101 and Cu-TDPAT become particularly attractive. While at ambient pressures LTA-5A and NaX have higher H_2 production capacities than Cu-TDPAT, the situation reverses as pressures are increased above 2 MPa. A further point to note is that even though Cu-TDPAT is less selective than MgMOF-74, it becomes competitive with this MOF at pressures above 4 MPa.

16. Binary 50/50 CO_2/CH_4 mixture separations

Natural gas purification requires removal of CO_2 from natural gas streams at pressures that can be as high as 7 MPa. We aim for natural gas production with a purity level of 99.95% or more, corresponding to a maximum CO_2 content of 500 ppm. Assuming that natural gas consists primarily of CH_4, let us compare the adsorption selectivities of MgMOF-74, MIL-101, Cu-TDPAT, and NaX zeolite. Figure 31a presents the IAST calculations of the adsorption selectivity defined by equation (6). In these calculations the partial pressures of CO_2 and CH_4 are taken to be equal to each other, i.e. $p_1 = p_2$. The highest selectivities are obtained with MgMOF-74 over the entire pressure range and this is followed by NaX zeolite and Cu-TDPAT. The performance of a PSA unit is dictated not only by the adsorption selectivity but by the capacity to adsorb CO_2 molecules. Generally speaking, higher capacities are desirable because the adsorber bed can be run for longer lengths of time before the need for regeneration arises. For CO_2 removal from natural gas, the component loadings of CO_2 in the mixture, is an appropriate measure of the capacity. The component loading can be expressed either per kg or per L of adsorbent material. Figures 31b, and 31c present data on the IAST calculations of the CO_2 uptake capacities using these two metrics. Both metrics are relevant, as we shall discuss below. An examination of the data presented in Figure 31 shows that the selectivity and capacity factors do not go hand-in-hand, especially when the operating pressures exceeding say 4 MPa. For example, NaX zeolite has a significantly lower capacity, both per kg and per L basis, than MgMOF-74, and Cu-TDPAT whereas the selectivity of NaX is higher than that of Cu-TDPAT for the entire range of pressures. NaX has a pore volume of 0.28 cm^3/g significantly lower than that of Cu-TDPAT. This is the reason that the capacity of NaX for CO_2 uptake becomes limiting for high pressure operations. Put another way, MOFs with "open' structures are especially attractive for high pressure separations. MgMOF-74 is rather unique in that it has both high selectivity and high capacity. That is the reason that MgMOF-74 is often the adsorbent of choice for a variety of separations.[9, 10, 20-22]

For a proper combination of the selectivity and capacity metrics, breakthrough calculations for a fixed bed depicted in Figure32a. The following parameter values were used: L = 0.3 m; ε = 0.4; v = 0.1 m/s (at inlet), corresponding to a superficial gas velocity $u = 0.04$ m/s (at inlet). These parameter values are the same as those used in earlier publications.[10, 12, 47] When comparing different materials, the fractional voidage is held constant at $\varepsilon = 0.4$. This implies the volume of adsorbents used in the fixed bed are the same for Cu-TDPAT, MIL-101, MgMOF-4, and NaX. The total mass of the adsorbents used is governed by the framework density.

Figure 32b shows typical concentration profiles at the exit of the adsorber packed with Cu-TDPAT and maintained at isothermal conditions at 298 K. In these calculations the partial pressures of CO_2 and CH_4 at the inlet to the adsorber is taken equal to each other, i.e. $p_1 = p_2 = 3.5$ MPa. From the exit gas concentrations we can determine the ppm CO_2 in outlet gas as a function of the dimensionless time dimensionless time, τ, defined by dividing the actual time, t, by the characteristic time, $\frac{L}{v}$; a comparison of the breakthrough characteristics of different adsorbents is presented in Figure 32c. MgMOF-74 has the longest breakthrough time, followed closely by Cu-TDPAT. When the composition in the exit gas reaches a certain desired purity level, the adsorption cycle needs to be terminated and the contents of the bed regenerated. We arbitrarily choose the purity level to be 500 ppm CO_2 in outlet gas. When this purity level is reached, the corresponding dimensionless breakthrough time, τ_{break}, can be determined.

To demonstrate how the choice of the best material alters with operating pressures, we carried out a series of breakthrough calculations for MgMOF-74, NaX, MIL-101, and Cu-TDPAT for pressures ranging from 0.1 MPa to 7 MPa. Figure 33a shows the influence of the total operating pressure on dimensionless breakthrough times, τ_{break}. The value of τ_{break} decreases for all materials with increasing pressure; this is due to limitations in the capacities with increasing pressure. MIL-101 that has the highest pore volume, displays the smallest decrease in τ_{break} with increasing pressure. In other words, the decrease in τ_{break} is a reflection of the approach to pore saturation. For Cu-TDPAT the decrease in τ_{break} with increasing pressure is less steep than for MgMOF-74; this is because Cu-TDPAT has a more open structure and therefore capacity limitations are of lesser significance than for NaX, and MgMOF-74.

Figure 33b presents data on the number of moles of 99.5%+ pure CH_4 produced per kg of adsorbent material during the time interval $0 - \tau_{break}$; this quantity is obtained from a material balance across the fixed bed adsorber. The amount produced *per kg of material* is relevant for grass-roots design of PSA units; this metric is directly a reflection of the adsorbent cost. We note that while NaX is superior to Cu-TDPAT for operations at atmospheric pressure, the efficacy of Cu-TDPAT becomes evident for higher pressures. A further point to note is that Cu-TDPAT becomes increasingly competitive with MgMOF-74 as the pressure increases, and for operations exceeding 6 MPa, Cu-TDPAT has nearly the same CH_4 productivity as MgMOF-74. Particularly noteworthy is the performance of MIL-101, that has the poorest selectivity amongst the four materials examined (cf. Figure 31a). On the basis of per kg of adsorbent, MIL-101 is able to produce the most amount of 99.5%+ pure CH_4 when the total system pressures exceed 6 MPa. The success of MIL-101 can be traced to the high gravimetric CO_2 uptake capacity (cf. Figure 31b).

Figure 33c presents data on the number of moles of 99.5%+ pure CH_4 produced per L of adsorbent material during the time interval $0 - \tau_{break}$. The volumetric production capacity is the relevant metric to use when deciding whether or not to replace the adsorbent currently used in an existing PSA unit. In this case, the adsorber dimensions are fixed, and therefore the relevant comparison should be on a *volumetric* basis. Materials with more open structures such as MIL-101 have low framework densities and, consequently, significantly lower volumetric production capacities. For this reason, MIL-101 has the poorest volumetric production capacity over the entire pressure range. The comparison between Cu-TDPAT and NaX is interesting because NaX outperforms Cu-TDPAT on a volumetric basis for pressures below 1 MPa, but this trend is reversed at higher pressures. At the highest pressures Cu-TDPAT approaches the volumetric production capacity of MgMOF-74, but does not exceed it.

A combination of the results presented in Figures 33b, and 33c would lead us to conclude that Cu-TDPAT and MgMOF-74 are both the *scenario robust* MOFs of choice for use in natural gas purification at pressures exceeding 3 MPa, performing well both for grass-roots design and also as replacement use in existing PSA units.

Let us consider the hierarchy of production capacities at a chosen total pressure of 7 MPa. Figure 34 presents plots of the number of moles of 99.5%+ pure CH_4 produced (a) per kg of adsorbent material, (b) per L of adsorbent material during the time interval 0 – $\tau_{\rm break}$ against the breakthrough time $\tau_{\rm break}$. We note that there is a perfect linear correlation between the dimensionless breakthrough time, $\tau_{\rm break}$, and the amount of 99.5%+ pure CH_4 produced per L of adsorbent. This is a rational result because the breakthrough calculations were performed with the same volume of adsorbent materials. The higher the value of $\tau_{\rm break}$, the higher the amount of CH_4 produced. Put another way, the dimensionless breakthrough time, $\tau_{\rm break}$, is the proper metric that reflects a combination of selectivity and capacity metrics. The best adsorbent material for operation at 7 MPa is MgMOF-74, and this is followed by Cu-TDPAT. We note that NaX zeolites is significantly poorer in its CH_4 production performance because of capacity limitations at high pressures.

It is also instructive to investigate the factors that lead to desirably high production capacities, either on a gravimetric, or volumetric basis. Figure 35 presents 3D bar plots in which the two production capacity metrics are plotted as a function of the adsorption selectivity (x-axis), and CO_2 uptake capacity (y-axis), both of which calculated on the basis of IAST for the binary mixture. To illustrate this, consider let us compare Cu-TDPAT and NaX. The adsorption selectivity of NaX is significantly higher than that of Cu-TDPAT, but production capacity of NaX is significantly lower, using either gravimetric or volumetric productivity metrics. In PSA operations at high pressures, capacity considerations are paramount and can over-ride selectivity deficiencies. This is best illustrated by MIL-101 which has the poorest selectivity, yet can compete with NaX zeolite. MgMOF-74 is an exceptional MOF, and has a good combination of selectivity and capacity. It loses the competition with Cu-TDPAT only when (1) pressures exceed 3MPa, and (2) the comparison is made on a gravimetric basis. The plots in Figure 35 underscore the fallacy of ranking adsorbent purely on the basis of selectivity; capacity factors are of vital importance in PSA operations.

17. Binary 50/50 CH_4/H_2 mixture separations

MOFs and ZIFs have potential use in recovery of H_2 from a mixture of hydrocarbons in a refinery context. Amongst the hydrocarbons, CH_4 is the poorest adsorption strength, and consequently the separation performance is dictated by that of the mixture CH_4/H_2.[45, 61-66] The separation of CH_4/H_2 mixtures is also of relevance in the process of purification of synthesis gas obtained from steam reforming of natural gas.[63, 64]

The results of the evaluation of the five different materials for separation of CH_4/H_2 mixtures are presented in Figures 36, 37, 38, 39, and 40. The conclusions to be drawn can be summarized as follows. LTA-5A and NaX zeolites suffer increasing capacity limitations as the pressure is increased beyond 2 MPa, and more open MOF structures such as MgMOF-74, and Cu-TDPAT become particularly attractive. A further point to note is that even though Cu-TDPAT is less selective than MgMOF-74 (cf. Figure 36a), it becomes competitive with MgMOF-74 at pressures above 4 MPa (see Figures 38, 39, and 40).

Wu et al.[66] have reported the results of a large-scale computational screening study of 105 different MOFs to determine the best adsorbent for separation of CH_4/H_2 mixtures for pressures ranging to 4 MPa; their study concludes that the best adsorbent for this purpose is MOF-116. The results shown in Figures 38, 39, and 40 lead to the conclusion that Cu-TDPAT offers even higher production capacities than offered by MOF-116.

18. Notation

b_A	dual-Langmuir-Freundlich constant for species i at adsorption site A, $\mathrm{Pa}^{-\nu_i}$
b_B	dual-Langmuir-Freundlich constant for species i at adsorption site B, $\mathrm{Pa}^{-\nu_i}$
L	length of packed bed adsorber, m
p_i	partial pressure of species i in mixture, Pa
p_t	total system pressure, Pa

q_{i}	component molar loading of species i, mol kg^{-1}
q_{t}	total molar loading in mixture, mol kg^{-1}
$q_{\mathrm{sat,A}}$	saturation loading of site A, mol kg^{-1}
$q_{\mathrm{sat,B}}$	saturation loading of site B, mol kg^{-1}
Q_{st}	isosteric heat of adsorption, J mol^{-1}
R	gas constant, 8.314 J mol^{-1} K^{-1}
S_{ads}	adsorption selectivity, dimensionless
t	time, s
T	absolute temperature, K
u	superficial gas velocity in packed bed, m s^{-1}
v	interstitial gas velocity in packed bed, m s^{-1}
V_{pore}	pore volume, m^3 kg^{-1}
z	distance along the adsorber, m
Z	Compressibility factor, dimensionless

Greek letters

ε	voidage of packed bed, dimensionless
ν	exponent in dual-Langmuir-Freundlich isotherm, dimensionless
ρ	framework density, kg m^{-3}
τ	time, dimensionless
τ_{break}	breakthrough time, dimensionless

Subscripts

i	referring to component i
A	referring to site A
B	referring to site B

Superscripts

abs	referring to absolute loading
excess	referring to excess loading
B	referring to site B

Table 1. Structural data on the different MOFs and NaX evaluated in this study for comparison purposes. The data for MgMOF-74 and NaX are from Herm et al. [22] and Krishna and Long [47]. The data for MIL-101 are taken from Chowdhury et al.[26]. The data for LTA-5A are from Pakseresht et al.[28] and Sircar and Golden.[29]

MOFs	Surface area $m^2 g^{-1}$	Pore volume $cm^3 g^{-1}$	Framework density $kg m^{-3}$
NaX zeolite	950	0.280	1421
LTA-5A	450	0.250	1508
MgMOF-74	1800	0.573	905
MIL-101	2674	1.38	440
Cu-TDPAT	1938	0.93	782

Table 2. Dual-site Langmuir-Freundlich parameters for pure CO_2 in Cu-TDPAT. These fits are based on experimental data for temperatures of 273 K, 288 K, 298 K, 308 K, and 323 K. It is to be noted that for all guest molecules the experimentally determined excess loadings were first converted to absolute loadings using the Peng-Robinson equation of state for estimation of the fluid density. The pore volume used is 0.93 $\mathrm{cm^3/g}$, determined experimentally.

$$q = q_{A,sat}\frac{b_A p^{\nu_A}}{1+b_A p^{\nu_A}} + q_{B,sat}\frac{b_B p^{\nu_B}}{1+b_B p^{\nu_B}}$$

$$q_{sat,A} = 0.46\ \mathrm{mol\,kg^{-1}}$$

$$q_{sat,B} = 23.9\,\mathrm{mol\,kg^{-1}}$$

$$b_A = b_{A0}\exp\left(\frac{E_A}{RT}\right);$$

$$b_{A0} = 1.33\times10^{-16}\ \mathrm{Pa}^{-\nu A}$$

$$E_A = 72\ \mathrm{kJ\ mol^{-1}}$$

$$\nu_A = 1.2$$

$$b_B = b_{B0}\exp\left(\frac{E_B}{RT}\right);$$

$$b_{B0} = 2.91\times10^{-9}\ \mathrm{Pa}^{-\nu B}$$

$$E_B = 23.8\ \mathrm{kJ\ mol^{-1}}$$

$$\nu_B = 0.75$$

Table 3. Dual-site Langmuir-Freundlich parameters for pure component isotherms of CO in Cu-TDPAT. These fits are based on experimental data that were carried out at 273 K, 288 K, 298 K. It is to be noted that for all guest molecules the experimentally determined excess loadings were first converted to absolute loadings using the Peng-Robinson equation of state for estimation of the fluid density. The pore volume used is 0.93 cm^3/g, determined experimentally.

$$q = q_{A,sat} \frac{b_A p^{\nu_A}}{1+b_A p^{\nu_A}} + q_{B,sat} \frac{b_B p^{\nu_B}}{1+b_B p^{\nu_B}}$$

$$q_{sat,A} = 0.46 \ \mathrm{mol\,kg^{-1}}$$

$$q_{sat,B} = 23.9 \,\mathrm{mol\,kg^{-1}}$$

$$b_A = b_{A0} \exp\left(\frac{E_A}{RT}\right);$$
$$b_{A0} = 1.33\times10^{-16} \ \mathrm{Pa}^{-\nu A}$$
$$E_A = 72 \ \mathrm{kJ\ mol^{-1}}$$
$$\nu_A = 1.2$$

$$b_B = b_{B0} \exp\left(\frac{E_B}{RT}\right);$$
$$b_{B0} = 2.91\times10^{-9} \ \mathrm{Pa}^{-\nu B}$$
$$E_B = 23.8 \ \mathrm{kJ\ mol^{-1}}$$
$$\nu_B = 0.75$$

Table 4. 1-site Langmuir parameters for pure component isotherms of CH_4, N_2 and H_2 in Cu-TDPAT. These fits are based on experimental data that were carried out at 298 K. It is to be noted that for all guest molecules the experimentally determined excess loadings were first converted to absolute loadings using the Peng-Robinson equation of state for estimation of the fluid density. The pore volume used is 0.93 cm^3/g, determined experimentally.

	$q_{A,sat}$ mol kg^{-1}	b Pa^{-1}	ν_A dimensionless
CH_4	16	5.77×10^{-7}	1
N_2	24	1.69×10^{-7}	1
H_2	38.5	2.6×10^{-8}	1

Table 5. Dual-site Langmuir parameter for adsorption of CO_2 in MgMOF-74. These parameters were determined by fitting adsorption isotherms for temperatures ranging from 278 K to 473 K. The fit parameters are those reported earlier in the work of Mason et al.[20]

$$q \equiv q_A + q_B = \frac{q_{sat,A} b_A p}{1 + b_A p} + \frac{q_{sat,B} b_B p}{1 + b_B p}$$

$$q_{sat,A} = 6.8\,\mathrm{mol\,kg}^{-1}$$

$$q_{sat,B} = 9.9\,\mathrm{mol\,kg}^{-1}$$

$$b_A = b_{A0} \exp\left(\frac{E_A}{RT}\right);$$
$$b_{A0} = 2.44 \times 10^{-11}\ \mathrm{Pa}^{-1}$$
$$E_A = 42\ \mathrm{kJ\ mol}^{-1}$$

$$b_B = b_{B0} \exp\left(\frac{E_B}{RT}\right);$$
$$b_{B0} = 1.39 \times 10^{-10}\ \mathrm{Pa}^{-1}$$
$$E_B = 24\ \mathrm{kJ\ mol}^{-1}$$

Table 6. Dual-site Langmuir parameter for adsorption of CH_4 and H_2 in MgMOF-74. The CH_4 parameters were determined by fitting adsorption isotherm data reported in the work of Dietzel et al. [67]. The reported excess loading data were converted to absolute loadings for fitting purposes.

CH_4:

$$q \equiv q_A + q_B = \frac{q_{sat,A} b_A p}{1+b_A p} + \frac{q_{sat,B} b_B p}{1+b_B p}$$

$$q_{sat,A} = 11 \text{ mol kg}^{-1}; \; q_{sat,B} = 5 \text{ mol kg}^{-1}$$

$$b_A = b_{A0} \exp\left(\frac{E_A}{RT}\right); \qquad b_B = b_{B0} \exp\left(\frac{E_B}{RT}\right);$$

$$b_{A0} = 3.01\times10^{-10} \text{ Pa}^{-1}; \; b_{B0} = 4.08\times10^{-11} \text{ Pa}^{-1}$$

$$E_A = 20.5 \text{ kJ mol}^{-1} \qquad E_B = 16 \text{ kJ mol}^{-1}$$

Table 7. H_2: the absolute uptake data in MgMOF-74 at 298 K reported by Yaghi [24], a document that is available on the web. The fit parameters are therefore only for 298 K.

	Site A		
	$q_{i,A,sat}$ mol kg^{-1}	$b_{i,A}$ Pa^{-1}	$\nu_{i,A}$ dimensionless
H_2	36	2.1×10^{-8}	1

Table 8. Dual-site Langmuir parameter for adsorption of CO_2 in NaX zeolite. These parameters were determined by fitting adsorption isotherm data reported in the works of Belmabkhout et al.[23] and Cavenati et al.[25], after converting the excess data to absolute loadings.

$$q \equiv q_A + q_B = \frac{q_{sat,A} b_A p}{1 + b_A p} + \frac{q_{sat,B} b_B p}{1 + b_B p}$$

$$q_{sat,A} = 3.5\,\mathrm{mol\,kg^{-1}}$$

$$q_{sat,B} = 5.2\,\mathrm{mol\,kg^{-1}}$$

$$b_A = b_{A0} \exp\left(\frac{E_A}{RT}\right);$$
$$b_{A0} = 3.64 \times 10^{-13}\ \mathrm{Pa^{-1}}$$
$$E_A = 35\ \mathrm{kJ\ mol^{-1}}$$

$$b_B = b_{B0} \exp\left(\frac{E_B}{RT}\right);$$
$$b_{B0} = 6.04 \times 10^{-11}\ \mathrm{Pa^{-1}}$$
$$E_B = 35\ \mathrm{kJ\ mol^{-1}}$$

Table 9. Dual-site Langmuir parameter for adsorption of CH_4 and H_2 in NaX zeolite. These parameters were determined by fitting adsorption isotherm data reported in the works of Belmabkhout et al.[23], after converting the excess data to absolute loadings.

CH_4:

$$q \equiv q_A + q_B = \frac{q_{sat,A} b_A p}{1 + b_A p} + \frac{q_{sat,B} b_B p}{1 + b_B p}$$

$$q_{sat,A} = 4 \ \mathrm{mol\,kg}^{-1}; \ q_{sat,B} = 5\,\mathrm{mol\,kg}^{-1}$$

$$b_A = b_{A0} \exp\left(\frac{E_A}{RT}\right); \qquad b_B = b_{B0} \exp\left(\frac{E_B}{RT}\right);$$

$$b_{A0} = 3.66 \times 10^{-10} \ \mathrm{Pa}^{-1}; \ b_{B0} = 3.75 \times 10^{-9} \ \mathrm{Pa}^{-1}$$

$$E_A = 14 \ \mathrm{kJ\,mol}^{-1} \qquad E_B = 14 \ \mathrm{kJ\,mol}^{-1}$$

H_2:

$$q = \frac{q_{sat} bp}{1 + bp}$$

$$q_{sat} = 18 \ \mathrm{mol\,kg}^{-1}$$

$$b = b_0 \exp\left(\frac{E}{RT}\right);$$

$$b_0 = 2.43 \times 10^{-9} \ \mathrm{Pa}^{-1}$$

$$E = 6 \ \mathrm{kJ\,mol}^{-1}$$

Table 10. Dual-site Langmuir parameters for pure CO_2 isotherms in MIL-101. These fits are based on the experimental data of Chowdhury et al. [26].

$$q \equiv q_A + q_B = \frac{q_{sat,A} b_A p}{1 + b_A p} + \frac{q_{sat,B} b_B p}{1 + b_B p}$$

$$q_{sat,A} = 1 \text{ mol kg}^{-1}$$

$$q_{sat,B} = 45 \text{ mol kg}^{-1}$$

$$b_A = b_{A0} \exp\left(\frac{E_A}{RT} \right);$$
$$b_{A0} = 3.31 \times 10^{-11} \text{ Pa}^{-1}$$
$$E_A = 36 \text{ kJ mol}^{-1}$$

$$b_B = b_{B0} \exp\left(\frac{E_B}{RT} \right);$$
$$b_{B0} = 1.98 \times 10^{-10} \text{ Pa}^{-1}$$
$$E_B = 18 \text{ kJ mol}^{-1}$$

Table 11. 1-site Langmuir parameters for pure CH_4 isotherms in MIL-101. These fits are based on the experimental data of Chowdhury et al. [26].

$$q = \frac{q_{sat} bp}{1 + bp}$$

$$q_{sat} = 34 \text{ mol kg}^{-1}$$

$$b = b_0 \exp\left(\frac{E}{RT} \right);$$
$$b_0 = 1.79 \times 10^{-9} \text{ Pa}^{-1}$$
$$E = 9.9 \text{ kJ mol}^{-1}$$

Table 12. 1-site Langmuir parameters for pure H_2 isotherms in MIL-101. These fits are based on the experimental data of Latroche et al.[27].

$$q = \frac{q_{sat} b p}{1 + b p}$$

$$q_{sat} = 34 \, \text{mol kg}^{-1}$$

$$b = b_0 \exp\left(\frac{E}{RT}\right);$$
$$b_0 = 1.79 \times 10^{-9} \text{ Pa}^{-1}$$
$$E = 9.9 \text{ kJ mol}^{-1}$$

Table 13. 2-site Langmuir-Freundlich parameters for pure CO_2, CO, CH_4 and H_2 isotherms in LTA-5A zeolite. The fits for pure CO_2, CO, CH_4 are derived from re-fitting the experimental data at 303 K presented in Table 1 of Pakseresht et al.[28]. The isotherm fit for H_2 is based on the data presented in Figure 6 of Sircar and Golden,[29] that was combined with Configurational-Bias Monte Carlo simulation data.

	$q_{A,sat}$ mol kg^{-1}	b_A $\mathrm{Pa}^{-\nu_i}$	ν_A dimensionless	$q_{B,sat}$ mol kg^{-1}	b_B $\mathrm{Pa}^{-\nu_i}$	ν_B dimensionless
CO_2	1.84	1.89×10^{-4}	1.24	2.1	8.51×10^{-4}	0.64
CO	68	6.44×10^{-5}	0.41	0.9	8.88×10^{-15}	2.8
CH_4	2	5.77×10^{-6}	1			
H_2	15	2.05×10^{-8}				

Table 14. Reed-Ehrlich parameters for a variety of species in CuBTC at 300 K.

Molecule	$Đ_i(0)$ / 10^{-8} m^2 s^{-1}	z	ϕ_i
CO_2	0.8	5	$1.5\exp(0.01\theta_i)$
CH_4	1.7	5	$1.8\exp(0.07\theta_i)$
H_2	18	5	$1.15\exp(-0.4\theta_i)$

19. References

(1) Li, B.; Zhang, Z.; Li, Y.; Yao, K.; Zhu, Y.; Deng, Z.; Yang, F.; Zhou, X.; Li, G.; Wu, H.; Nijem, N.; Chabal, Y. J.; Lai, Z.; Han, Y.; Shi, Z.; Feng, S.; Li, J. Enhanced Binding Affinity, Remarkable Selectivity, and High Capacity of CO_2 by Dual Functionalization of a rht-Type Metal–Organic Framework, *Angew. Chem. Int. Ed.* **2012**, *51*, 1412-2415.

(2) Zhao, D.; Yuan, D.; Sun, D.; Zhou, H.-C. Stabilization of Metal-Organic Frameworks with High Surface Areas by Incorporation of Mesocaviteis and Microwindows, *J. Am. Chem. Soc.* **2009**, *131*, 91866-99188.

(3) Farha, O. K.; Yazaydın, A. Ö.; Eryazici, I.; Malliakas, C. D.; Hauser, B. G.; M.G., K.; Nguyen, S. T.; Snurr, R. Q.; Hupp, J. T. *De novo* synthesis of a metal–organic framework material featuring ultrahigh surface area and gas storage capacities *Nature Chemistry* **2010**, *2*, 944-948.

(4) Yan, Y.; Telepen, I.; Yang, S.; Lin, X.; Kockelmann, W.; Dailly, A.; Blake, A. J.; Lewis, W.; Walker, G. S.; Allan, D. R.; Barnett, S. A.; Champness, N. R.; Schröder, M. Metal−Organic Polyhedral Frameworks: High H_2 Adsorption Capacities and Neutron Powder Diffraction Studies, *J. Am. Chem. Soc.* **2010**, *132*, 4092-4094.

(5) Yuan, D.; Zhao, D.; Sun, D.; Zhou, H. C. An Isoreticular Series of Metal–Organic Frameworks with Dendritic Hexacarboxylate Ligands and Exceptionally High Gas-Uptake Capacity, *Angew. Chem. Int. Ed.* **2010**, *49*, 5357-5361.

(6) Zheng, B.; Bai, J.; Duan, J.; Wojtas, L.; Zaworotko, M. J. Enhanced CO_2 Binding Affinity of a High-Uptake *rht*-Type Metal−Organic Framework Decorated with Acylamide Groups, *J. Am. Chem. Soc.* **2011**, *133*, 748-751.

(7) Cairns, A. J.; Perman, J. A.; Wojtas, L.; Kravstov, V. C.; Alkordi, M. H.; Eddaoudi, M.; Zaworotko, M. J. Supermolecular Building Blocks (SBBs) and Crystal Design: 12-Connected Open Frameworks Based on a Molecular Cubohemioctahedron, *J. Am. Chem. Soc.* **2008**, *130*, 1560-1561.

(8) Nouar, F.; Eubank, J. F.; Bousquet, T.; Wojtas, L.; Zaworotko, M. J.; Eddaoudi, M. Supermolecular Building Blocks (SBBs) for the Design and Synthesis of Highly Porous Metal-Organic Frameworks, *J. Am. Chem. Soc.* **2008**, *130*, 1833-1835.

(9) Krishna, R.; van Baten, J. M. In silico screening of metal-organic frameworks in separation applications, *Phys. Chem. Chem. Phys.* **2011**, *13*, 10593-10616.

(10) Krishna, R.; van Baten, J. M. A comparison of the CO_2 capture characteristics of zeolites and metal-organic frameworks, *Sep. Purif. Technol.* **2012**, *87*, 120-126.

(11) Krishna, R. Diffusion in Porous Crystalline Materials, *Chem. Soc. Rev.* **2012**, *41*, 3099-3118.

(12) Krishna, R. Adsorptive separation of $CO_2/CH_4/CO$ gas mixtures at high pressures, *Microporous Mesoporous Mater.* **2012**, *156*, 217-223.

(13) Perdew, J. P.; Burke, K.; Emzerhof, M. Generalized Gradient Approximation Made Simple, *Phys. Rev. Lett.* **1996**, *77*, 3865-3868.

(14) Myers, A. L.; Prausnitz, J. M. Thermodynamics of mixed gas adsorption, *A.I.Ch.E.J.* **1965**, *11*, 121-130.

(15) Krishna, R.; van Baten, J. M. Screening of zeolite adsorbents for separation of hexane isomers: A molecular simulation study, *Sep. Purif. Technol.* **2007**, *55*, 246-255.

(16) Krishna, R.; van Baten, J. M. Using molecular simulations for screening of zeolites for separation of CO_2/CH_4 mixtures, *Chem. Eng. J.* **2007**, *133*, 121-131.

(17) Krishna, R.; van Baten, J. M. Investigating the potential of MgMOF-74 membranes for CO_2 capture, *J. Membr. Sci.* **2011**, *377*, 249-260.

(18) Krishna, R.; van Baten, J. M. Maxwell-Stefan modeling of slowing-down effects in mixed gas permeation across porous membranes, *J. Membr. Sci.* **2011**, *383*, 289-300.

(19) Chmelik, C.; van Baten, J. M.; Krishna, R. Hindering effects in diffusion of CO_2/CH_4 mixtures in ZIF-8 crystals, *J. Membr. Sci.* **2012**, *397-398*, 87-91.

(20) Mason, J. A.; Sumida, K.; Herm, Z. R.; Krishna, R.; Long, J. R. Evaluating Metal-Organic Frameworks for Post-Combustion Carbon Dioxide Capture via Temperature Swing Adsorption, *Energy Environ. Sci.* **2011**, *3*, 3030-3040.

(21) Herm, Z. R.; Krishna, R.; Long, J. R. CO_2/CH_4, CH_4/H_2 and $CO_2/CH_4/H_2$ separations at high pressures using Mg2(dobdc), *Microporous Mesoporous Mater.* **2012**, *151*, 481-487.

(22) Herm, Z. R.; Swisher, J. A.; Smit, B.; Krishna, R.; Long, J. R. Metal-Organic Frameworks as Adsorbents for Hydrogen Purification and Pre-Combustion Carbon Dioxide Capture *J. Am. Chem. Soc.* **2011**, *133*, 5664-5667.

(23) Belmabkhout, Y.; Pirngruber, G.; Jolimaitre, E.; Methivier, A. A complete experimental approach for synthesis gas separation studies using static gravimetric and column breakthrough experiments, *Adsorption* **2007**, *13*, 341-349.

(24) Yaghi, O. M. Hydrogen Storage in Metal Organic Frameworks, www.hydrogen.energy.gov/pdfs/review11/st049_yaghi_2011_p.pdf, University of California Los Angeles, California, 2011.

(25) Cavenati, S.; Grande, C. A.; Rodrigues, A. E. Adsorption Equilibrium of Methane, Carbon Dioxide, and Nitrogen on Zeolite 13X at High Pressures, *J. Chem. Eng. Data* **2004**, *49*, 1095-1101.

(26) Chowdhury, P.; Mekala, S.; Dreisbach, F.; Gumma, S. Adsorption of CO, CO_2 and CH_4 on Cu-BTC and MIL-101 Metal Organic Frameworks: Effect of Open Metal Sites and Adsorbate Polarity, *Microporous Mesoporous Mater.* **2012**, *152*, 246-252.

(27) Latroche, M.; Surblé, S.; Serre, C.; Mellot-Draznieks, C.; Llewellyn, P. L.; Lee, J. H.; Chang, J. S.; Jhung, S. H.; Férey, G. Hydrogen Storage in the Giant-Pore Metal–Organic Frameworks MIL-100 and MIL-101, *Angew. Chem. Int. Ed.* **2006**, *45*, 8227-8231.

(28) Pakseresht, S.; Kazemeini, M.; Akbarnejad, M. M. Equilibrium isotherms for CO, CO_2, CH_4 and C_2H_4 on the 5A molecular sieve by a simple volumetric apparatus, *Sep. Purif. Technol.* **2002**, *28*, 53-60.

(29) Sircar, S.; Golden, T. C. Purification of Hydrogen by Pressure Swing Adsorption, *Sep. Sci. and Technol.* **2000**, *35*, 667-687.

(30) Myers, A. L.; Monson, P. A. Adsorption in Porous Materials at High Pressure: Theory and Experiment, *Langmuir* **2002**, *18*, 10261-10273.

(31) Simmons, J. M.; Wu, H.; Zhou, W.; Yildirim, T. Carbon capture in metal–organic frameworks—a comparative study, *Energy & Environ. Sci.* **2011**, *4*, 2177-2185.

(32) Mishra, P.; Mekala, S.; Dreisbach, F.; Mandal, B.; Gumma, S. Adsorption of CO_2, CO, CH_4 and N_2 on a zinc based metal organic framework, *Sep. Purif. Technol.* **2012**, *94*, 124-130.

(33) McDonald, T. M.; D'Alessandro, D. M.; Krishna, R.; Long, J. R. Enhanced carbon dioxide capture upon incorporation of *N,N'*- dimethylethylenediamine in the metal-organic framework CuBTTri, *Chemical Science* **2011**, *2*, 2022-2028.

(34) Bloch, E. D.; Murray, L.; Queen, W. L.; Chavan, S. M.; Maximoff, S. N.; Bigi, J. P.; Krishna, R.; Peterson, V. K.; Grandjean, F.; Long, G. J.; Smit, B.; Bordiga, S.; Brown, C. M.; Long, J. R. Selective Binding of O_2 over N_2 in a Redox-Active Metal-Organic Framework with Open Iron(II) Coordination Sites, *J. Am. Chem. Soc.* **2011**, *133*, 14814-14822.

(35) He, Y.; Zhang, Z.; Xiang, S.; Fronczek, F. R.; Krishna, R.; Chen, B. A Microporous Metal-Organic Framework for Highly Selective Separation of Acetylene, Ethylene and Ethane from Methane at Room Temperature, *Chem. Eur. J.* **2012**, *18*, 613-619.

(36) He, Y.; Zhang, Z.; Xiang, S.; Wu, H.; Fronczek, F. R.; Zhou, W.; Krishna, R.; O'Keeffe, M.; Chen, B. High Separation Capacity and Selectivity of C_2 Hydrocarbons over Methane within a Microporous Metal-Organic Framework at Room Temperature, *Chem. Eur. J.* **2012**, *18*, 1901-1904.

(37) Moellmer, J.; Moeller, A.; Dreisbach, F.; Glaeser, R.; Staudt, R. High pressure adsorption of hydrogen, nitrogen, carbon dioxide and methane on the metal–organic framework HKUST-1, *Microporous Mesoporous Mater.* **2011**, *138*, 140-148.

(38) Krishna, R.; van Baten, J. M. Influence of segregated adsorption on mixture diffusion in DDR zeolite, *Chem. Phys. Lett.* **2007**, *446*, 344-349.

(39) Krishna, R.; van Baten, J. M. Segregation effects in adsorption of CO_2 containing mixtures and their consequences for separation selectivities in cage-type zeolites, *Sep. Purif. Technol.* **2008**, *61*, 414-423.

(40) Krishna, R.; van Baten, J. M. Onsager coefficients for binary mixture diffusion in nanopores, *Chem. Eng. Sci.* **2008**, *63*, 3120-3140.

(41) Krishna, R.; van Baten, J. M. Diffusion of hydrocarbon mixtures in MFI zeolite: Influence of intersection blocking, *Chem. Eng. J.* **2008**, *140*, 614-620.

(42) Ryan, P.; Farha, O. K.; Broadbelt, L. J.; Snurr, R. Q. Computational screening of metal-organic frameworks for Xenon/Krypton separation, *A.I.Ch.E.J.* **2011**, *57*, 1759-1766.

(43) Cessford, N. F.; Seaton, N. A.; Düren, T. Evaluation of Ideal Adsorbed Solution Theory as a Tool for the Design of Metal-Organic Framework Materials, *Ind. Eng. Chem. Res.* **2012**, *51*, 4911-4921.

(44) Chmelik, C.; Kärger, J.; Wiebcke, M.; Caro, J.; van Baten, J. M.; Krishna, R. Adsorption and diffusion of alkanes in CuBTC crystals investigated using infrared microscopy and molecular simulations, *Microporous Mesoporous Mater.* **2009**, *117*, 22-32.

(45) Krishna, R.; van Baten, J. M. In Silico Screening of Zeolite Membranes for CO_2 Capture, *J. Membr. Sci.* **2010**, *360*, 323-333.

(46) Krishna, R.; van Baten, J. M. Unified Maxwell-Stefan description of binary mixture diffusion in micro- and meso- porous materials, *Chem. Eng. Sci.* **2009**, *64*, 3159-3178.

(47) Krishna, R.; Long, J. R. Screening metal-organic frameworks by analysis of transient breakthrough of gas mixtures in a fixed bed adsorber, *J. Phys. Chem. C* **2011**, *115*, 12941-12950.

(48) Ho, M. T.; Allinson, G. W.; Wiley, D. E. Reducing the Cost of CO_2 Capture from Flue Gases Using Pressure Swing Adsorption, *Ind. Eng. Chem. Res.* **2008**, *47*, 4883-4890.

(49) Kumar, R. Pressure Swing Adsorption Process: Performance Optimum and Adsorbent Selection, *Ind. Eng. Chem. Res.* **1994**, *33*, 1600-1605.

(50) Krishna, R.; Baur, R. Modelling issues in zeolite based separation processes, *Sep. Purif. Technol.* **2003**, *33*, 213-254.

(51) Krishna, R.; Baur, R. Diffusion, Adsorption and Reaction in Zeolites: Modelling and Numerical Issues, http://www.science.uva.nl/research/cr/zeolite/, University of Amsterdam, Amsterdam, 11 November 2003.

(52) Kooijman, H. A.; Taylor, R. A dynamic nonequilibrium model of tray distillation columns, *A.I.Ch.E.J.* **1995**, *41*, 1852-1863.

(53) Michelsen, M. An efficient general purpose method of integration of stiff ordinary differential equations, *A.I.Ch.E.J.* **1976**, *22*, 594-597.

(54) Bulirsch, R.; Stoer, J. Numerical treatment of ordinary differential equations by extrapolation methods, *Numer. Math.* **1966**, *8*, 1-14.

(55) Britt, D.; Furukawa, H.; Wang, B.; Glover, T. G.; Yaghi, O. M. Highly efficient separation of carbon dioxide by a metal-organic framework replete with open metal sites, *Proc. Natl. Acad. Sci. U.S.A.* **2009**, *106*, 20637-20640.

(56) Bloch, E. D.; Queen, W. L.; Krishna, R.; Zadrozny, J. M.; Brown, C. M.; Long, J. R. Hydrocarbon Separations in a Metal-Organic Framework with Open Iron(II) Coordination Sites, *Science* **2012**, *335*, 1606-1610.

(57) Krishna, R.; van Baten, J. M. Diffusion of alkane mixtures in zeolites. Validating the Maxwell-Stefan formulation using MD simulations, *J. Phys. Chem. B* **2005**, *109*, 6386-6396.

(58) Krishna, R.; van Baten, J. M. Insights into diffusion of gases in zeolites gained from molecular dynamics simulations, *Microporous Mesoporous Mater.* **2008**, *109*, 91-108.

(59) Krishna, R.; Paschek, D.; Baur, R. Modelling the occupancy dependence of diffusivities in zeolites, *Microporous Mesoporous Mater.* **2004**, *76*, 233-246.

(60) Krishna, R. Describing the diffusion of guest molecules inside porous structures, *J. Phys. Chem. C* **2009**, *113*, 19756-19781.

(61) Bux, H.; Liang, F.; Li, Y.; Cravillon, J.; Wiebcke, M.; Caro, J. Zeolitic Imidazolate Framework Membrane with Molecular Sieving Properties by Microwave-Assisted Solvothermal Synthesis, *J. Am. Chem. Soc.* **2009**, *131*, 16000-16001.

(62) Li, Y.; Liang, F.; Bux, H.; Yang, W.; Caro, J. Zeolitic Imidazolate Framework ZIF-7 Based Molecular Sieve Membrane for Hydrogen Separation, *J. Membr. Sci.* **2010**, *354*, 48-54.

(63) Keskin, S. Comparing Performance of CPO and IRMOF Membranes for Gas Separations Using Atomistic Models, *Ind. Eng. Chem. Res.* **2010**, *49*, 11689-11696.

(64) Gallo, M.; Glossman-Mitnik, D. Fuel Gas Storage and Separations by Metal-Organic Frameworks: Simulated Adsorption Isotherms for H_2 and CH_4 and Their Equimolar Mixture, *J. Phys. Chem. C* **2009**, *113*, 6634-6642.

(65) Keskin, S. Molecular Simulation Study of CH_4/H_2 Mixture Separations Using Metal Organic Framework Membranes and Composites, *J. Phys. Chem. C* **2010**, *114*, 13047-13054.

(66) Wu, D.; Wang, C.; Liu, B.; Liu, D.; Yang, Q.; Zhong, C. Large-Scale Computational Screening of Metal-Organic Frameworks for CH_4/H_2 Separation, *A.I.Ch.E.J.* **2012**, *58*, 2078-2084.

(67) Dietzel, P. D. C.; Besikiotis, V.; Blom, R. Application of metal–organic frameworks with coordinatively unsaturated metal sites in storage and separation of methane and carbon dioxide, *J. Mater. Chem.* **2009**, *19*, 7362-7370.

(68) Krishna, R.; van Baten, J. M. Describing Mixture Diffusion in Microporous Materials under Conditions of Pore Saturation, *J. Phys. Chem. C* **2010**, *114*, 11557-11563.

20. Captions for Figures

Figure 1. Three different cages in the Cu-TDPAT structure: cub-O_h (violet), T-T_d (purple) and T-O_h (orange). Color scheme: copper: dark-green (shown as square pyramid); carbon: grey; oxygen: red; nitrogen, blue; void space: large violet sphere. H atoms are omitted for clarity.

Figure 2. XRD patterns of as-synthesized and outgassed samples

Figure 3. Frameworks of MIL-101, MgMOF-74, LTA-5A, and NaX.

Figure 4. 3D bar plot comparing the framework densities, pore volumes, and surface areas of LTA-5A, NaX, MgMOF-74, Cu-TDPAT, and MIL-101.

Figure 5. Comparison of the experimentally determined absolute component loadings for CO at 273 K, 288 K, and 298 K with the isotherm fits using parameters specified in Table 3.

Figure 6. Comparison of uptake of CO_2 (expressed in absolute loadings) in Cu-TDPAT, MIL101, MgMOF-74, LTA-5A and NaX. The presented data are based on the isotherm fits.

Figure 7. Comparison of isosteric heats of adsorption, Q_{st}, of CO_2 and CO in Cu-TDPAT. The calculations of, Q_{st}, are based on the use of the Clausius-Clapeyron equation, using *numerical* procedures for differentiation of the dual-Langmuir-Freundlich model.

Figure 8. (a) Configurational-bias Monte Carlo (CBMC) simulations of the pure component adsorption isotherms of CO_2, CH_4 and H_2 in CuBTC (= HKUST-1) at 300 K. The continuous solid lines in (a) are the dual-Langmuir-Freundlich fits of the pure component isotherms. (b, c) CBMC simulations of (b) 50/50 CO_2/CH_4 and (c0 15/85 CO_2/H_2 mixture adsorption in CuBTC at 300 K. The continuous solid lines are the IAST estimations of the component loadings. The CBMC simulation results are taken from the works of Krishna, van Baten and co-workers.[9, 40, 44-46]

Figure 9. Schematic of a packed bed adsorber.

Figure 10. Calculations of the superficial gas velocity at the outlet of the adsorber packed with Cu-TDPAT. The feed mixture to the adsorber is a binary CO_2/CH_4 gas mixture maintained at isothermal conditions at 298 K. In these calculations the partial pressures of CO_2 and CH_4 are taken to be equal to each other, i.e. $p_1 = p_2$ = 3.5 MPa. The *y*-axis is superficial gas velocity of the outlet gas mixture. The *x*-axis is the dimensionless breakthrough time, τ.

Figure 11. Schematic illustration of the apparatus used for the breakthrough experiments. The pressure at the exit of the packed bed corresponds to 100 kPa.

Figure 12. Experimentally determined breakthrough curves obtained for 50/50 (a) CO_2/CH_4, (b) CO_2/H_2, and (c) CO_2/N_2 mixtures using activated and regenerated samples. The smooth lines represent our breakthrough simulations; for this purpose the framework density of the sample is taken to be 1117 kg/m^3, corresponding to a sample containing 30 wt% water as in the experiments (this value determined from TGA of the sample used). The sample mass used in (a) and (b) was 100.5 mg of Cu-TDPAT crystals. For (c) the sample mass was 130 mg of Cu-TDPAT crystals. The experimental breakthrough times are corrected for the time delay between the exit of the packed bed and the entrance to the MS detection unit. The time delay was estimated to be 3.31 minutes in (a) and (b). For (c) the time delay was 3.7 minutes.

Figure 13. MD simulations of the Maxwell-Stefan diffusivities of CO_2, CH_4 and H_2 in CuBTC (= HKUST-1) at 300 K. These data are reported in the works of Krishna, van Baten and co-workers.[9, 40, 44-46, 68] The continuous solid lines are the Reed-Ehrlich fits of the diffusivities using parameter values reported in Table 14.

Figure 14. Comparison of breakthrough simulations for 50/50 (a) CO_2/CH_4, (b) CO_2/H_2, and (c) CO_2/N_2 mixtures in which intra-crystalline diffusion effects are included (indicated by crosses) with those in which equilibrium conditions are assumed (continuous solid lines). For the case in which intra-crystalline diffusion effects are included the crystallite size is taken to be 400 μm, and the diffusivities of the individual species are those obtained in the MD simulations of the Maxwell-Stefan diffusivities of CO_2, CH_4 and H_2 in CuBTC (= HKUST-1) at 300 K. The diffusivity of N_2 is assumed to have the same value as that for CH_4.

Figure 15. Breakthrough characteristics of an adsorber packed with Cu-TDPAT and maintained at isothermal conditions at 298 K. Ppm CO_2 in outlet gas as a function of the dimensionless time for various adsorbent materials. The partial pressures of CO_2 and CH_4 at the inlet to the adsorber are $p_1 = p_2 = 3.5$ MPa. The various curves are obtained with different crystal sizes.

Figure 16. Calculations using Ideal Adsorbed Solution Theory (IAST) of Myers and Prausnitz.[14] for (a) CO_2/H_2 adsorption selectivity, (b) (CO_2 + CO + CH_4) uptake capacity, expressed as moles per kg of adsorbent, in equilibrium with a quaternary $CO_2/CO/CH_4/H_2$ gas mixture maintained at isothermal conditions at 298 K, and (c) (CO_2 +CO+ CH_4) uptake capacity, expressed as moles per L of adsorbent, in equilibrium with a ternary $CO_2/CO/CH_4/H_2$ gas mixture maintained at isothermal conditions at 298 K. In these calculations the partial pressures of the three components are: $p_1//p_2/p_3/p_4$=40/5/5/50.

Figure 17. (a) Schematic of a packed bed adsorber. (b) Breakthrough characteristics a quaternary 40/5/5/50 $CO_2/CO/CH_4/H_2$ mixture in an adsorber packed with Cu-TDPAT and maintained at isothermal conditions at 298 K. Video animations of the breakthrough simulations are available as Supporting Information. (c) Ppm (CO_2 + CO+ CH_4) in outlet gas as a function of the dimensionless time for various adsorbent materials. The total operating pressure for the data in (b), and (c) corresponds to 6 MPa.

Figure 18. Influence of the total operating pressure on (a) dimensionless breakthrough times, and the number of moles of 99.95%+ pure H_2 produced (b) per kg of adsorbent material, and (c) per L of adsorbent material during the time interval 0 – τ_{break}. The breakthrough times, τ_{break}, correspond to those when the outlet gas contains 500 ppm (CO_2 + CO+ CH_4).

Figure 19. Plot of the number of moles of 99.95%+ pure H_2 produced (a) per kg of adsorbent material, (b) per L of adsorbent material during the time interval $0 - \tau_{\mathrm{break}}$ against the breakthrough time τ_{break} for packed bed adsorber with step-input of mixture with partial pressures: p_1 =2.4 MPa; p_2=0.3 MPa; p_3=0.3 MPa; p_4=3 MPa at 298 K. The breakthrough times, τ_{break}, correspond to those when the outlet gas contains 500 ppm (CO_2 + CO+ CH_4).

Figure 20. 3D bar plots showing the dependence of the number of moles of 99.95%+ pure H_2 produced (a) per kg, and (b) per L of adsorbent in a fixed bed adsorber (*z*-axes) for $CO_2/CO/CH_4/H_2$ mixture with step-input of mixture with partial pressures: p_1 =2.4 MPa; p_2=0.3 MPa; p_3=0.3 MPa; p_4=3 MPa on adsorption selectivity (*x*-axis), and the (CO_2 + CO + CH_4) uptake capacity (in mol kg^{-1} plotted on the *y*-axis).

Figure 21. Calculations using Ideal Adsorbed Solution Theory (IAST) of Myers and Prausnitz.[14] for (a) CO_2/H_2 adsorption selectivity, (b) (CO_2 + CH_4) uptake capacity, expressed as moles per kg of adsorbent, in equilibrium with a ternary $CO_2/CH_4/H_2$ 40/10/50 gas mixture maintained at isothermal conditions at 298 K, and (c) (CO_2 + CH_4) uptake capacity, expressed as moles per L of adsorbent, in equilibrium with a ternary $CO_2/CH_4/H_2$ gas mixture maintained at isothermal conditions at 298 K. In these calculations the partial pressures of the three components are: $p_1/p_2/p_3$=40/10/50

Figure 22.(a) Schematic of a packed bed adsorber. (b) Breakthrough characteristics of an adsorber packed with Cu-TDPAT and maintained at isothermal conditions at 298 K. (c) Ppm (CO_2 + CH_4) in outlet gas as a function of the dimensionless time for various adsorbent materials. The total operating pressure for the data in (b), and (c) corresponds to 4 MPa.

Figure 23. Influence of the total operating pressure on (a) dimensionless breakthrough times, and the number of moles of 99.95%+ pure H_2 produced (b) per kg of adsorbent material, and (c) per L of adsorbent material during the time interval 0 – τ_{break}. The breakthrough times, τ_{break}, correspond to those when the outlet gas contains 500 ppm (CO_2 + CH_4).

Figure 24. Plot of the number of moles of 99.95%+ pure H_2 produced (a) per kg of adsorbent material, (b) per L of adsorbent material during the time interval 0 – τ_{break} against the breakthrough time τ_{break} for packed bed adsorber with step-input of mixture with partial pressures: p_1 =2.8 MPa; p_2=0.7 MPa; p_3=3.5 MPa at 298 K. The breakthrough times, τ_{break}, correspond to those when the outlet gas contains 500 ppm (CO_2 + CH_4).

Figure 25. 3D bar plots showing the dependence of the number of moles of 99.95%+ pure H_2 produced (a) per kg, and (b) per L of adsorbent in a fixed bed adsorber (*z*-axes) for $CO_2/CH_4/H_2$ mixture with step-input of mixture with partial pressures: p_1 =2.8 MPa; p_2=0.7 MPa; p_3=3.5 MPa on the adsorption selectivity (*x*-axis), and the (CO_2 + CH_4) uptake capacity (in mol kg^{-1} plotted on the *y*-axis).

Figure 26. Calculations using Ideal Adsorbed Solution Theory (IAST) of Myers and Prausnitz[14] for (a) CO_2/H_2 adsorption selectivity, (b) CO_2 uptake capacity, expressed as moles per kg of adsorbent, in equilibrium with a binary CO_2/H_2 gas mixture maintained at isothermal conditions at 298 K, and (c) CO_2 uptake capacity, expressed as moles per L of adsorbent, in equilibrium with a binary CO_2/H_2 gas mixture maintained at isothermal conditions at 298 K. In these calculations the partial pressures of CO_2 and H_2 are taken to be $p_2 = 4p_2$.

Figure 27. (a) Schematic of a packed bed adsorber. (b) Breakthrough characteristics of an adsorber packed with Cu-TDPAT and maintained at isothermal conditions at 298 K. (c) Ppm CO_2 in outlet gas as a function of the dimensionless time for various adsorbent materials. In the calculations for (b) and (c) the partial pressures of CO_2 and H_2 at the inlet to the adsorber are $p_1 = 1.4$ MPa, $p_2 = 5.6$ MPa.

Figure 28. Influence of the total operating pressure on (a) dimensionless breakthrough times, and the number of moles of 99.95%+ pure H_2 produced (b) per kg of adsorbent material, and (c) per L of adsorbent material during the time interval 0 – τ_{break}. The breakthrough times, τ_{break}, correspond to those when the outlet gas contains 500 ppm CO_2.

Figure 29. Plot of the number of moles of 99.95%+ pure H_2 produced (a) per kg of adsorbent material, (b) per L of adsorbent material during the time interval 0 – τ_{break} against the breakthrough time τ_{break} for packed bed adsorber with step-input of a 20/80 CO_2/H_2 mixture at 298 K and total pressure of 7 MPa. The breakthrough times, τ_{break}, correspond to those when the outlet gas contains 500 ppm CO_2.

Figure 30. 3D bar plots showing the dependence of the number of moles of 99.95%+ pure H_2 produced (a) per kg, and (b) per L of adsorbent in a fixed bed adsorber (z-axes) for 20/80 CO_2/H_2 mixture at 298 K and total pressures of 7 MPa on the adsorption selectivity (x-axis), and the CO_2 uptake capacity (expressed in mol kg^{-1} plotted on the y-axis).

Figure 31. Calculations using Ideal Adsorbed Solution Theory (IAST) of Myers and Prausnitz.[14] for (a) CO_2/CH_4 adsorption selectivity, (b) CO_2 uptake capacity, expressed as moles per kg of adsorbent, in equilibrium with a binary CO_2/CH_4 gas mixture maintained at isothermal conditions at 298 K, and (c) CO_2 uptake capacity, expressed as moles per L of adsorbent, in equilibrium with a binary CO_2/CH_4 gas mixture maintained at isothermal conditions at 298 K. In these calculations the partial pressures of CO_2 and CH_4 are taken to be equal to each other, i.e. $p_1 = p_2$.

Figure 32. (a) Schematic of a packed bed adsorber. (b) Breakthrough characteristics of an adsorber packed with Cu-TDPAT and maintained at isothermal conditions at 298 K. (c) Ppm CO_2 in outlet gas as a function of the dimensionless time for various adsorbent materials. In the calculations for (b) and (c) the partial pressures of CO_2 and CH_4 at the inlet to the adsorber are $p_1 = p_2 = 3.5$ MPa.

Figure 33. Influence of the total operating pressure on (a) dimensionless breakthrough times, and the number of moles of 99.5%+ pure CH_4 produced (b) per kg of adsorbent material, and (c) per L of adsorbent material during the time interval $0 - \tau_{\text{break}}$. The breakthrough times, τ_{break}, correspond to those when the outlet gas contains < 500 ppm CO_2.

Figure 34. Plot of the number of moles of 99.5%+ pure CH_4 produced (a) per kg of adsorbent material, (b) per L of adsorbent material during the time interval $0 - \tau_{\text{break}}$ against the breakthrough time τ_{break} for packed bed adsorber with step-input of a 50/50 CO_2/CH_4 mixture at 298 K and. The breakthrough times, τ_{break}, correspond to those when the outlet gas contains 500 ppm CO_2.

Figure 35. 3D bar plots showing the dependence of the number of moles of 99.5%+ pure CH_4 produced (a) per kg, and (b) per L of adsorbent in a fixed bed adsorber (*z*-axes) for equimolar CO_2/CH_4 mixture total pressure of 7 MPa on the adsorption selectivity (*x*-axis), and the CO_2 uptake capacity (in mol kg^{-1} plotted on the *y*-axis).

Figure 36. Calculations using Ideal Adsorbed Solution Theory (IAST) of Myers and Prausnitz.[14] for (a) CH_4/H_2 adsorption selectivity, (b) CH_4 uptake capacity, expressed as moles per kg of adsorbent, in equilibrium with a binary CH_4/H_2 gas mixture maintained at isothermal conditions at 298 K, and (c) CH_4 uptake capacity, expressed as moles per L of adsorbent, in equilibrium with a binary CH_4/H_2 gas mixture maintained at isothermal conditions at 298 K. In these calculations the partial pressures of CH_4 and H_2 are taken to be $p_1 = p_2$.

Figure 37. (a) Schematic of a packed bed adsorber. (b) Breakthrough characteristics of an adsorber packed with Cu-TDPAT and maintained at isothermal conditions at 298 K. (c) Ppm CH_4 in outlet gas as a function of the dimensionless time for various adsorbent materials. In the calculations for (b) and (c) the partial pressures of CH_4 and H_2 at the inlet to the adsorber are $p_1 = p_2 = 3.5$ MPa.

Figure 38. Influence of the total operating pressure on (a) dimensionless breakthrough times, and the number of moles of 99.95%+ pure H_2 produced (b) per kg of adsorbent material, and (c) per L of adsorbent material during the time interval $0 - \tau_{\text{break}}$. The breakthrough times, τ_{break}, correspond to those when the outlet gas contains 500 ppm CH_4.

Figure 39. Plot of the number of moles of 99.95%+ pure H_2 produced (a) per kg of adsorbent material, (b) per L of adsorbent material during the time interval 0 – τ_{break} against the breakthrough time τ_{break} for packed bed adsorber with step-input of a 50/5 CH_4/H_2 mixture at 298 K and total pressures of 7 MPa. The breakthrough times, τ_{break}, correspond to those when the outlet gas contains 500 ppm CH_4.

Figure 40. 3D bar plots showing the dependence of the number of moles of 99.95%+ pure H_2 produced (a) per kg and (b) per L of adsorbent in a fixed bed adsorber (*z*-axes) for equimolar CH_4/H_2 mixture at 298 K and total pressure of 7 MPa on the adsorption selectivity (*x*-axis), and the CH_4 uptake capacity (expressed in mol kg^{-1} plotted on the *y*-axis).

Figure 1

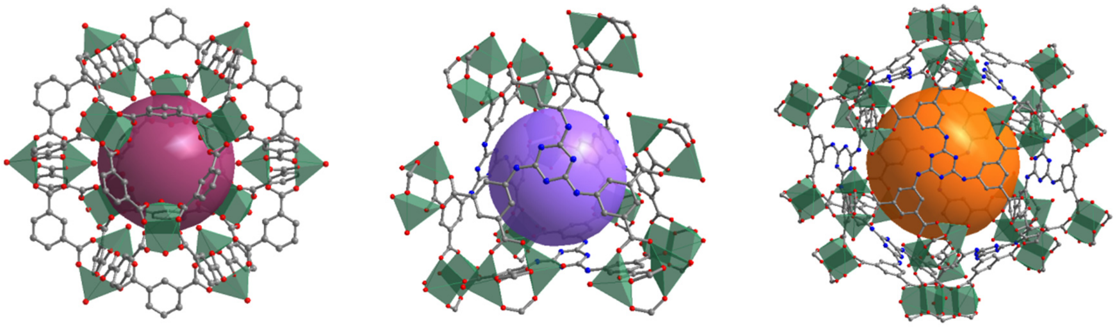

Figure 2

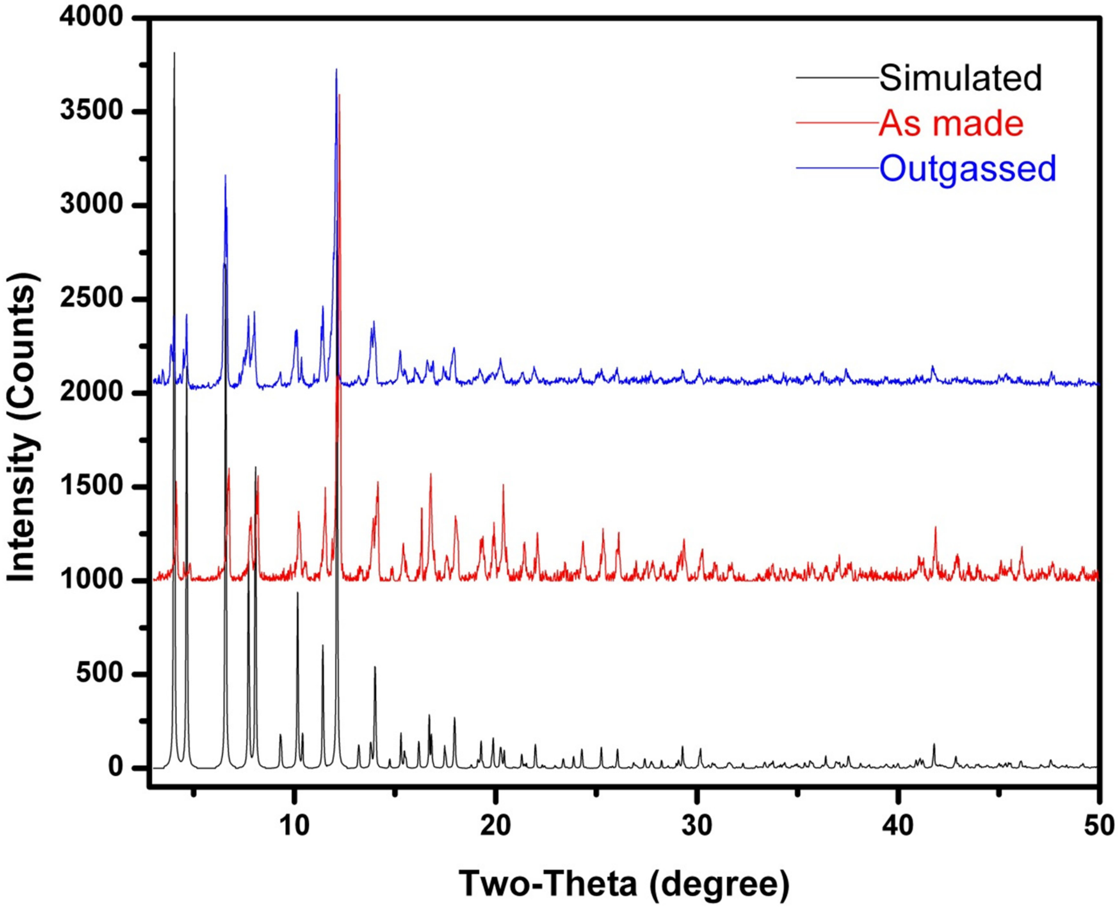

Simulated
As made
Outgassed
Intensity (Counts)
Two-Theta (degree)
0
500
1000
1500
2000
2500
3000
3500
4000
10
20
30
40
50

Figure 3

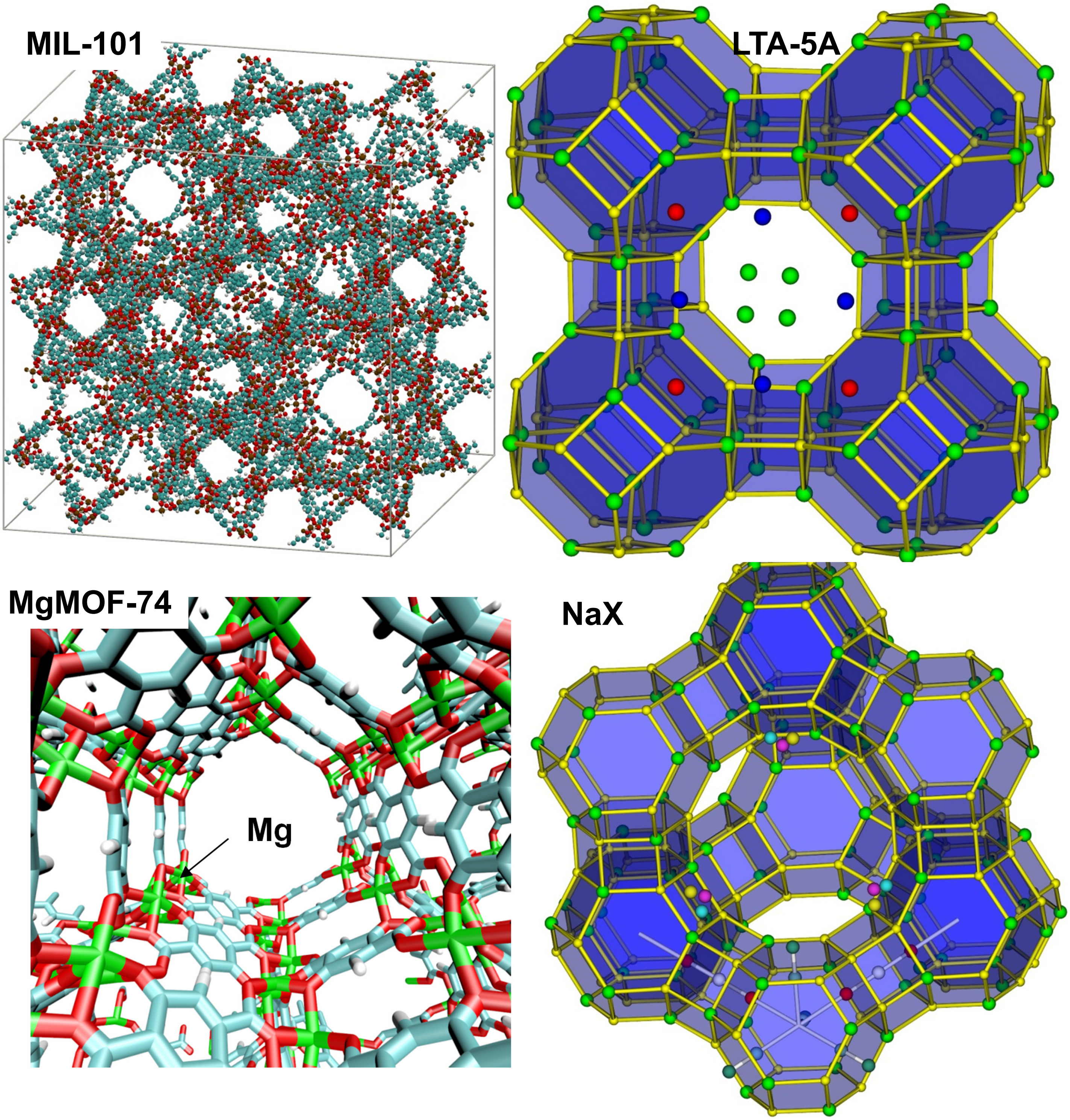

Figure 4

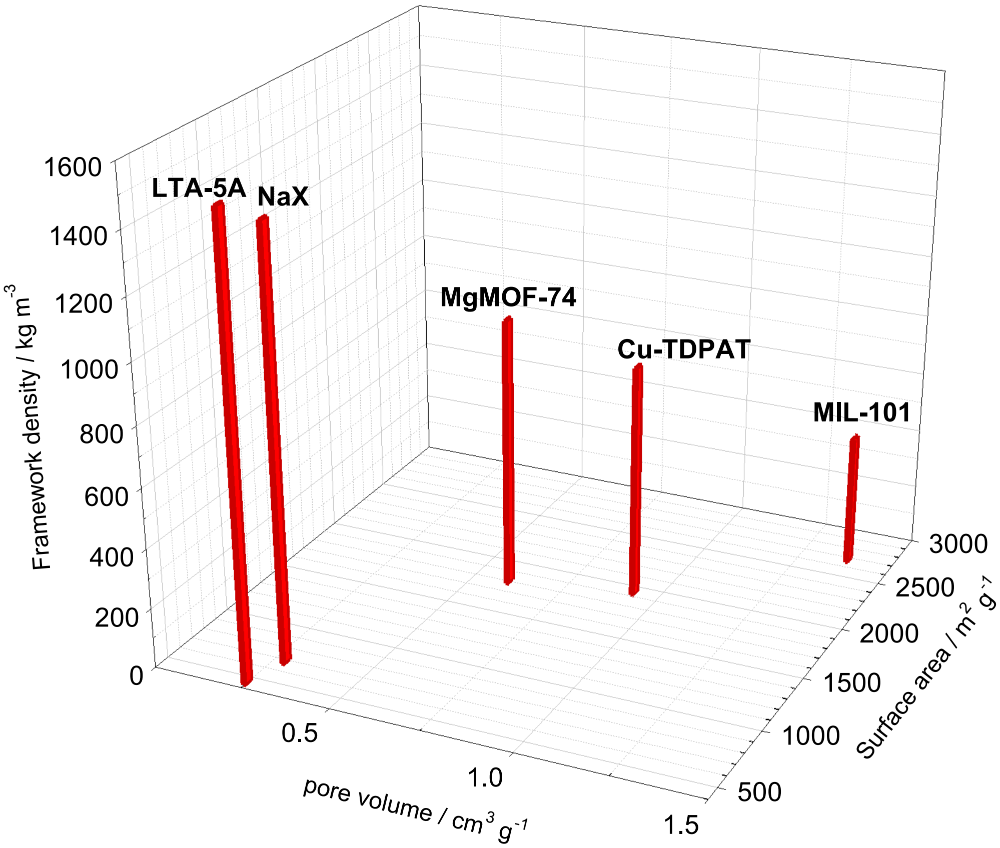

Framework density / kg m-3
1600
1400
1200
1000
800
600
400
200
0
pore volume / cm3 g-1
0.5
1.0
1.5
Surface area / m2 g-1
500
1000
1500
2000
2500
3000
LTA-5A
NaX
MgMOF-74
Cu-TDPAT
MIL-101

Figure 5

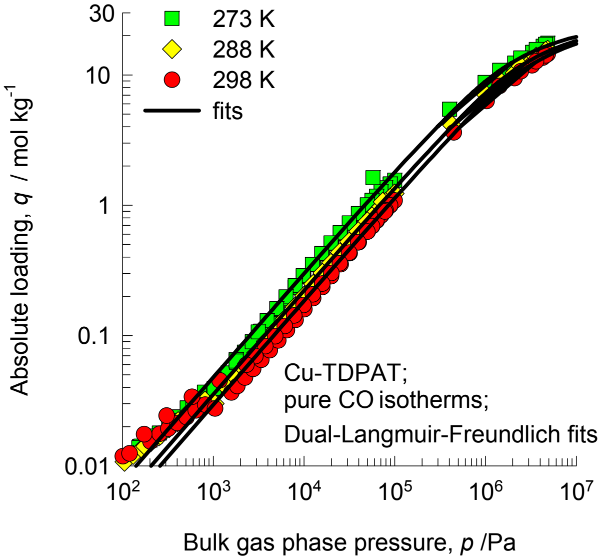

30
10
1
0.1
0.01
Absolute loading, q / mol kg-1
273 K
288 K
298 K
fits
Cu-TDPAT;
pure CO isotherms;
Dual-Langmuir-Freundlich fits
10²
10³
10⁴
10⁵
10⁶
10⁷
Bulk gas phase pressure, p /Pa

Figure 6

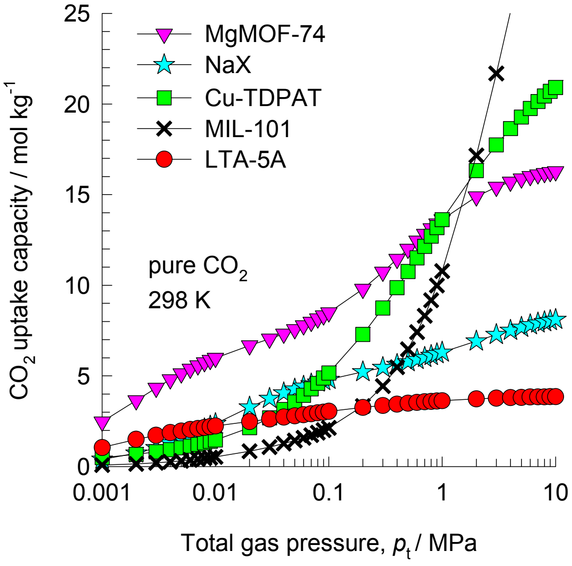

CO2 uptake capacity / mol kg-1
25
20
15
10
5
0
0.001
0.01
0.1
1
10
Total gas pressure, pt / MPa
MgMOF-74
NaX
Cu-TDPAT
MIL-101
LTA-5A
pure CO2
298 K

Figure 7

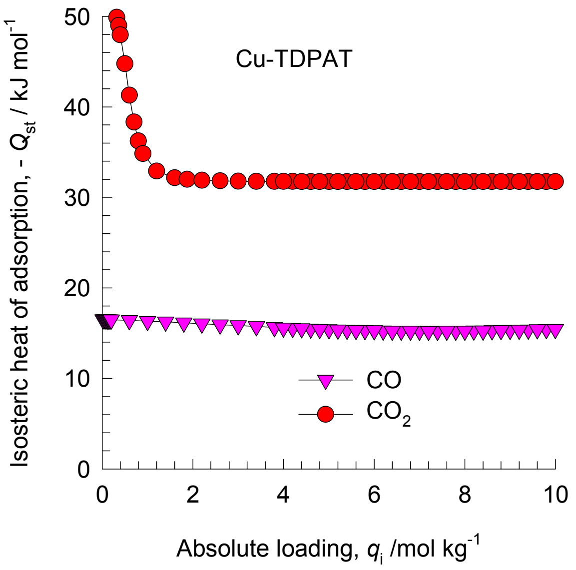
Cu-TDPAT
Isosteric heat of adsorption, - Q_{st} / kJ mol^{-1}
50
40
30
20
10
0
0
2
4
6
8
10
Absolute loading, q_i /mol kg^{-1}
CO
CO_2

Figure 8

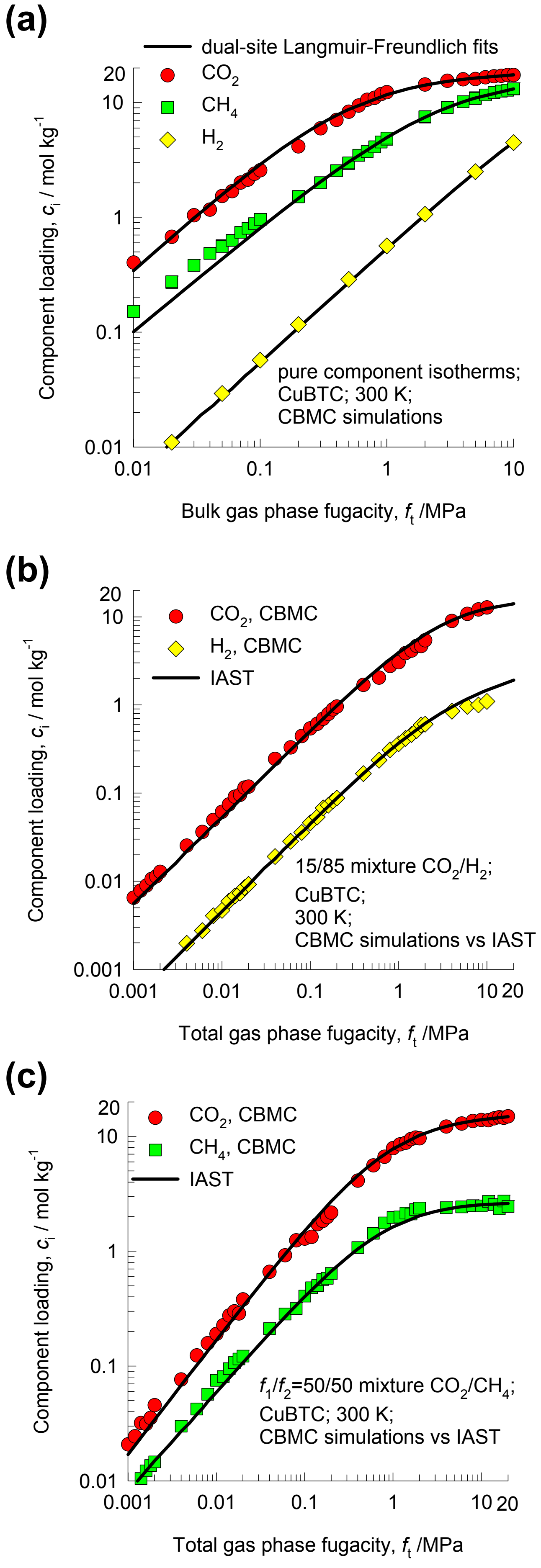
(a)
dual-site Langmuir-Freundlich fits
CO2
CH4
H2
pure component isotherms;
CuBTC; 300 K;
CBMC simulations
Component loading, ci / mol kg-1
20
10
1
0.1
0.01
0.01
0.1
1
10
Bulk gas phase fugacity, ft /MPa
(b)
CO2, CBMC
H2, CBMC
IAST
15/85 mixture CO2/H2;
CuBTC;
300 K;
CBMC simulations vs IAST
Component loading, ci / mol kg-1
20
10
1
0.1
0.01
0.001
0.001
0.01
0.1
1
10
20
Total gas phase fugacity, ft /MPa
(c)
CO2, CBMC
CH4, CBMC
IAST
f1/f2=50/50 mixture CO2/CH4;
CuBTC; 300 K;
CBMC simulations vs IAST
Component loading, ci / mol kg-1
20
10
1
0.1
0.01
0.001
0.01
0.1
1
10
20
Total gas phase fugacity, ft /MPa

Figure 9

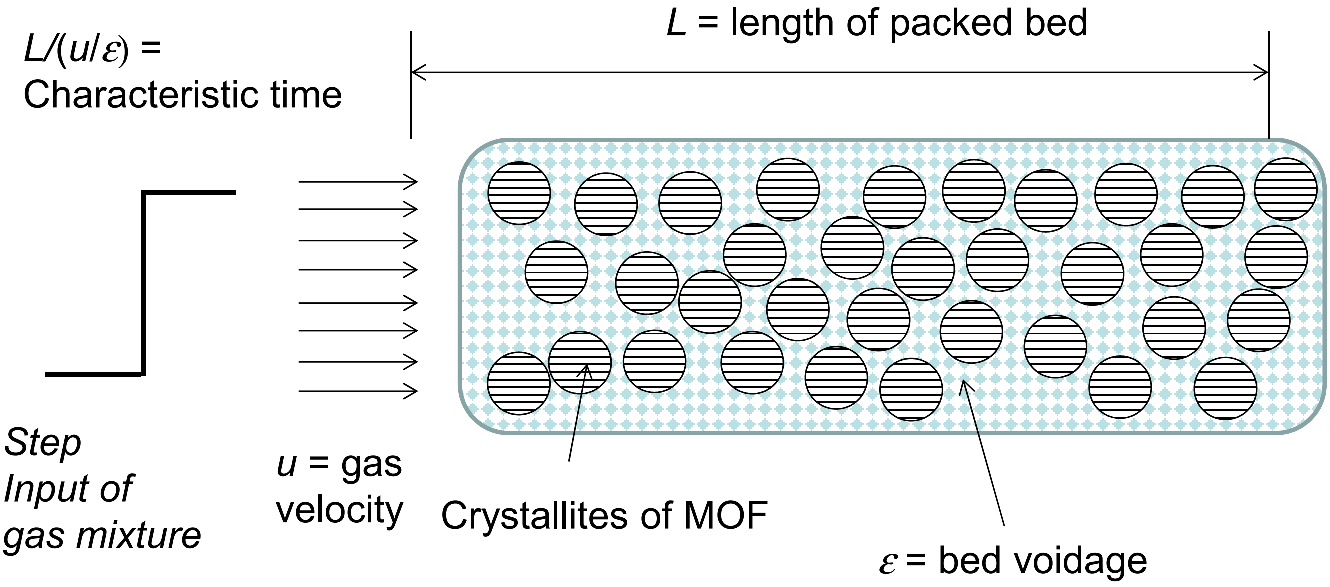
L = length of packed bed
L/(u/ε) =
Characteristic time
Step
Input of
gas mixture
u = gas
velocity
Crystallites of MOF
ε = bed voidage

Figure 10

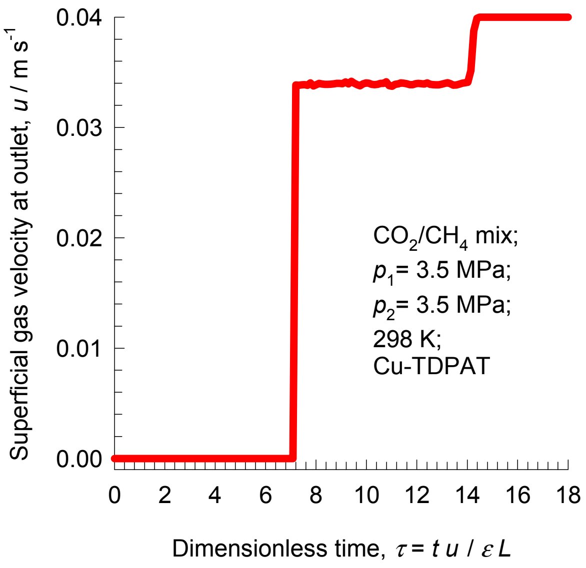
0.04
0.03
0.02
0.01
0.00
Superficial gas velocity at outlet, u / m s^{-1}
0
2
4
6
8
10
12
14
16
18
Dimensionless time, $\tau = t\,u\,/\,\varepsilon L$
CO_2/CH_4 mix;
p_1= 3.5 MPa;
p_2= 3.5 MPa;
298 K;
Cu-TDPAT

Figure 11

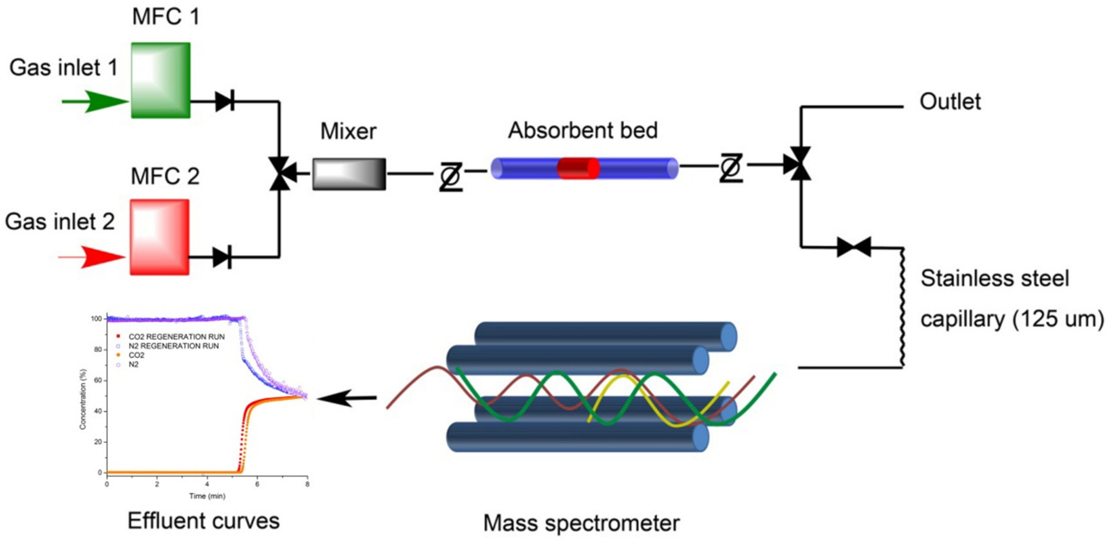
MFC 1
Gas inlet 1
MFC 2
Gas inlet 2
Mixer
Absorbent bed
Outlet
Stainless steel
capillary (125 um)
100
80
60
40
20
0
Concentration (%)
0
2
4
6
8
Time (min)
CO2 REGENERATION RUN
N2 REGENERATION RUN
CO2
N2
Effluent curves
Mass spectrometer

Figure 12

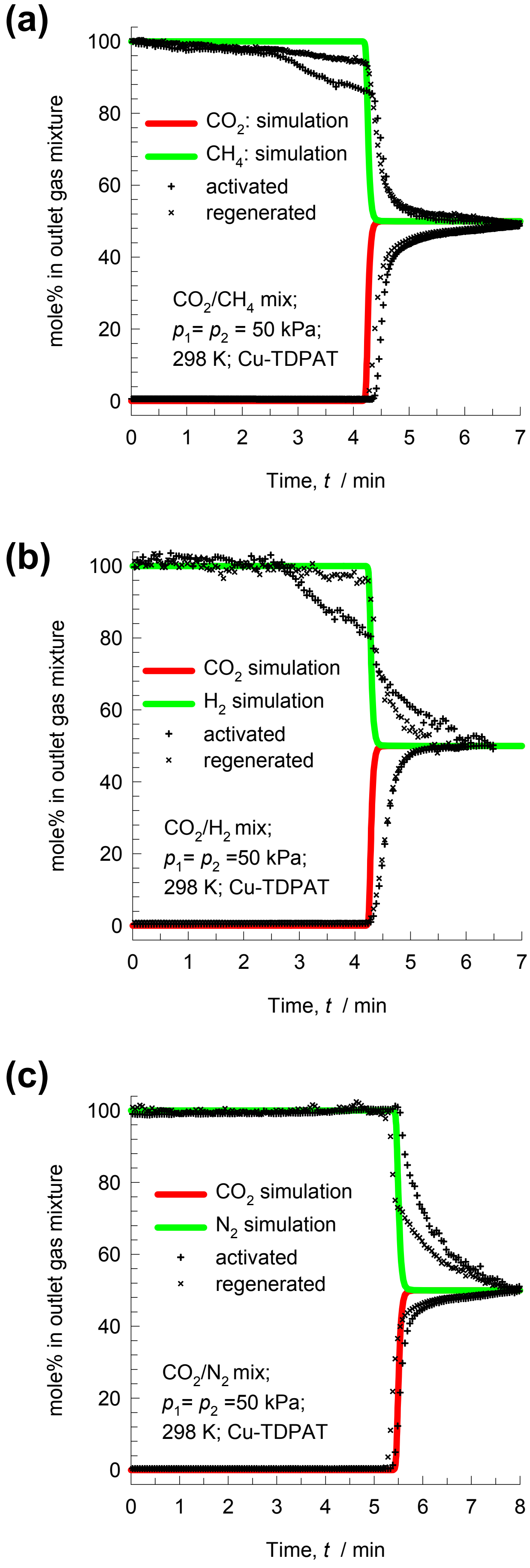

(a)
100
80
60
40
20
0
mole% in outlet gas mixture
CO_2: simulation
CH_4: simulation
+ activated
× regenerated
CO_2/CH_4 mix;
p_1= p_2 = 50 kPa;
298 K; Cu-TDPAT
0 1 2 3 4 5 6 7
Time, t / min
(b)
100
80
60
40
20
0
mole% in outlet gas mixture
CO_2 simulation
H_2 simulation
+ activated
× regenerated
CO_2/H_2 mix;
p_1= p_2 =50 kPa;
298 K; Cu-TDPAT
0 1 2 3 4 5 6 7
Time, t / min
(c)
100
80
60
40
20
0
mole% in outlet gas mixture
CO_2 simulation
N_2 simulation
+ activated
× regenerated
CO_2/N_2 mix;
p_1= p_2 =50 kPa;
298 K; Cu-TDPAT
0 1 2 3 4 5 6 7 8
Time, t / min

Figure 13

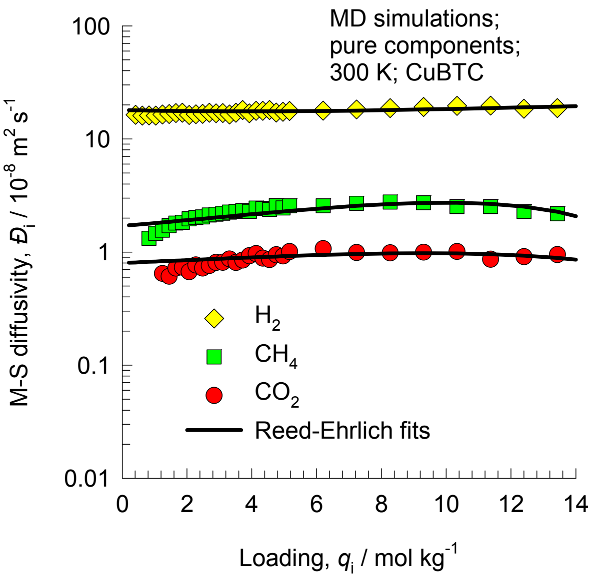
MD simulations;
pure components;
300 K; CuBTC
M-S diffusivity, $Đ_i$ / 10^{-8} m^2 s^{-1}
100
10
1
0.1
0.01
Loading, q_i / mol kg^{-1}
0
2
4
6
8
10
12
14
H_2
CH_4
CO_2
Reed-Ehrlich fits

Figure 14

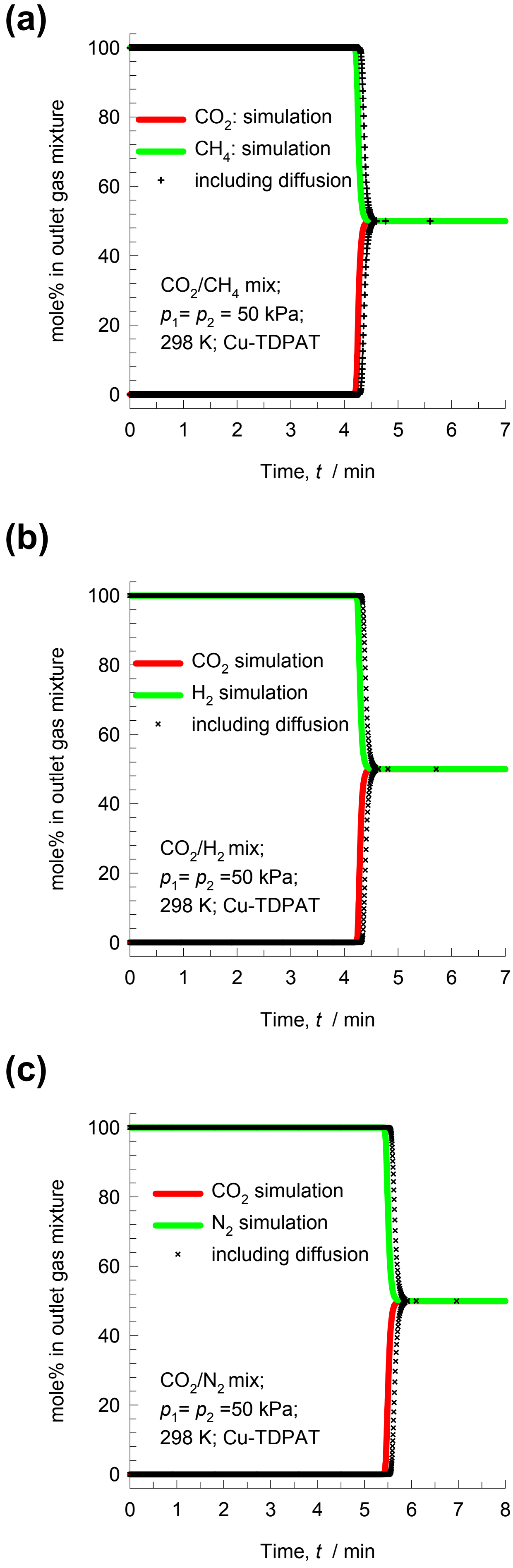
(a)
100
80
60
40
20
0
mole% in outlet gas mixture
CO_2: simulation
CH_4: simulation
+ including diffusion
CO_2/CH_4 mix;
$p_1 = p_2$ = 50 kPa;
298 K; Cu-TDPAT
0
1
2
3
4
5
6
7
Time, *t* / min
(b)
100
80
60
40
20
0
mole% in outlet gas mixture
CO_2 simulation
H_2 simulation
× including diffusion
CO_2/H_2 mix;
$p_1 = p_2$ =50 kPa;
298 K; Cu-TDPAT
0
1
2
3
4
5
6
7
Time, *t* / min
(c)
100
80
60
40
20
0
mole% in outlet gas mixture
CO_2 simulation
N_2 simulation
× including diffusion
CO_2/N_2 mix;
$p_1 = p_2$ =50 kPa;
298 K; Cu-TDPAT
0
1
2
3
4
5
6
7
8
Time, *t* / min

Figure 15

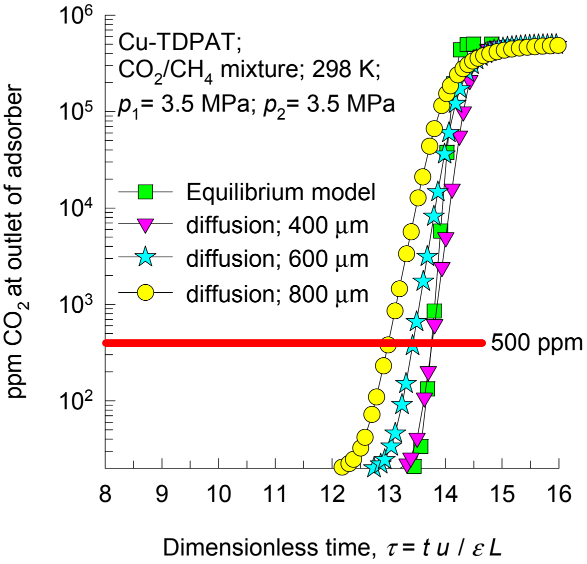
Cu-TDPAT;
CO$_2$/CH$_4$ mixture; 298 K;
p_1= 3.5 MPa; p_2= 3.5 MPa
Equilibrium model
diffusion; 400 µm
diffusion; 600 µm
diffusion; 800 µm
500 ppm
ppm CO$_2$ at outlet of adsorber
10^2
10^3
10^4
10^5
10^6
8
9
10
11
12
13
14
15
16
Dimensionless time, $\tau = t\,u\,/\,\varepsilon L$

Figure 16

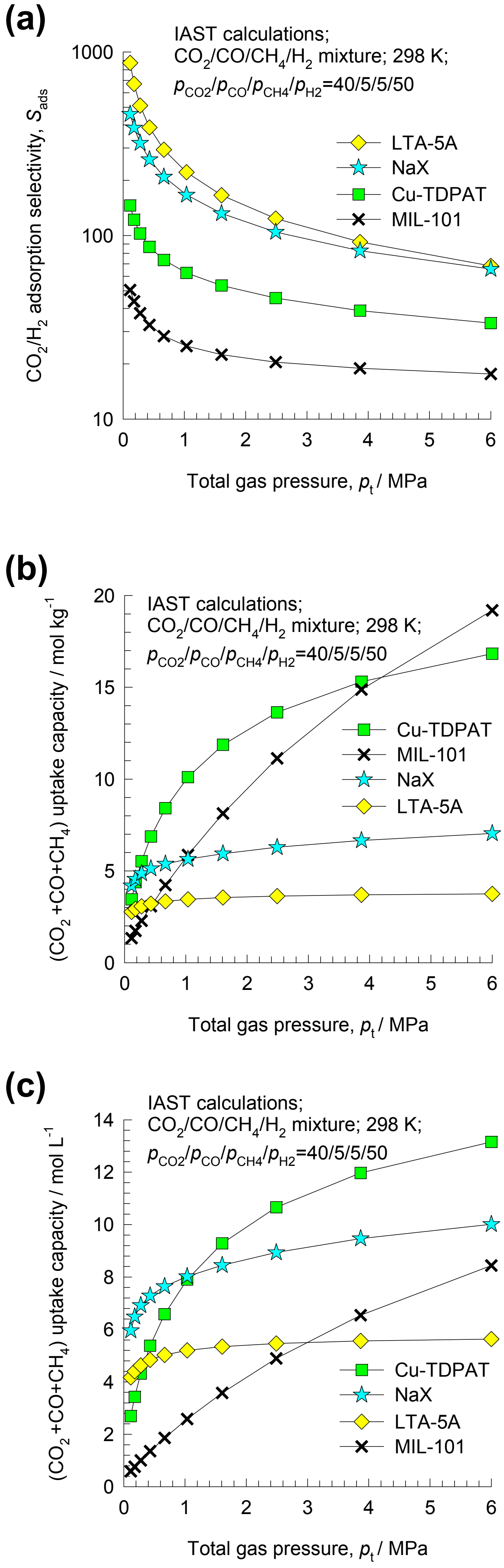
(a)
IAST calculations;
$CO_2/CO/CH_4/H_2$ mixture; 298 K;
$p_{CO2}/p_{CO}/p_{CH4}/p_{H2}$=40/5/5/50
LTA-5A
NaX
Cu-TDPAT
MIL-101
CO_2/H_2 adsorption selectivity, S_{ads}
1000
100
10
0
1
2
3
4
5
6
Total gas pressure, p_t / MPa
(b)
IAST calculations;
$CO_2/CO/CH_4/H_2$ mixture; 298 K;
$p_{CO2}/p_{CO}/p_{CH4}/p_{H2}$=40/5/5/50
Cu-TDPAT
MIL-101
NaX
LTA-5A
$(CO_2 + CO + CH_4)$ uptake capacity / mol kg^{-1}
20
15
10
5
0
0
1
2
3
4
5
6
Total gas pressure, p_t / MPa
(c)
IAST calculations;
$CO_2/CO/CH_4/H_2$ mixture; 298 K;
$p_{CO2}/p_{CO}/p_{CH4}/p_{H2}$=40/5/5/50
Cu-TDPAT
NaX
LTA-5A
MIL-101
$(CO_2 + CO + CH_4)$ uptake capacity / mol L^{-1}
14
12
10
8
6
4
2
0
0
1
2
3
4
5
6
Total gas pressure, p_t / MPa

Figure 17

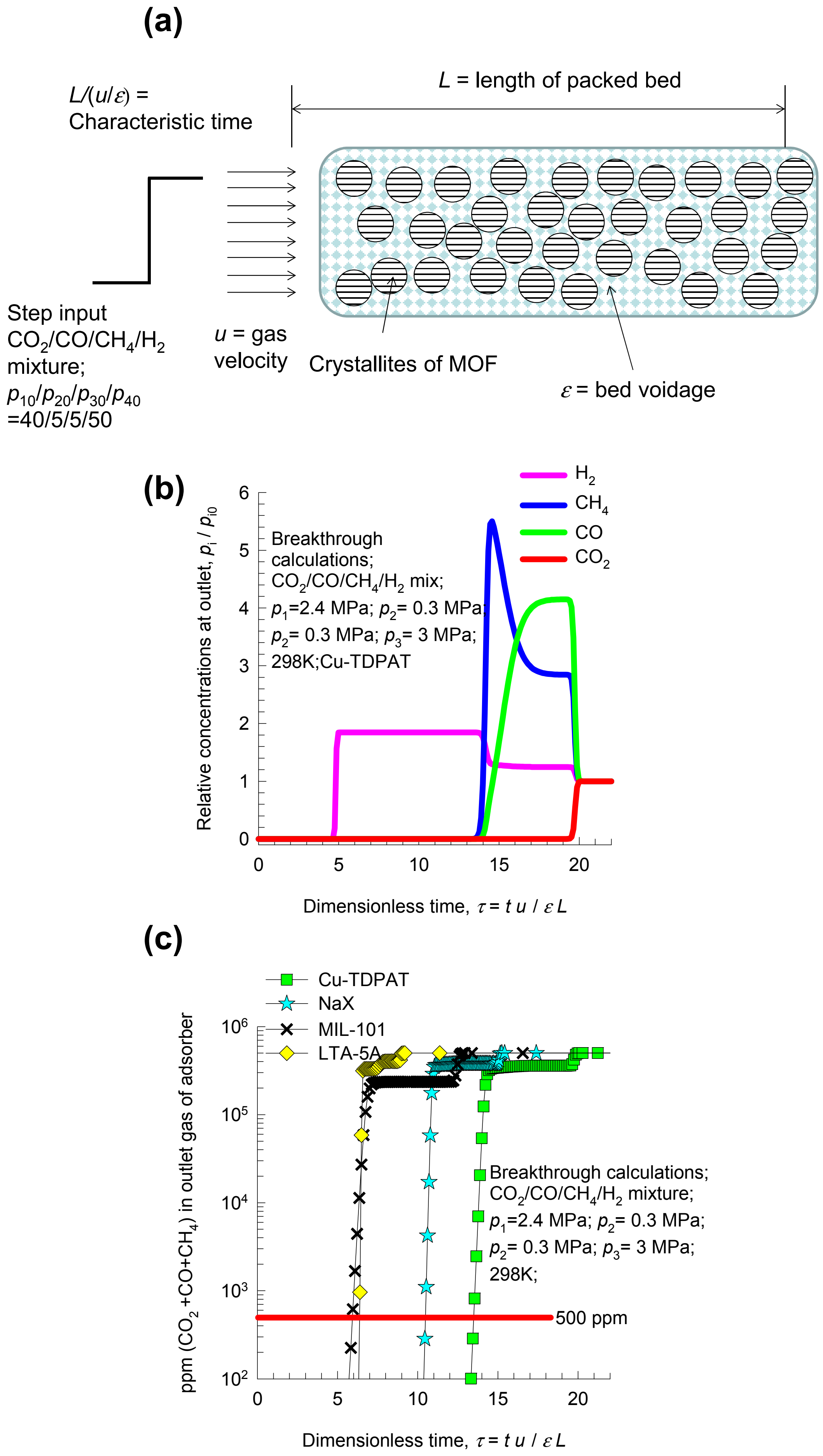
(a)
L/(u/ε) = Characteristic time
L = length of packed bed
Step input CO2/CO/CH4/H2 mixture; p10/p20/p30/p40 =40/5/5/50
u = gas velocity
Crystallites of MOF
ε = bed voidage
(b)
H2
CH4
CO
CO2
Breakthrough calculations; CO2/CO/CH4/H2 mix; p1=2.4 MPa; p2= 0.3 MPa; p2= 0.3 MPa; p3= 3 MPa; 298K;Cu-TDPAT
Relative concentrations at outlet, pi / pi0
0
1
2
3
4
5
6
0
5
10
15
20
Dimensionless time, τ = t u / ε L
(c)
Cu-TDPAT
NaX
MIL-101
LTA-5A
Breakthrough calculations; CO2/CO/CH4/H2 mixture; p1=2.4 MPa; p2= 0.3 MPa; p2= 0.3 MPa; p3= 3 MPa; 298K;
500 ppm
ppm (CO2 +CO+CH4) in outlet gas of adsorber
10^2
10^3
10^4
10^5
10^6
0
5
10
15
20
Dimensionless time, τ = t u / ε L

Figure 18

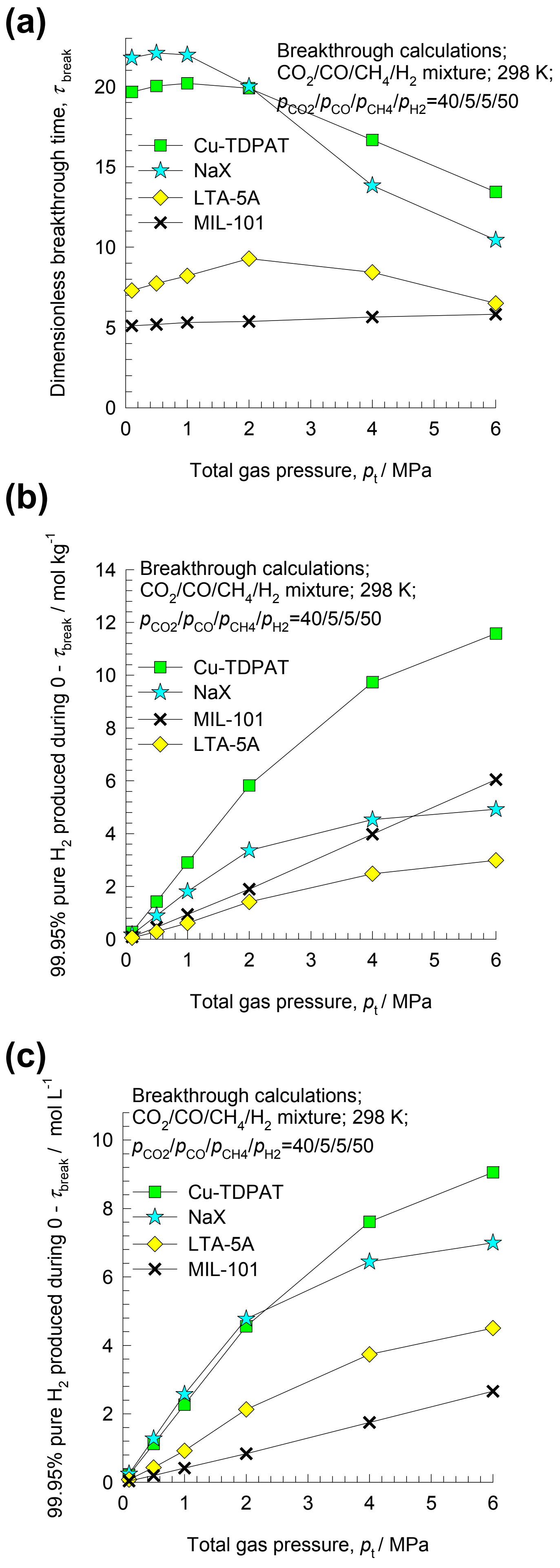
(a)
Breakthrough calculations;
$CO_2/CO/CH_4/H_2$ mixture; 298 K;
$p_{CO2}/p_{CO}/p_{CH4}/p_{H2}$=40/5/5/50
Cu-TDPAT
NaX
LTA-5A
MIL-101
Dimensionless breakthrough time, τ_{break}
0
5
10
15
20
0
1
2
3
4
5
6
Total gas pressure, p_t / MPa
(b)
Breakthrough calculations;
$CO_2/CO/CH_4/H_2$ mixture; 298 K;
$p_{CO2}/p_{CO}/p_{CH4}/p_{H2}$=40/5/5/50
Cu-TDPAT
NaX
MIL-101
LTA-5A
99.95% pure H_2 produced during 0 - τ_{break} / mol kg^{-1}
0
2
4
6
8
10
12
14
0
1
2
3
4
5
6
Total gas pressure, p_t / MPa
(c)
Breakthrough calculations;
$CO_2/CO/CH_4/H_2$ mixture; 298 K;
$p_{CO2}/p_{CO}/p_{CH4}/p_{H2}$=40/5/5/50
Cu-TDPAT
NaX
LTA-5A
MIL-101
99.95% pure H_2 produced during 0 - τ_{break} / mol L^{-1}
0
2
4
6
8
10
0
1
2
3
4
5
6
Total gas pressure, p_t / MPa

Figure 19

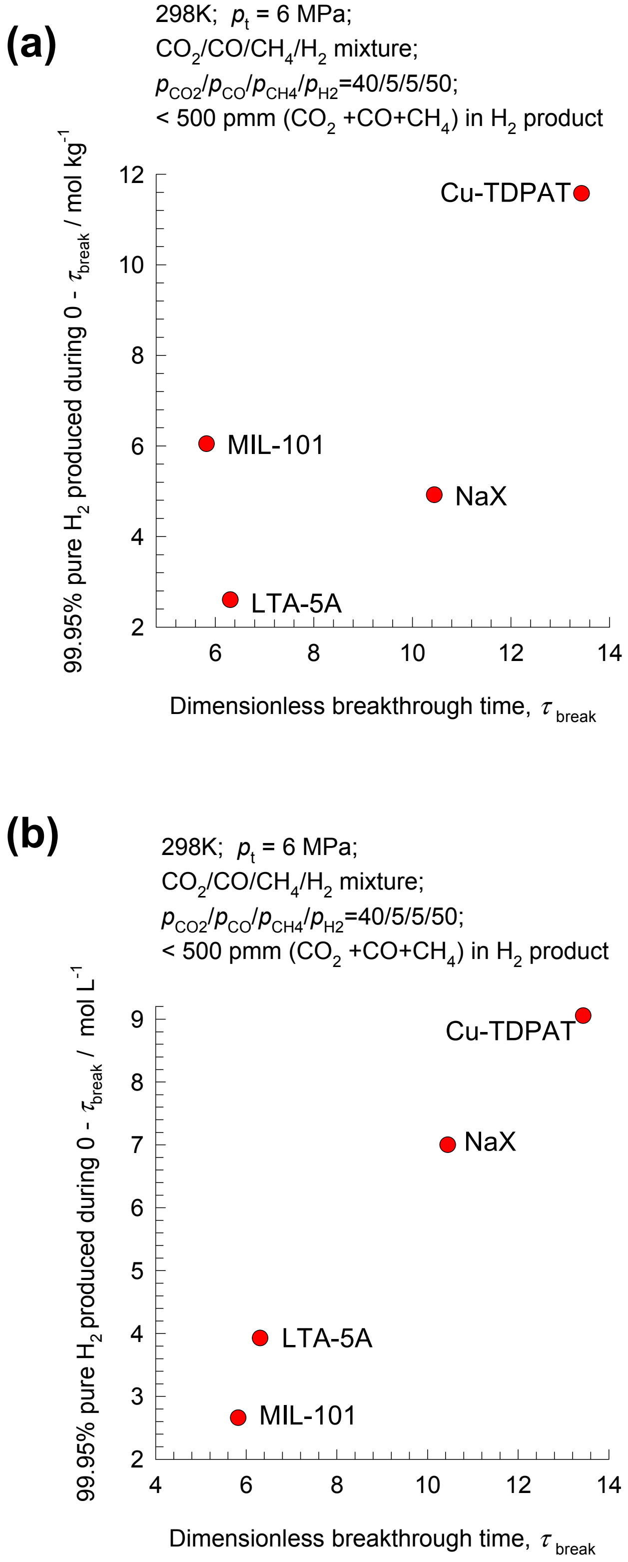
(a)
298K; p_t = 6 MPa;
$CO_2/CO/CH_4/H_2$ mixture;
$p_{CO2}/p_{CO}/p_{CH4}/p_{H2}$=40/5/5/50;
< 500 pmm (CO_2 +CO+CH_4) in H_2 product
99.95% pure H_2 produced during 0 - τ_{break} / mol kg^{-1}
Dimensionless breakthrough time, τ_{break}
12
10
8
6
4
2
6
8
10
12
14
Cu-TDPAT
MIL-101
NaX
LTA-5A
(b)
298K; p_t = 6 MPa;
$CO_2/CO/CH_4/H_2$ mixture;
$p_{CO2}/p_{CO}/p_{CH4}/p_{H2}$=40/5/5/50;
< 500 pmm (CO_2 +CO+CH_4) in H_2 product
99.95% pure H_2 produced during 0 - τ_{break} / mol L^{-1}
Dimensionless breakthrough time, τ_{break}
9
8
7
6
5
4
3
2
4
6
8
10
12
14
Cu-TDPAT
NaX
LTA-5A
MIL-101

Figure 20

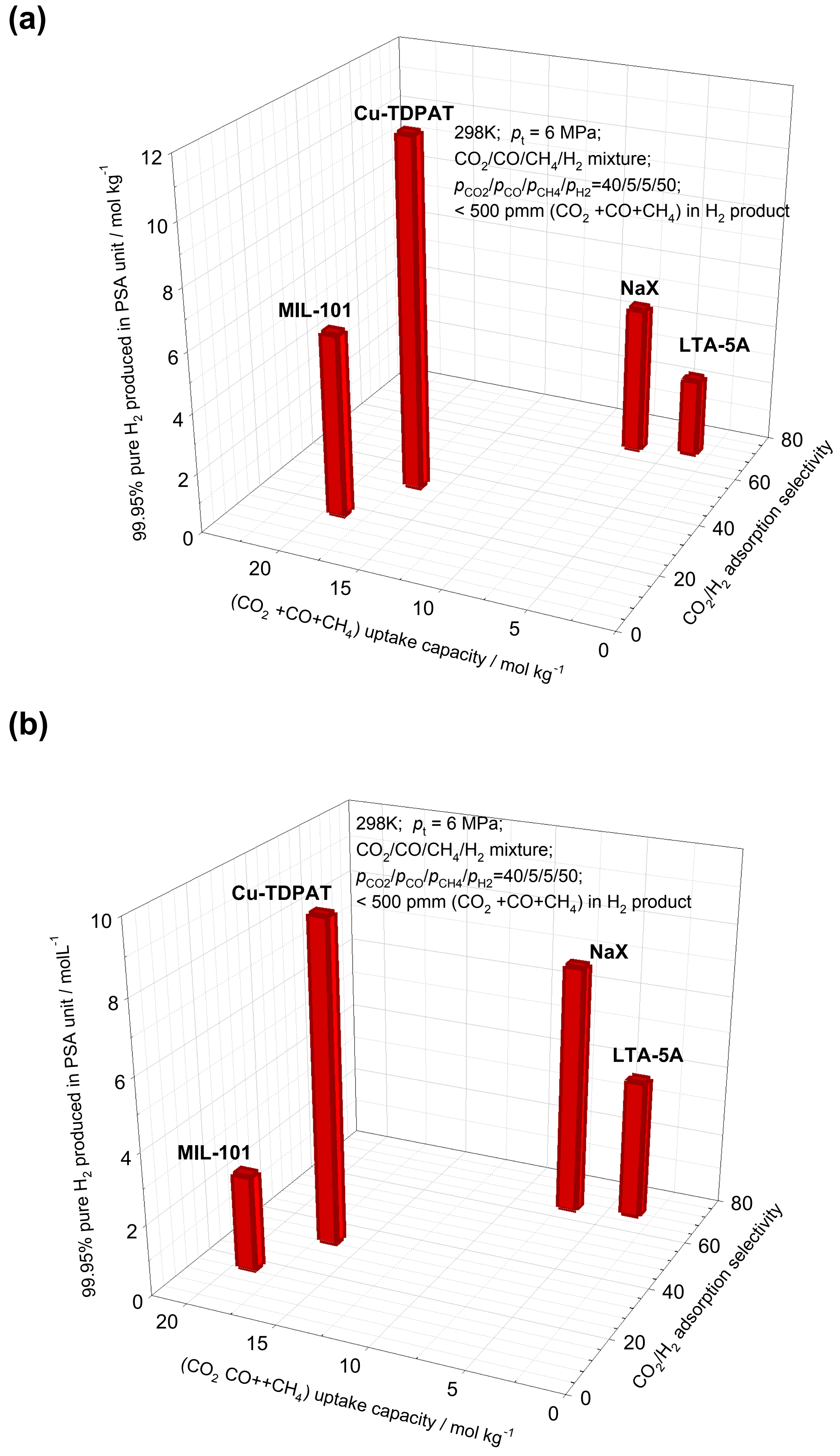
(a)
298K; p_t = 6 MPa;
$CO_2/CO/CH_4/H_2$ mixture;
$p_{CO2}/p_{CO}/p_{CH4}/p_{H2}$=40/5/5/50;
< 500 pmm (CO_2 +CO+CH_4) in H_2 product
Cu-TDPAT
MIL-101
NaX
LTA-5A
99.95% pure H_2 produced in PSA unit / mol kg^{-1}
0
2
4
6
8
10
12
(CO_2 +CO+CH_4) uptake capacity / mol kg^{-1}
20
15
10
5
0
CO_2/H_2 adsorption selectivity
0
20
40
60
80
(b)
298K; p_t = 6 MPa;
$CO_2/CO/CH_4/H_2$ mixture;
$p_{CO2}/p_{CO}/p_{CH4}/p_{H2}$=40/5/5/50;
< 500 pmm (CO_2 +CO+CH_4) in H_2 product
Cu-TDPAT
MIL-101
NaX
LTA-5A
99.95% pure H_2 produced in PSA unit / $molL^{-1}$
0
2
4
6
8
10
(CO_2 CO++CH_4) uptake capacity / mol kg^{-1}
20
15
10
5
0
CO_2/H_2 adsorption selectivity
0
20
40
60
80

Figure 21

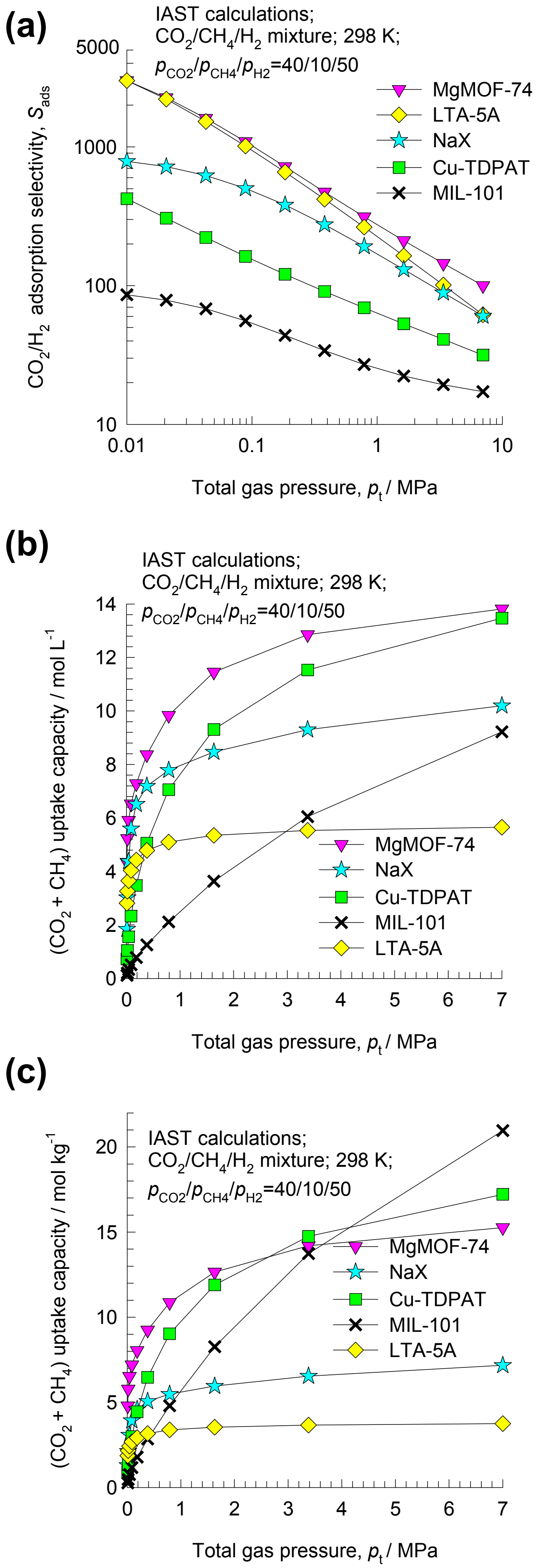

(a)
IAST calculations;
$CO_2/CH_4/H_2$ mixture; 298 K;
$p_{CO2}/p_{CH4}/p_{H2}$=40/10/50
CO_2/H_2 adsorption selectivity, S_{ads}
5000
1000
100
10
0.01
0.1
1
10
Total gas pressure, p_t / MPa
MgMOF-74
LTA-5A
NaX
Cu-TDPAT
MIL-101
(b)
IAST calculations;
$CO_2/CH_4/H_2$ mixture; 298 K;
$p_{CO2}/p_{CH4}/p_{H2}$=40/10/50
$(CO_2 + CH_4)$ uptake capacity / mol L^{-1}
14
12
10
8
6
4
2
0
0
1
2
3
4
5
6
7
Total gas pressure, p_t / MPa
MgMOF-74
NaX
Cu-TDPAT
MIL-101
LTA-5A
(c)
IAST calculations;
$CO_2/CH_4/H_2$ mixture; 298 K;
$p_{CO2}/p_{CH4}/p_{H2}$=40/10/50
$(CO_2 + CH_4)$ uptake capacity / mol kg^{-1}
20
15
10
5
0
0
1
2
3
4
5
6
7
Total gas pressure, p_t / MPa
MgMOF-74
NaX
Cu-TDPAT
MIL-101
LTA-5A

Figure 22

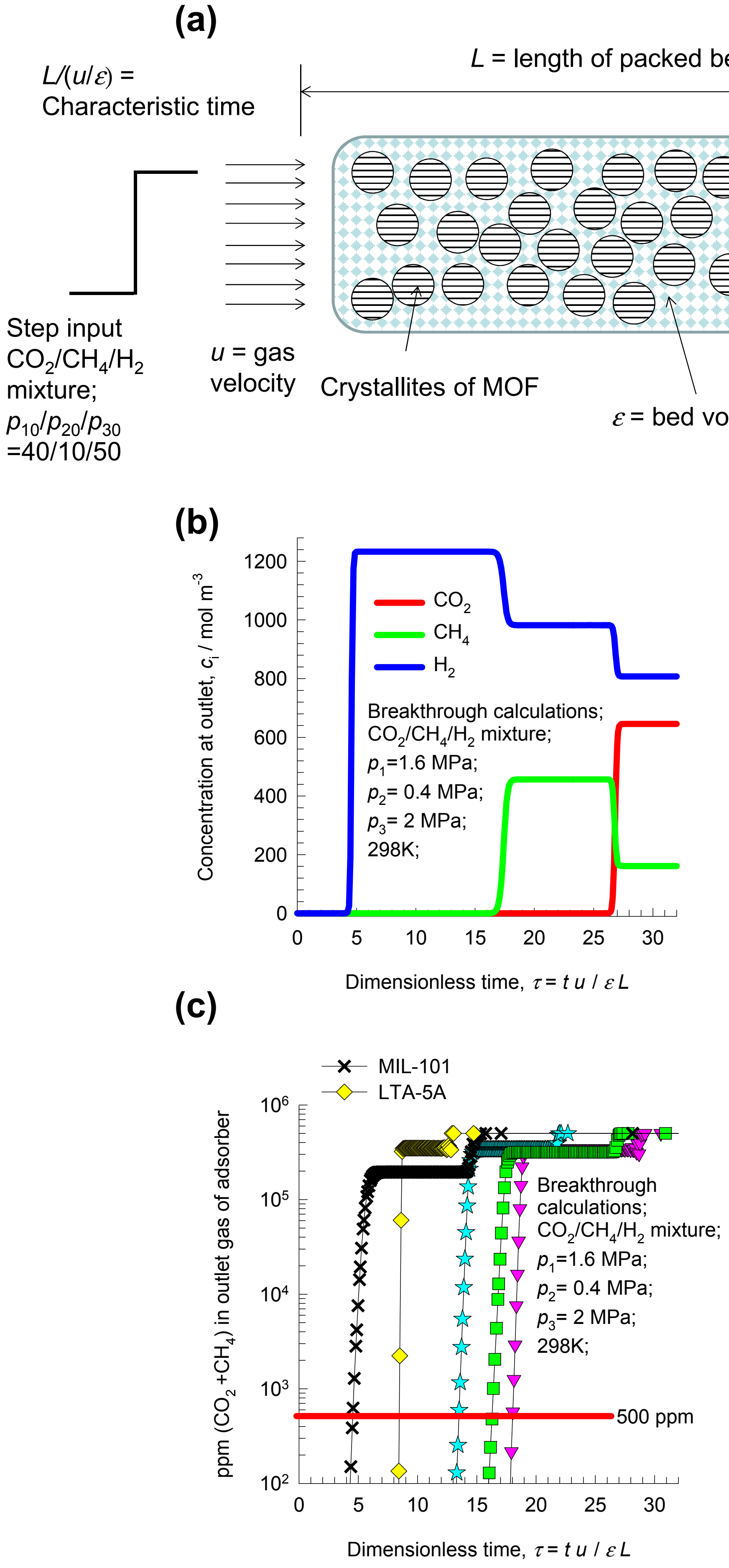

(a)
L/(u/ε) =
Characteristic time
L = length of packed bed
Step input
CO2/CH4/H2
mixture;
p10/p20/p30
=40/10/50
u = gas
velocity
Crystallites of MOF
ε = bed voidage
(b)
Concentration at outlet, ci / mol m-3
0
200
400
600
800
1000
1200
CO2
CH4
H2
Breakthrough calculations;
CO2/CH4/H2 mixture;
p1=1.6 MPa;
p2= 0.4 MPa;
p3= 2 MPa;
298K;
0
5
10
15
20
25
30
Dimensionless time, τ = t u / ε L
(c)
MIL-101
LTA-5A
ppm (CO2 +CH4) in outlet gas of adsorber
10^6
10^5
10^4
10^3
10^2
Breakthrough
calculations;
CO2/CH4/H2 mixture;
p1=1.6 MPa;
p2= 0.4 MPa;
p3= 2 MPa;
298K;
500 ppm
0
5
10
15
20
25
30
Dimensionless time, τ = t u / ε L

Figure 23

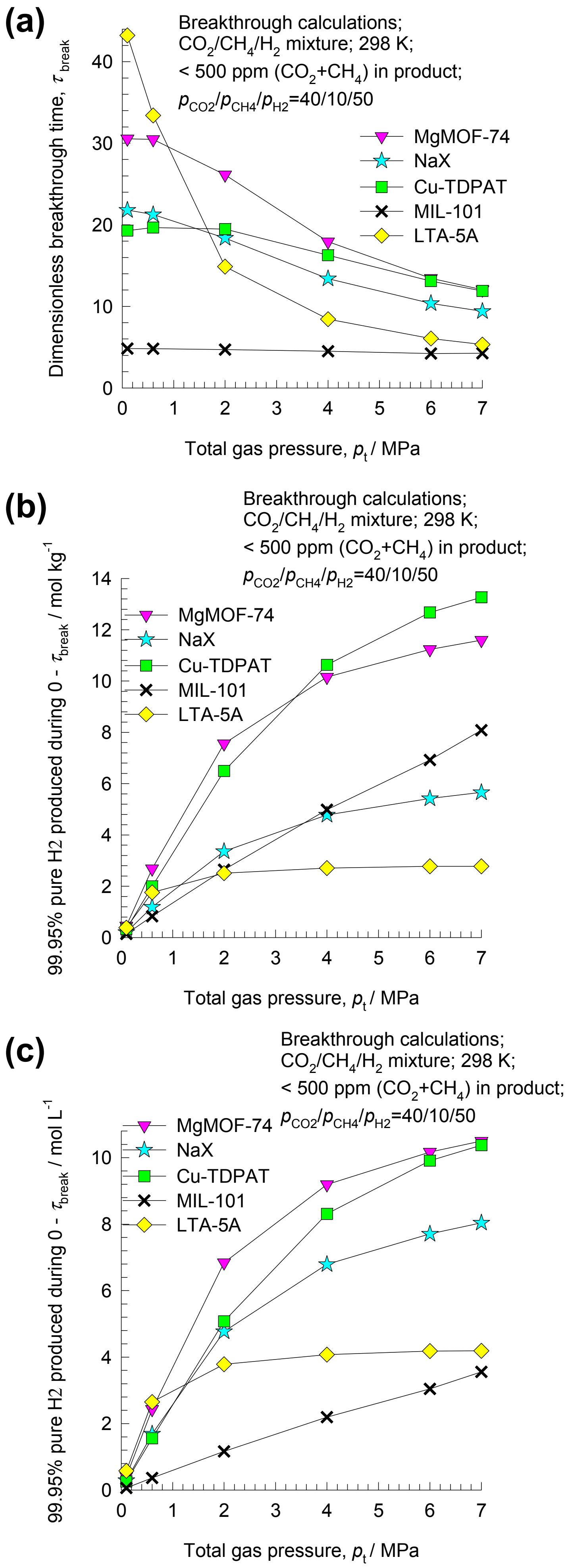
(a)
Breakthrough calculations;
$CO_2/CH_4/H_2$ mixture; 298 K;
< 500 ppm (CO_2+CH_4) in product;
$p_{CO2}/p_{CH4}/p_{H2}$=40/10/50
MgMOF-74
NaX
Cu-TDPAT
MIL-101
LTA-5A
Dimensionless breakthrough time, τ_{break}
0
10
20
30
40
0
1
2
3
4
5
6
7
Total gas pressure, p_t / MPa
(b)
Breakthrough calculations;
$CO_2/CH_4/H_2$ mixture; 298 K;
< 500 ppm (CO_2+CH_4) in product;
$p_{CO2}/p_{CH4}/p_{H2}$=40/10/50
MgMOF-74
NaX
Cu-TDPAT
MIL-101
LTA-5A
99.95% pure H2 produced during 0 - τ_{break} / mol kg^{-1}
0
2
4
6
8
10
12
14
0
1
2
3
4
5
6
7
Total gas pressure, p_t / MPa
(c)
Breakthrough calculations;
$CO_2/CH_4/H_2$ mixture; 298 K;
< 500 ppm (CO_2+CH_4) in product;
$p_{CO2}/p_{CH4}/p_{H2}$=40/10/50
MgMOF-74
NaX
Cu-TDPAT
MIL-101
LTA-5A
99.95% pure H2 produced during 0 - τ_{break} / mol L^{-1}
0
2
4
6
8
10
0
1
2
3
4
5
6
7
Total gas pressure, p_t / MPa

Figure 24

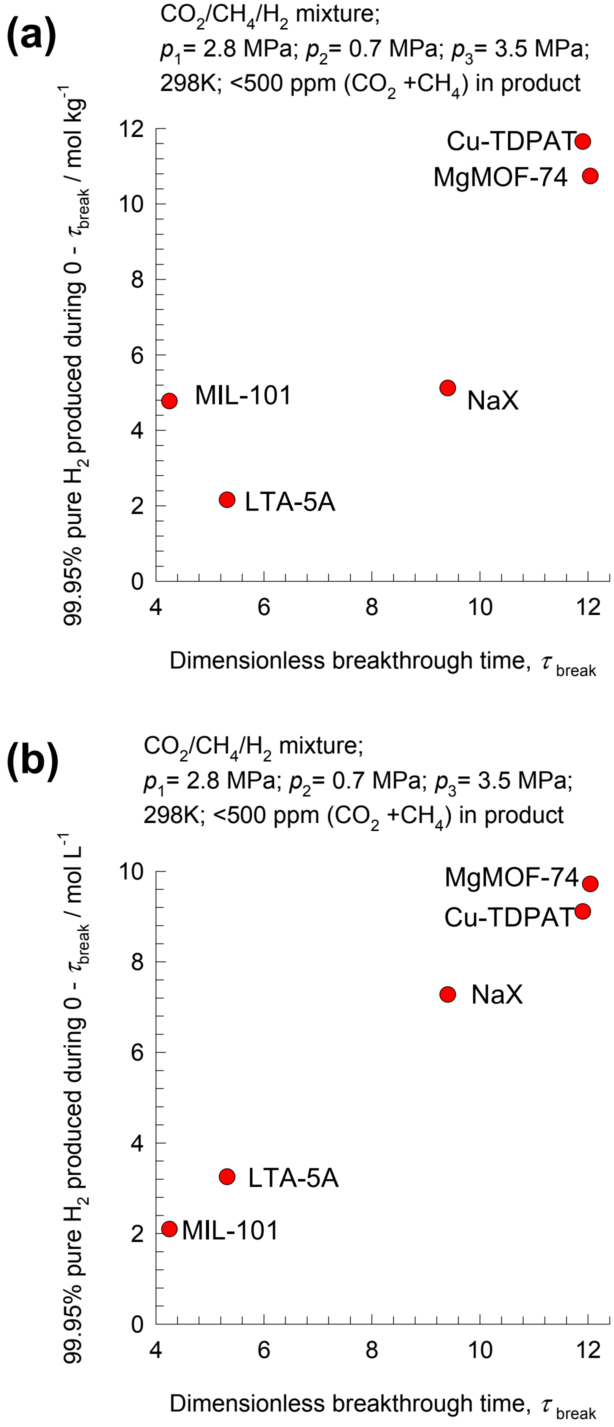
(a)
$CO_2/CH_4/H_2$ mixture;
p_1= 2.8 MPa; p_2= 0.7 MPa; p_3= 3.5 MPa;
298K; <500 ppm (CO_2 +CH_4) in product
99.95% pure H_2 produced during 0 - τ_{break} / mol kg^{-1}
0
2
4
6
8
10
12
4
6
8
10
12
Dimensionless breakthrough time, τ_{break}
Cu-TDPAT
MgMOF-74
MIL-101
NaX
LTA-5A
(b)
$CO_2/CH_4/H_2$ mixture;
p_1= 2.8 MPa; p_2= 0.7 MPa; p_3= 3.5 MPa;
298K; <500 ppm (CO_2 +CH_4) in product
99.95% pure H_2 produced during 0 - τ_{break} / mol L^{-1}
0
2
4
6
8
10
4
6
8
10
12
Dimensionless breakthrough time, τ_{break}
MgMOF-74
Cu-TDPAT
NaX
LTA-5A
MIL-101

Figure 25

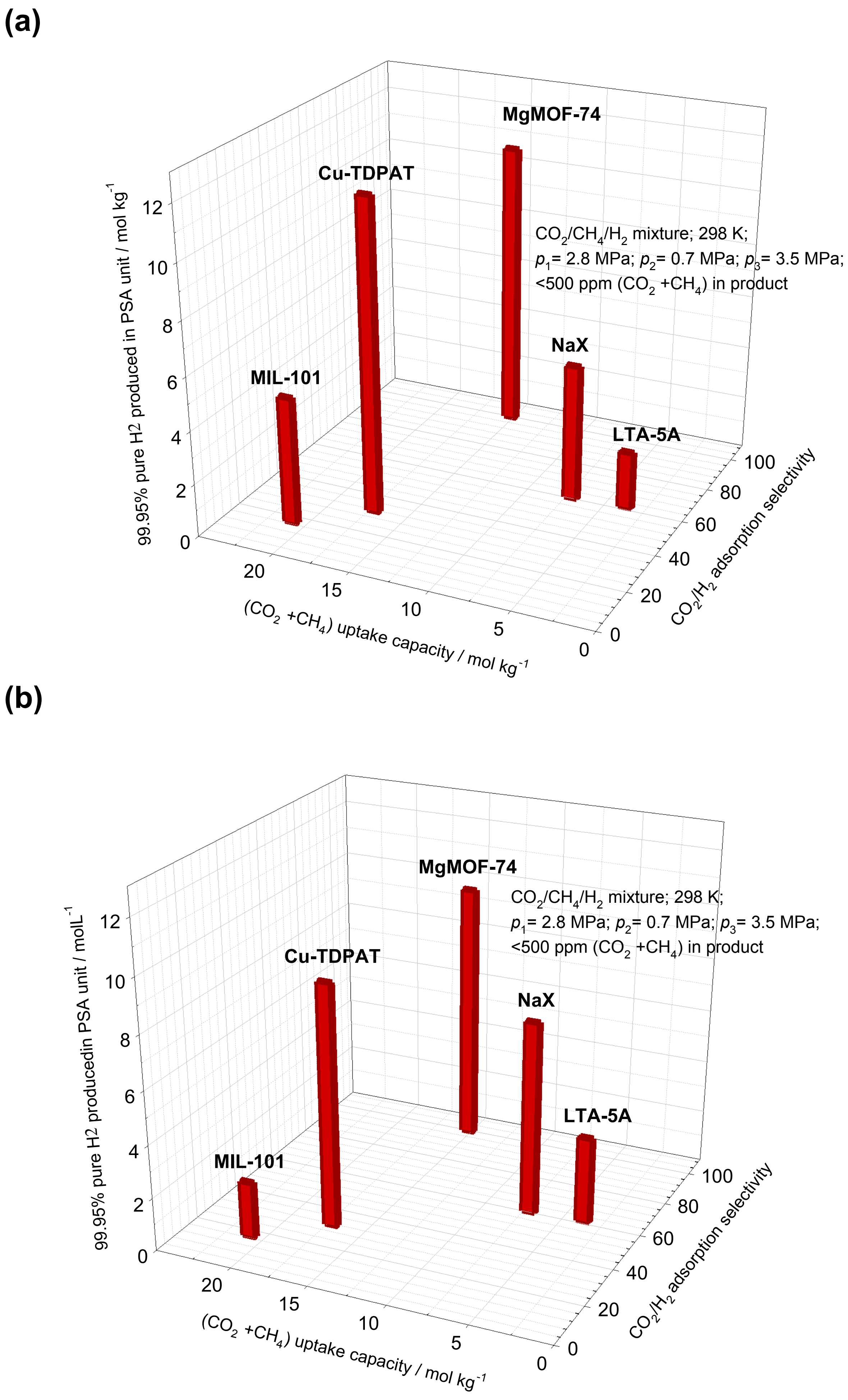
(a)
MgMOF-74
Cu-TDPAT
MIL-101
NaX
LTA-5A
CO2/CH4/H2 mixture; 298 K;
p1= 2.8 MPa; p2= 0.7 MPa; p3= 3.5 MPa;
<500 ppm (CO2 +CH4) in product
99.95% pure H2 produced in PSA unit / mol kg-1
0
2
4
6
8
10
12
(CO2 +CH4) uptake capacity / mol kg-1
20
15
10
5
0
CO2/H2 adsorption selectivity
0
20
40
60
80
100
(b)
MgMOF-74
Cu-TDPAT
MIL-101
NaX
LTA-5A
CO2/CH4/H2 mixture; 298 K;
p1= 2.8 MPa; p2= 0.7 MPa; p3= 3.5 MPa;
<500 ppm (CO2 +CH4) in product
99.95% pure H2 producedin PSA unit / molL-1
0
2
4
6
8
10
12
(CO2 +CH4) uptake capacity / mol kg-1
20
15
10
5
0
CO2/H2 adsorption selectivity
0
20
40
60
80
100

Figure 26

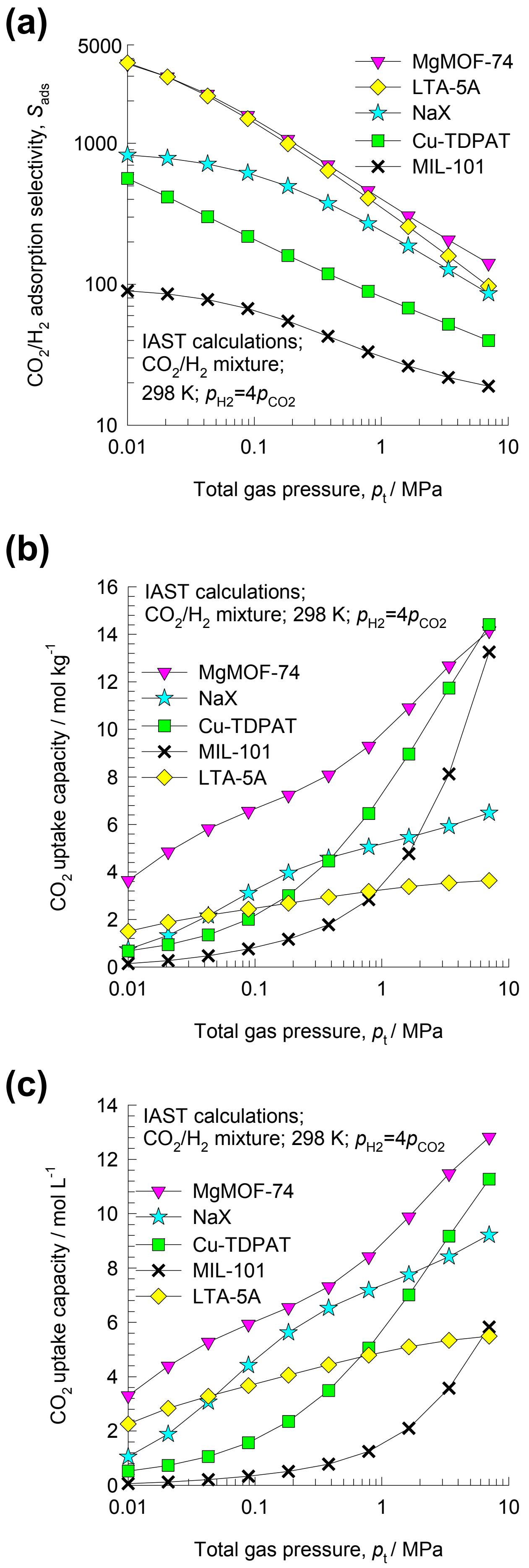
(a)
5000
1000
100
10
CO$_2$/H$_2$ adsorption selectivity, S_{ads}
MgMOF-74
LTA-5A
NaX
Cu-TDPAT
MIL-101
IAST calculations;
CO$_2$/H$_2$ mixture;
298 K; p_{H2}=4p_{CO2}
0.01
0.1
1
10
Total gas pressure, p_t / MPa
(b)
16
14
12
10
8
6
4
2
0
CO$_2$ uptake capacity / mol kg^{-1}
IAST calculations;
CO$_2$/H$_2$ mixture; 298 K; p_{H2}=4p_{CO2}
MgMOF-74
NaX
Cu-TDPAT
MIL-101
LTA-5A
0.01
0.1
1
10
Total gas pressure, p_t / MPa
(c)
14
12
10
8
6
4
2
0
CO$_2$ uptake capacity / mol L^{-1}
IAST calculations;
CO$_2$/H$_2$ mixture; 298 K; p_{H2}=4p_{CO2}
MgMOF-74
NaX
Cu-TDPAT
MIL-101
LTA-5A
0.01
0.1
1
10
Total gas pressure, p_t / MPa

Figure 27

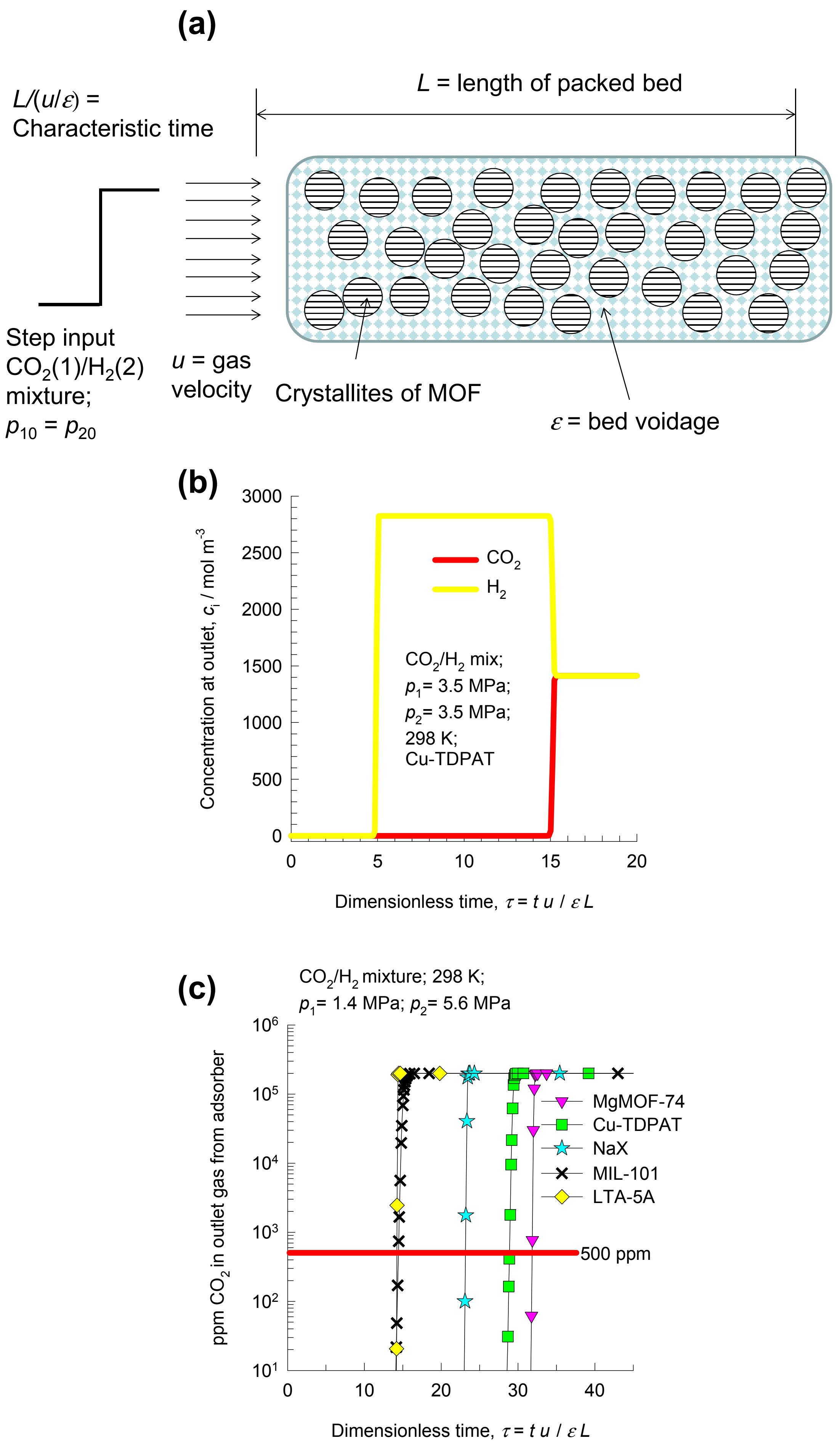

(a)
$L/(u/\varepsilon)$ =
Characteristic time
L = length of packed bed
Step input
$CO_2(1)/H_2(2)$
mixture;
$p_{10} = p_{20}$
u = gas
velocity
Crystallites of MOF
ε = bed voidage
(b)
Concentration at outlet, c_i / mol m^{-3}
3000
2500
2000
1500
1000
500
0
0
5
10
15
20
Dimensionless time, $\tau = t\,u\,/\,\varepsilon\,L$
CO_2
H_2
CO_2/H_2 mix;
p_1= 3.5 MPa;
p_2= 3.5 MPa;
298 K;
Cu-TDPAT
(c)
CO_2/H_2 mixture; 298 K;
p_1= 1.4 MPa; p_2= 5.6 MPa
ppm CO_2 in outlet gas from adsorber
10^6
10^5
10^4
10^3
10^2
10^1
0
10
20
30
40
Dimensionless time, $\tau = t\,u\,/\,\varepsilon\,L$
MgMOF-74
Cu-TDPAT
NaX
MIL-101
LTA-5A
500 ppm

Figure 28

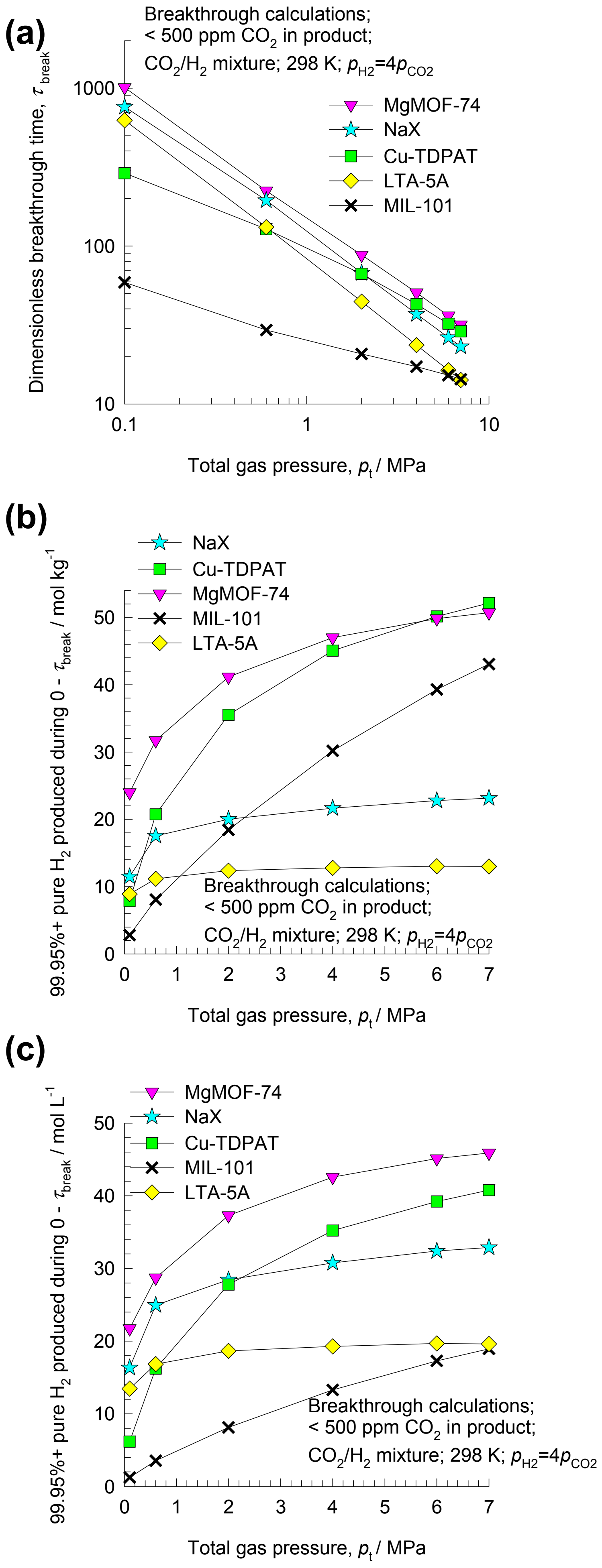

(a)
Breakthrough calculations;
< 500 ppm CO_2 in product;
CO_2/H_2 mixture; 298 K; $p_{H2}=4p_{CO2}$
MgMOF-74
NaX
Cu-TDPAT
LTA-5A
MIL-101
Dimensionless breakthrough time, τ_{break}
1000
100
10
0.1
1
10
Total gas pressure, p_t / MPa
(b)
NaX
Cu-TDPAT
MgMOF-74
MIL-101
LTA-5A
99.95%+ pure H_2 produced during 0 - τ_{break} / mol kg^{-1}
50
40
30
20
10
0
Breakthrough calculations;
< 500 ppm CO_2 in product;
CO_2/H_2 mixture; 298 K; $p_{H2}=4p_{CO2}$
0
1
2
3
4
5
6
7
Total gas pressure, p_t / MPa
(c)
MgMOF-74
NaX
Cu-TDPAT
MIL-101
LTA-5A
99.95%+ pure H_2 produced during 0 - τ_{break} / mol L^{-1}
50
40
30
20
10
0
Breakthrough calculations;
< 500 ppm CO_2 in product;
CO_2/H_2 mixture; 298 K; $p_{H2}=4p_{CO2}$
0
1
2
3
4
5
6
7
Total gas pressure, p_t / MPa

Figure 29

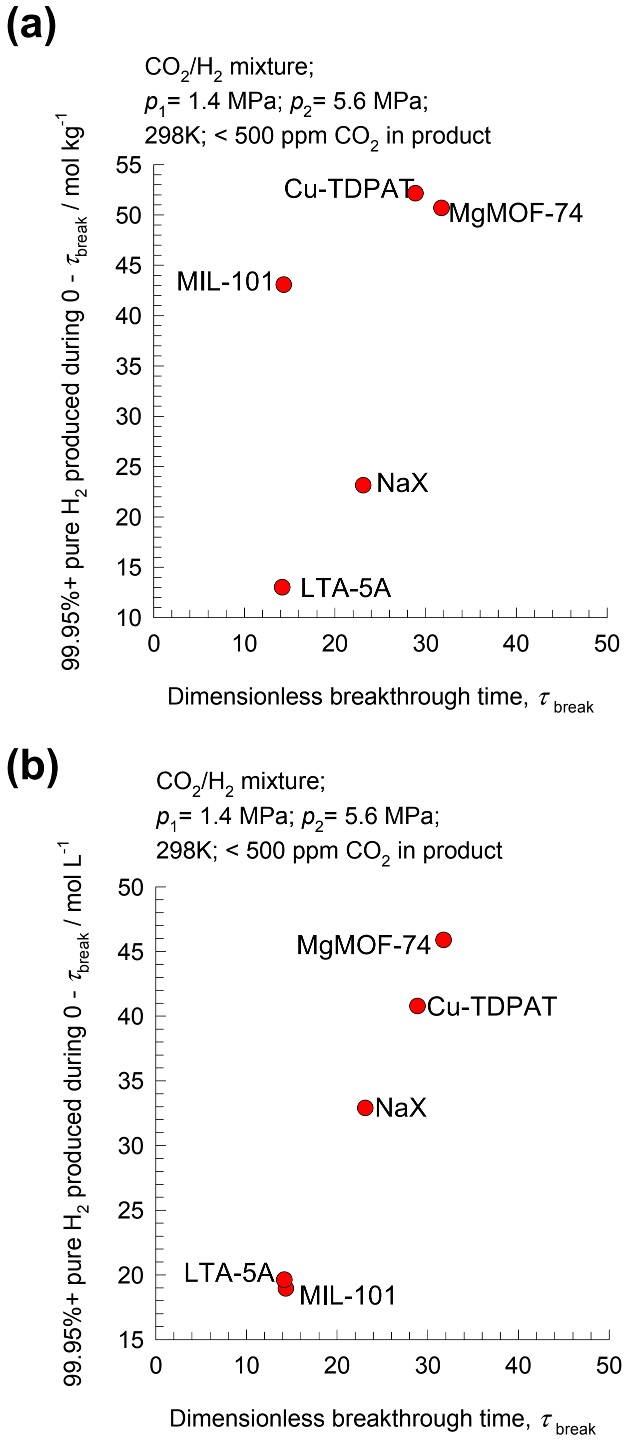
(a)
CO$_2$/H$_2$ mixture;
p_1= 1.4 MPa; p_2= 5.6 MPa;
298K; < 500 ppm CO$_2$ in product
99.95%+ pure H$_2$ produced during 0 - τ_{break} / mol kg^{-1}
Dimensionless breakthrough time, τ_{break}
55
50
45
40
35
30
25
20
15
10
0
10
20
30
40
50
Cu-TDPAT
MgMOF-74
MIL-101
NaX
LTA-5A
(b)
CO$_2$/H$_2$ mixture;
p_1= 1.4 MPa; p_2= 5.6 MPa;
298K; < 500 ppm CO$_2$ in product
99.95%+ pure H$_2$ produced during 0 - τ_{break} / mol L^{-1}
Dimensionless breakthrough time, τ_{break}
50
45
40
35
30
25
20
15
0
10
20
30
40
50
MgMOF-74
Cu-TDPAT
NaX
LTA-5A
MIL-101

Figure 30

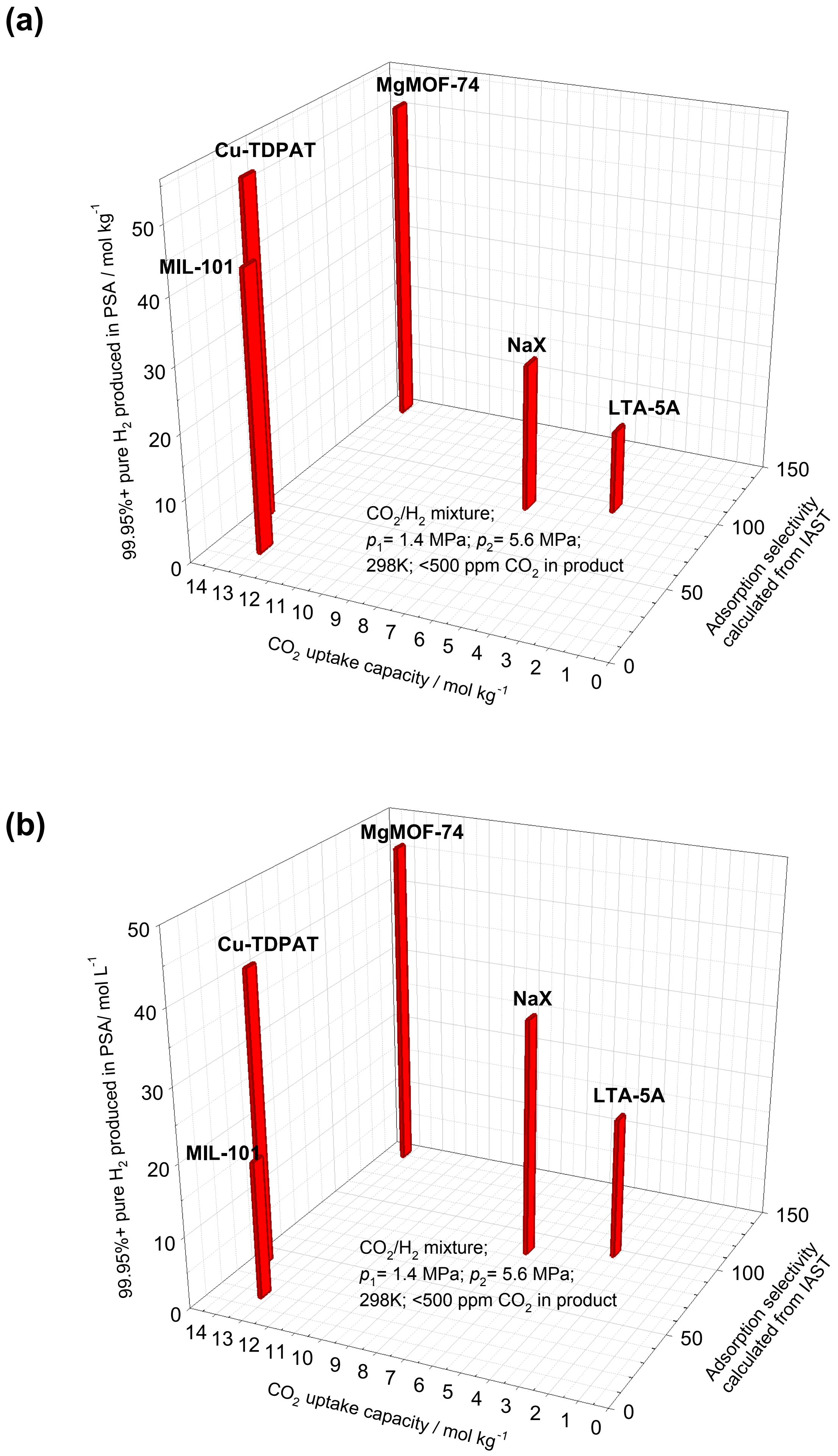
(a)
MgMOF-74
Cu-TDPAT
MIL-101
NaX
LTA-5A
99.95%+ pure H_2 produced in PSA / mol kg^{-1}
0
10
20
30
40
50
CO_2/H_2 mixture;
p_1= 1.4 MPa; p_2= 5.6 MPa;
298K; <500 ppm CO_2 in product
14 13 12 11 10 9 8 7 6 5 4 3 2 1 0
CO_2 uptake capacity / mol kg^{-1}
0
50
100
150
Adsorption selectivity calculated from IAST
(b)
MgMOF-74
Cu-TDPAT
NaX
LTA-5A
MIL-101
99.95%+ pure H_2 produced in PSA/ mol L^{-1}
0
10
20
30
40
50
CO_2/H_2 mixture;
p_1= 1.4 MPa; p_2= 5.6 MPa;
298K; <500 ppm CO_2 in product
14 13 12 11 10 9 8 7 6 5 4 3 2 1 0
CO_2 uptake capacity / mol kg^{-1}
0
50
100
150
Adsorption selectivity calculated from IAST

Figure 31

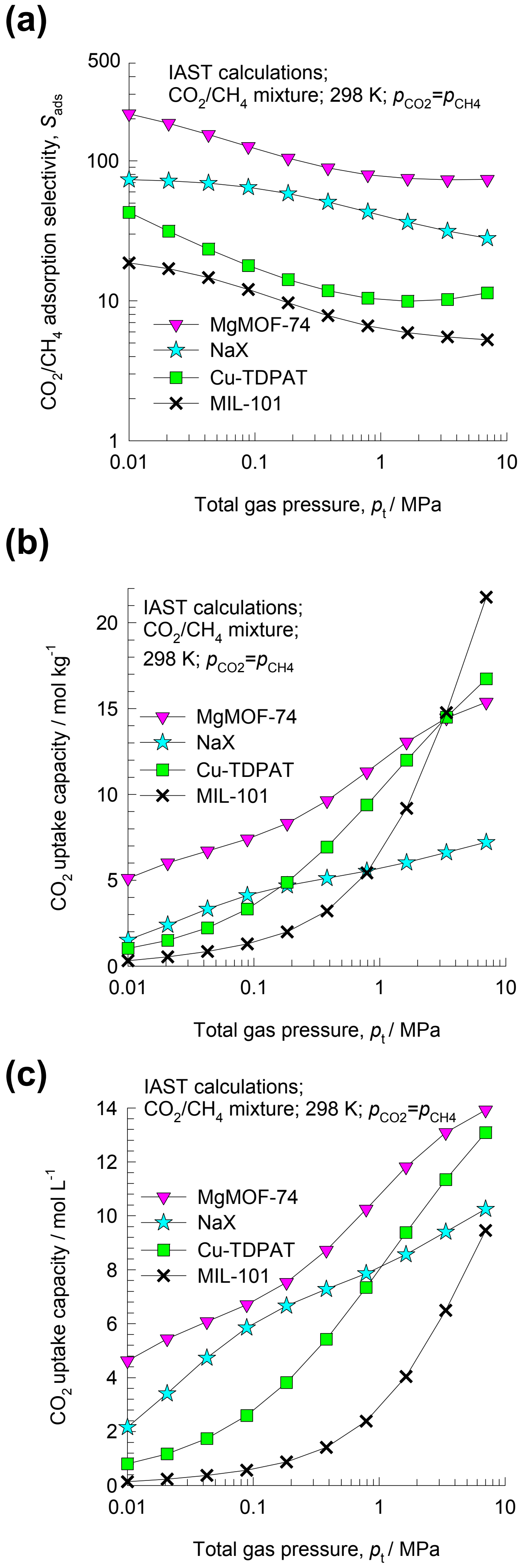
(a)
500
100
10
1
0.01
0.1
1
10
IAST calculations;
CO_2/CH_4 mixture; 298 K; $p_{CO2}=p_{CH4}$
CO_2/CH_4 adsorption selectivity, S_{ads}
MgMOF-74
NaX
Cu-TDPAT
MIL-101
Total gas pressure, p_t / MPa
(b)
IAST calculations;
CO_2/CH_4 mixture;
298 K; $p_{CO2}=p_{CH4}$
20
15
10
5
0
0.01
0.1
1
10
CO_2 uptake capacity / mol kg^{-1}
MgMOF-74
NaX
Cu-TDPAT
MIL-101
Total gas pressure, p_t / MPa
(c)
IAST calculations;
CO_2/CH_4 mixture; 298 K; $p_{CO2}=p_{CH4}$
14
12
10
8
6
4
2
0
0.01
0.1
1
10
CO_2 uptake capacity / mol L^{-1}
MgMOF-74
NaX
Cu-TDPAT
MIL-101
Total gas pressure, p_t / MPa

Figure 32

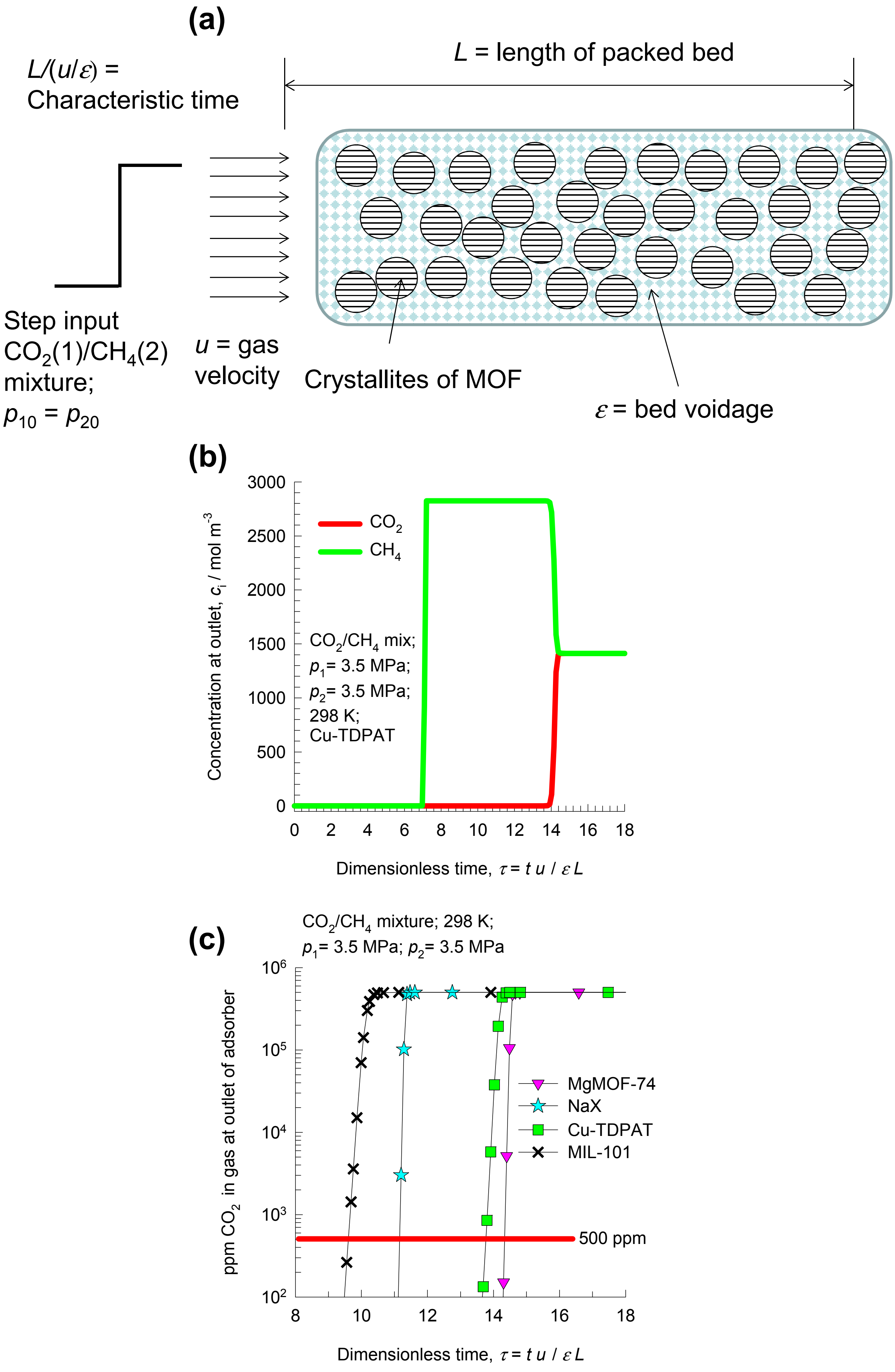

(a)
L/(u/ε) = Characteristic time
L = length of packed bed
Step input CO2(1)/CH4(2) mixture; p10 = p20
u = gas velocity
Crystallites of MOF
ε = bed voidage
(b)
Concentration at outlet, ci / mol m-3
3000
2500
2000
1500
1000
500
0
CO2
CH4
CO2/CH4 mix;
p1= 3.5 MPa;
p2= 3.5 MPa;
298 K;
Cu-TDPAT
0
2
4
6
8
10
12
14
16
18
Dimensionless time, τ = t u / ε L
(c)
CO2/CH4 mixture; 298 K;
p1= 3.5 MPa; p2= 3.5 MPa
ppm CO2 in gas at outlet of adsorber
10^6
10^5
10^4
10^3
10^2
MgMOF-74
NaX
Cu-TDPAT
MIL-101
500 ppm
8
10
12
14
16
18
Dimensionless time, τ = t u / ε L

Figure 33

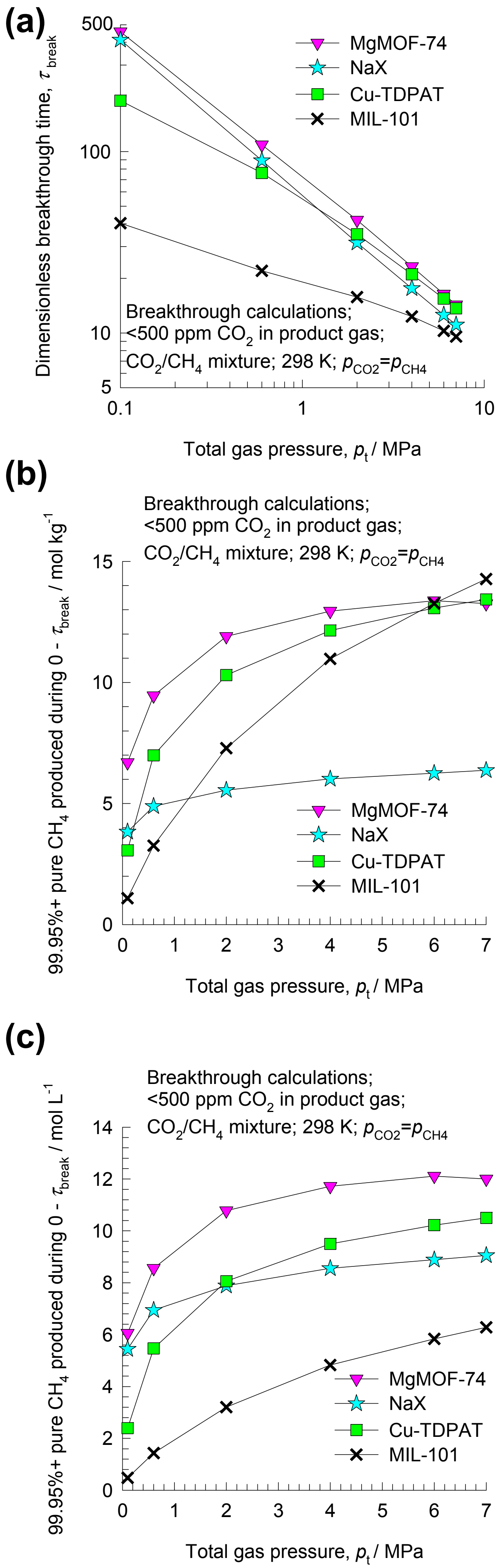

(a)
Dimensionless breakthrough time, τbreak
500
100
10
5
0.1
1
10
Total gas pressure, pt / MPa
MgMOF-74
NaX
Cu-TDPAT
MIL-101
Breakthrough calculations;
<500 ppm CO2 in product gas;
CO2/CH4 mixture; 298 K; pCO2=pCH4
(b)
99.95%+ pure CH4 produced during 0 - τbreak / mol kg-1
0
5
10
15
0
1
2
3
4
5
6
7
Total gas pressure, pt / MPa
Breakthrough calculations;
<500 ppm CO2 in product gas;
CO2/CH4 mixture; 298 K; pCO2=pCH4
MgMOF-74
NaX
Cu-TDPAT
MIL-101
(c)
99.95%+ pure CH4 produced during 0 - τbreak / mol L-1
0
2
4
6
8
10
12
14
0
1
2
3
4
5
6
7
Total gas pressure, pt / MPa
Breakthrough calculations;
<500 ppm CO2 in product gas;
CO2/CH4 mixture; 298 K; pCO2=pCH4
MgMOF-74
NaX
Cu-TDPAT
MIL-101

Figure 34

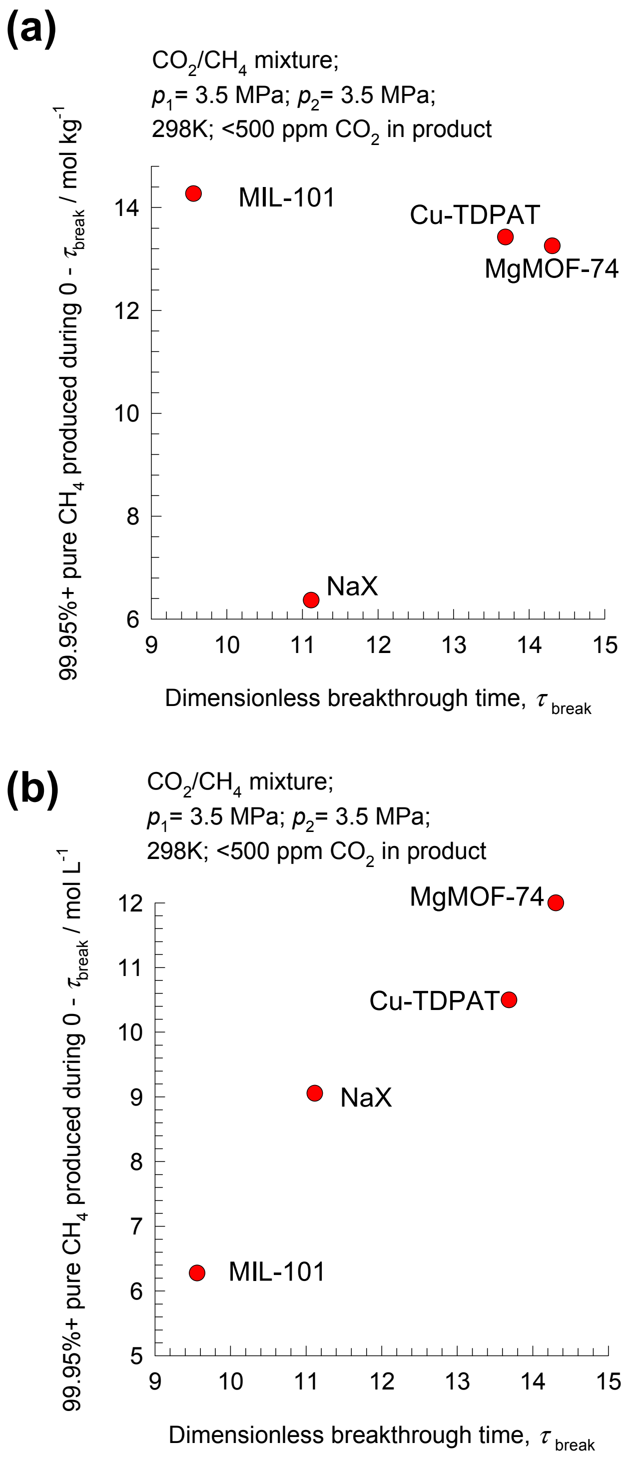

(a)
CO2/CH4 mixture;
p1= 3.5 MPa; p2= 3.5 MPa;
298K; <500 ppm CO2 in product
99.95%+ pure CH4 produced during 0 - τbreak / mol kg-1
6
8
10
12
14
9
10
11
12
13
14
15
Dimensionless breakthrough time, τ break
MIL-101
Cu-TDPAT
MgMOF-74
NaX
(b)
CO2/CH4 mixture;
p1= 3.5 MPa; p2= 3.5 MPa;
298K; <500 ppm CO2 in product
99.95%+ pure CH4 produced during 0 - τbreak / mol L-1
5
6
7
8
9
10
11
12
9
10
11
12
13
14
15
Dimensionless breakthrough time, τ break
MgMOF-74
Cu-TDPAT
NaX
MIL-101

Figure 35

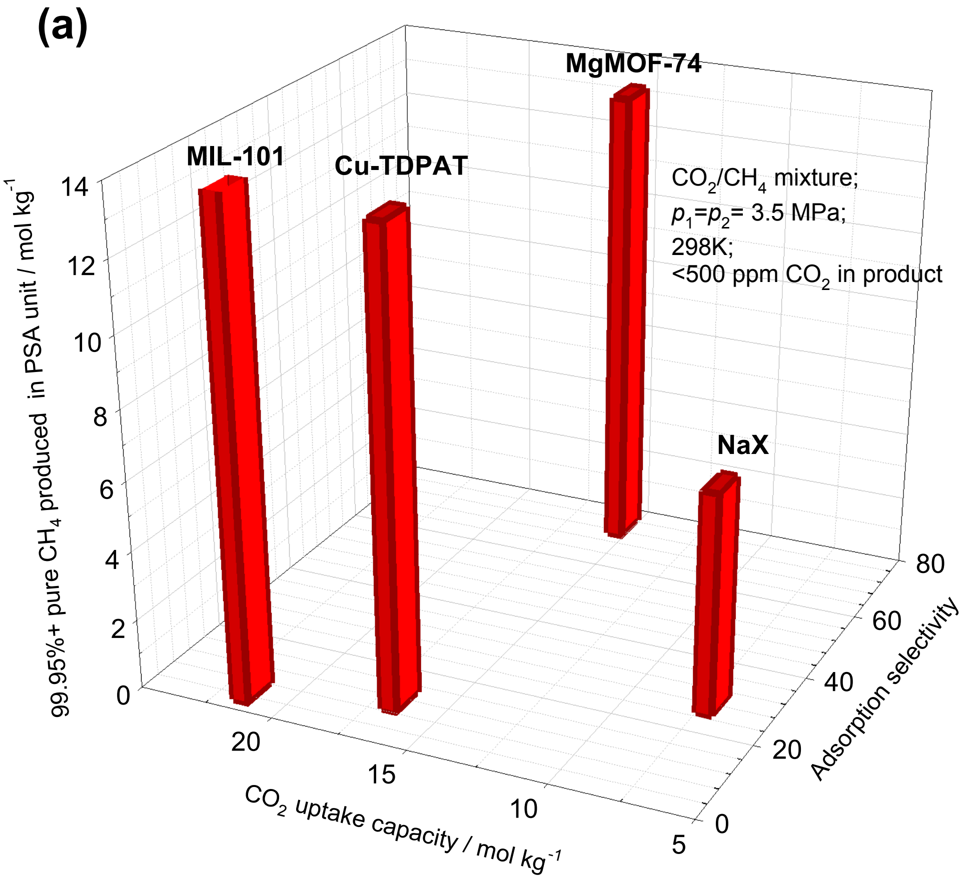
(a)
MIL-101
Cu-TDPAT
MgMOF-74
NaX
CO$_2$/CH$_4$ mixture;
p_1=p_2= 3.5 MPa;
298K;
<500 ppm CO$_2$ in product
99.95%+ pure CH$_4$ produced in PSA unit / mol kg^{-1}
0
2
4
6
8
10
12
14
CO$_2$ uptake capacity / mol kg^{-1}
20
15
10
5
Adsorption selectivity
0
20
40
60
80

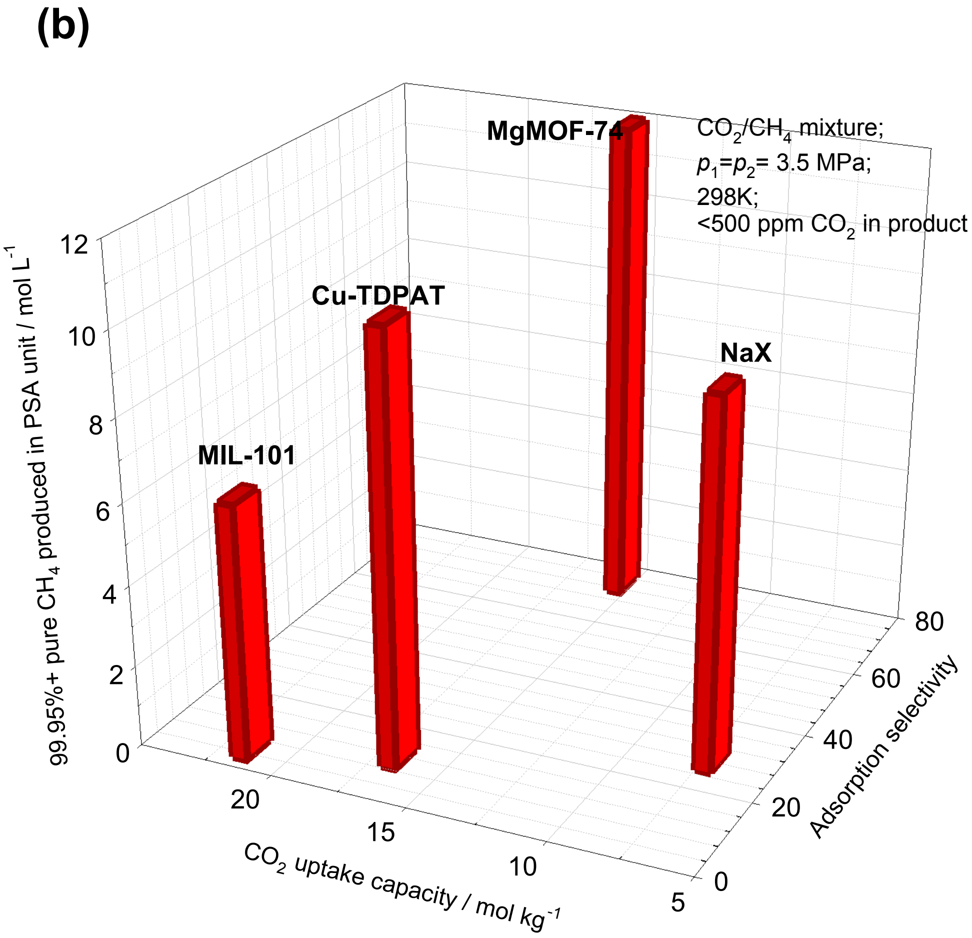
(b)
MgMOF-74
Cu-TDPAT
NaX
MIL-101
CO$_2$/CH$_4$ mixture;
p_1=p_2= 3.5 MPa;
298K;
<500 ppm CO$_2$ in product
99.95%+ pure CH$_4$ produced in PSA unit / mol L^{-1}
0
2
4
6
8
10
12
CO$_2$ uptake capacity / mol kg^{-1}
20
15
10
5
Adsorption selectivity
0
20
40
60
80

Figure 36

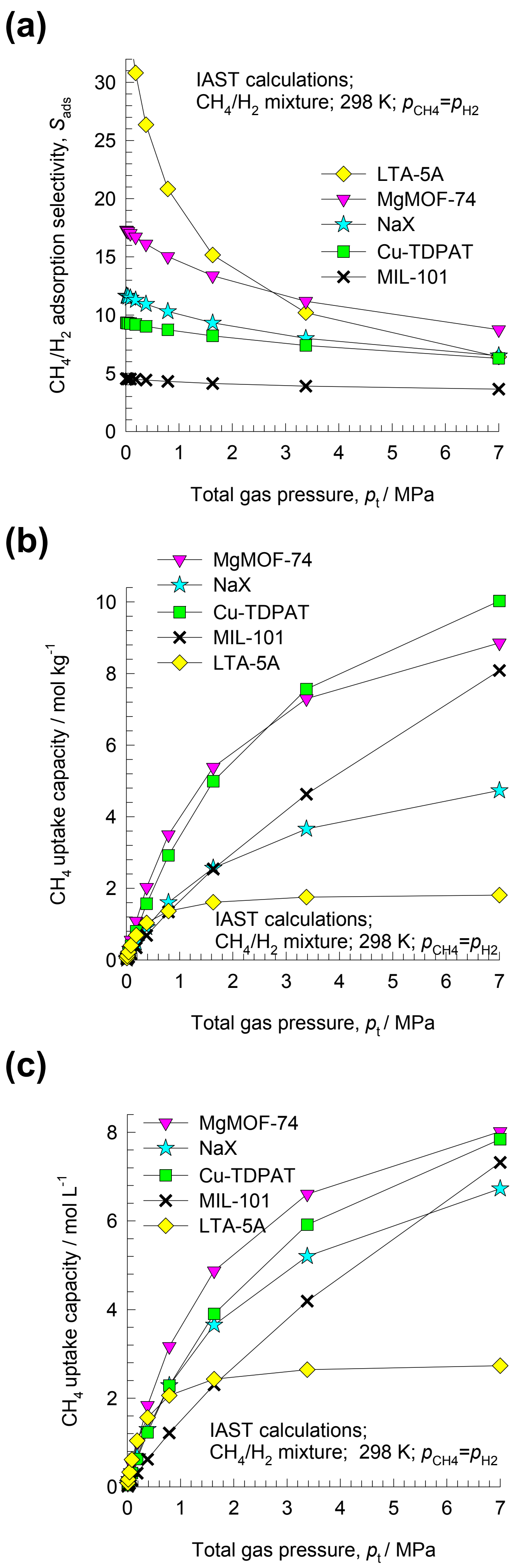
(a)
IAST calculations;
CH4/H2 mixture; 298 K; pCH4=pH2
LTA-5A
MgMOF-74
NaX
Cu-TDPAT
MIL-101
CH4/H2 adsorption selectivity, Sads
0
5
10
15
20
25
30
0
1
2
3
4
5
6
7
Total gas pressure, pt / MPa
(b)
MgMOF-74
NaX
Cu-TDPAT
MIL-101
LTA-5A
IAST calculations;
CH4/H2 mixture; 298 K; pCH4=pH2
CH4 uptake capacity / mol kg-1
0
2
4
6
8
10
0
1
2
3
4
5
6
7
Total gas pressure, pt / MPa
(c)
MgMOF-74
NaX
Cu-TDPAT
MIL-101
LTA-5A
IAST calculations;
CH4/H2 mixture; 298 K; pCH4=pH2
CH4 uptake capacity / mol L-1
0
2
4
6
8
0
1
2
3
4
5
6
7
Total gas pressure, pt / MPa

Figure 37

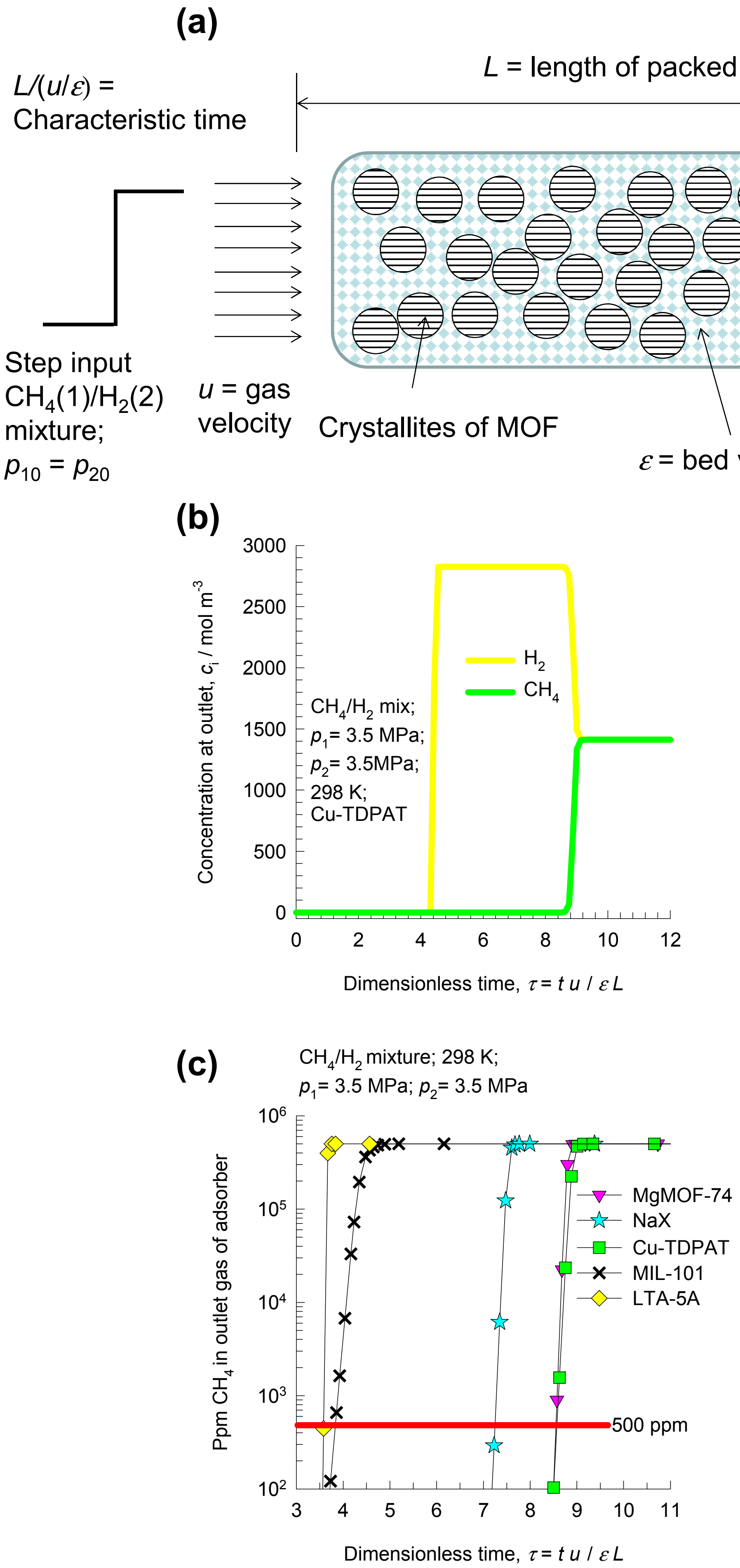
(a)
L/(u/ε) = Characteristic time
L = length of packed bed
Step input CH$_4$(1)/H$_2$(2) mixture; $p_{10} = p_{20}$
u = gas velocity
Crystallites of MOF
ε = bed voidage
(b)
Concentration at outlet, c_i / mol m^{-3}
0
500
1000
1500
2000
2500
3000
0
2
4
6
8
10
12
H$_2$
CH$_4$
CH$_4$/H$_2$ mix;
p_1= 3.5 MPa;
p_2= 3.5MPa;
298 K;
Cu-TDPAT
Dimensionless time, τ = t u / ε L
(c)
CH$_4$/H$_2$ mixture; 298 K;
p_1= 3.5 MPa; p_2= 3.5 MPa
Ppm CH$_4$ in outlet gas of adsorber
10^2
10^3
10^4
10^5
10^6
3
4
5
6
7
8
9
10
11
MgMOF-74
NaX
Cu-TDPAT
MIL-101
LTA-5A
500 ppm
Dimensionless time, τ = t u / ε L

Figure 38

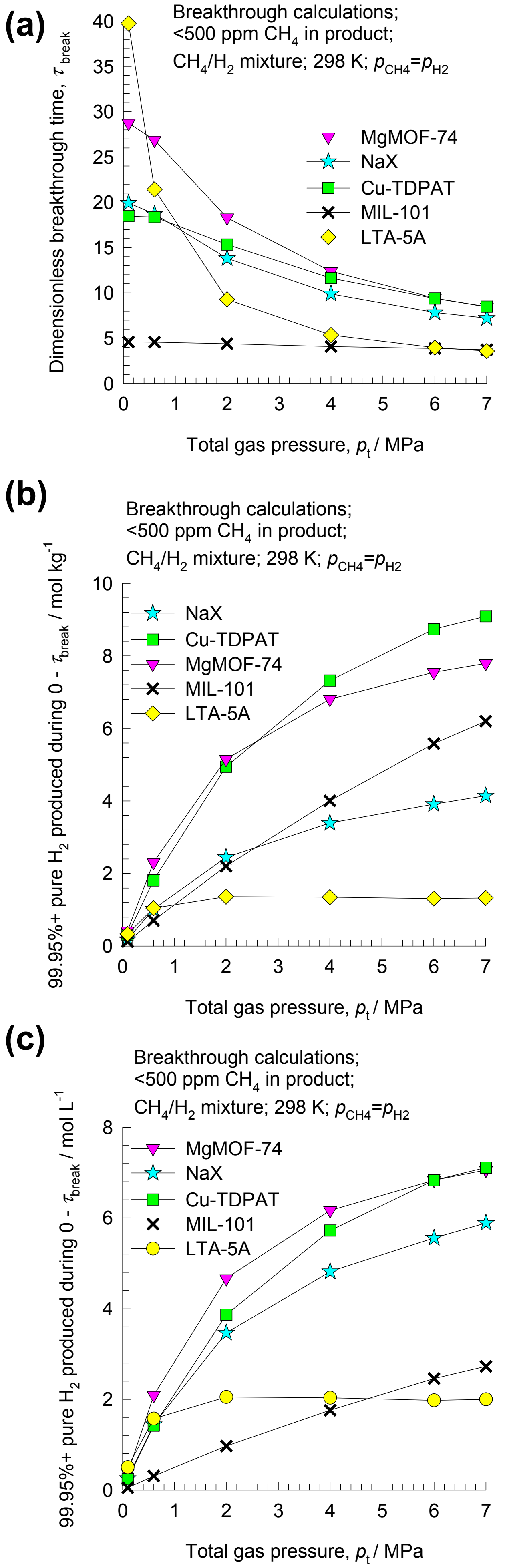
(a)
Breakthrough calculations;
<500 ppm CH4 in product;
CH4/H2 mixture; 298 K; pCH4=pH2
Dimensionless breakthrough time, τbreak
0
5
10
15
20
25
30
35
40
MgMOF-74
NaX
Cu-TDPAT
MIL-101
LTA-5A
0
1
2
3
4
5
6
7
Total gas pressure, pt / MPa
(b)
Breakthrough calculations;
<500 ppm CH4 in product;
CH4/H2 mixture; 298 K; pCH4=pH2
99.95%+ pure H2 produced during 0 - τbreak / mol kg-1
0
2
4
6
8
10
NaX
Cu-TDPAT
MgMOF-74
MIL-101
LTA-5A
0
1
2
3
4
5
6
7
Total gas pressure, pt / MPa
(c)
Breakthrough calculations;
<500 ppm CH4 in product;
CH4/H2 mixture; 298 K; pCH4=pH2
99.95%+ pure H2 produced during 0 - τbreak / mol L-1
0
2
4
6
8
MgMOF-74
NaX
Cu-TDPAT
MIL-101
LTA-5A
0
1
2
3
4
5
6
7
Total gas pressure, pt / MPa

Figure 39

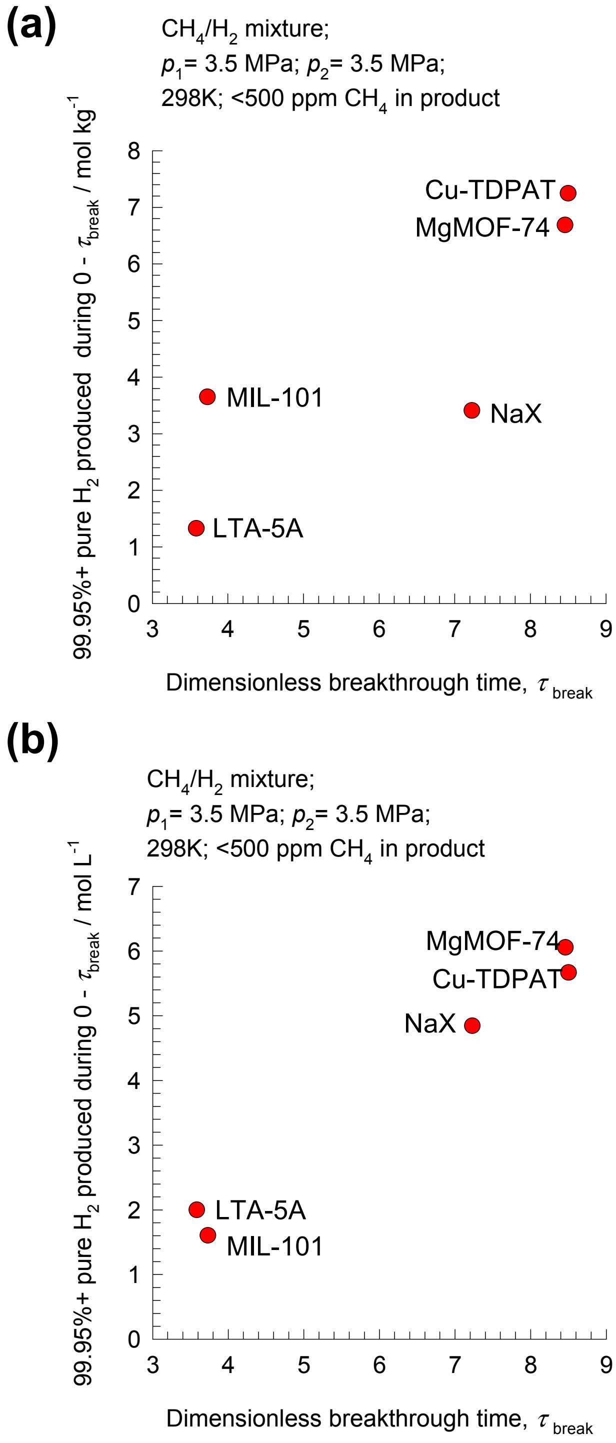
(a)
CH$_4$/H$_2$ mixture;
p_1= 3.5 MPa; p_2= 3.5 MPa;
298K; <500 ppm CH$_4$ in product
99.95%+ pure H$_2$ produced during 0 - τ_{break} / mol kg^{-1}
0
1
2
3
4
5
6
7
8
3
4
5
6
7
8
9
Cu-TDPAT
MgMOF-74
MIL-101
NaX
LTA-5A
Dimensionless breakthrough time, τ_{break}
(b)
CH$_4$/H$_2$ mixture;
p_1= 3.5 MPa; p_2= 3.5 MPa;
298K; <500 ppm CH$_4$ in product
99.95%+ pure H$_2$ produced during 0 - τ_{break} / mol L^{-1}
0
1
2
3
4
5
6
7
3
4
5
6
7
8
9
MgMOF-74
Cu-TDPAT
NaX
LTA-5A
MIL-101
Dimensionless breakthrough time, τ_{break}

Figure 40

(a)

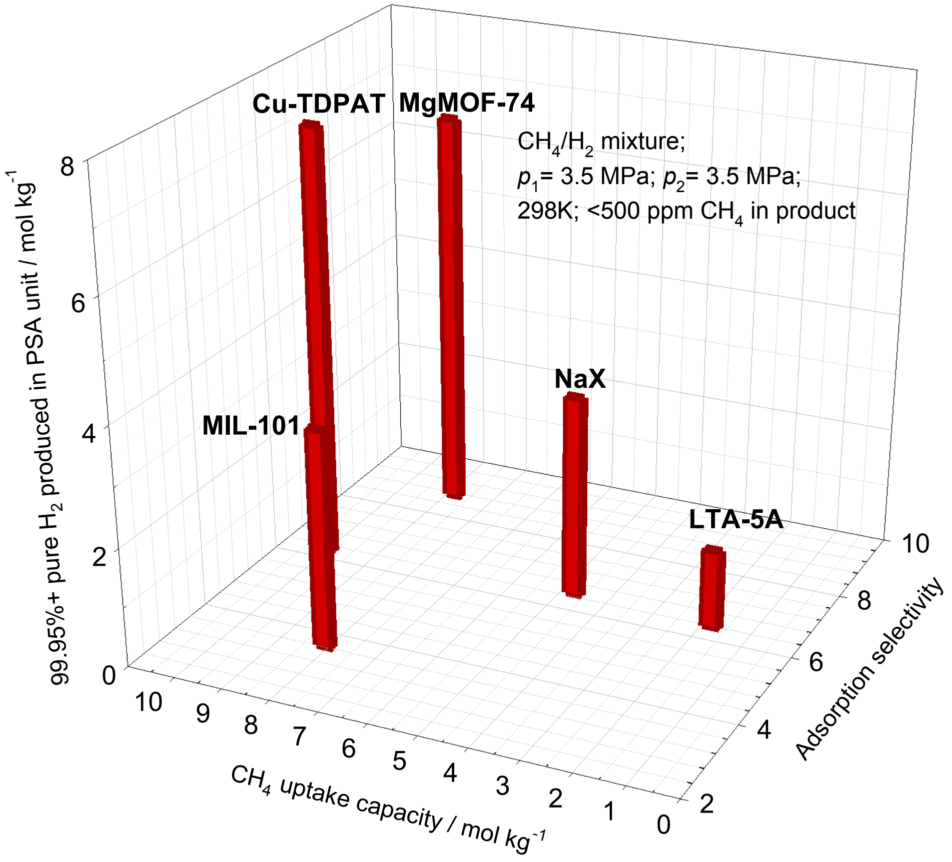
Cu-TDPAT
MgMOF-74
MIL-101
NaX
LTA-5A
CH4/H2 mixture;
p1= 3.5 MPa; p2= 3.5 MPa;
298K; <500 ppm CH4 in product
99.95%+ pure H2 produced in PSA unit / mol kg-1
0
2
4
6
8
CH4 uptake capacity / mol kg-1
10
9
8
7
6
5
4
3
2
1
0
Adsorption selectivity
2
4
6
8
10

(b)

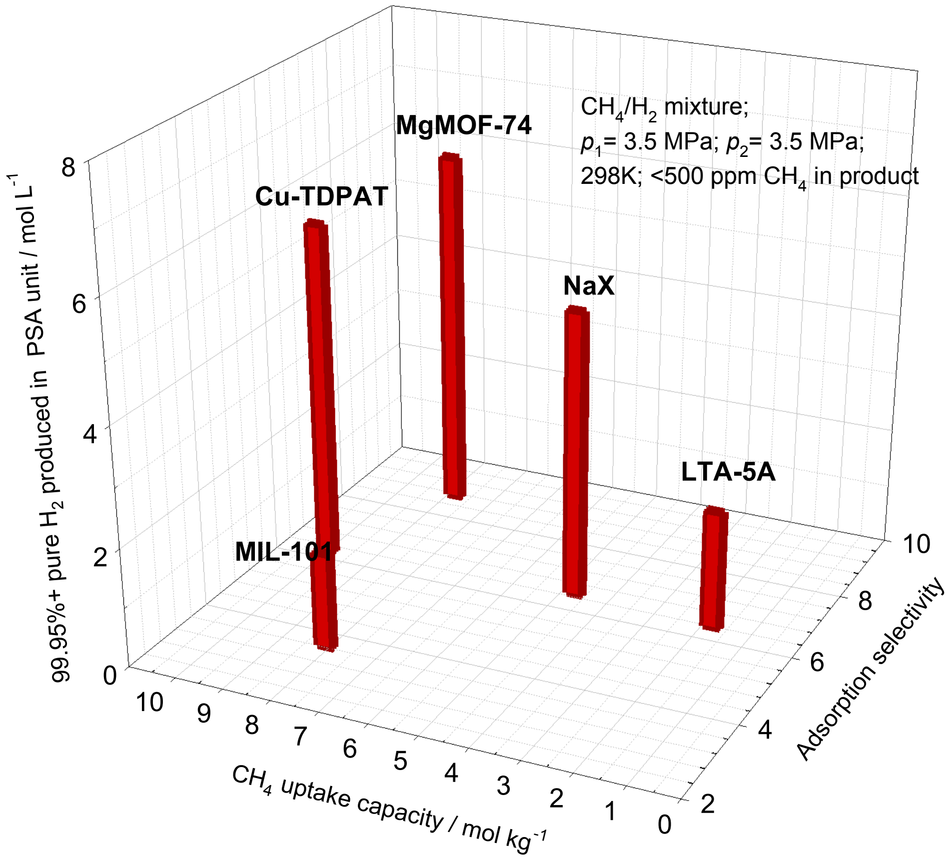
Cu-TDPAT
MgMOF-74
MIL-101
NaX
LTA-5A
CH4/H2 mixture;
p1= 3.5 MPa; p2= 3.5 MPa;
298K; <500 ppm CH4 in product
99.95%+ pure H2 produced in PSA unit / mol L-1
0
2
4
6
8
CH4 uptake capacity / mol kg-1
10
9
8
7
6
5
4
3
2
1
0
Adsorption selectivity
2
4
6
8
10